The effect of land cover change on surface wind resource in southwest Western Australia

and implications for wind energy generation

Anthony Liu

Supervised by Dr Merlinde Kay

School of Photovoltaic and
Renewable Energy Engineering

Faculty of Engineering

The University of New South Wales

November, 2022

A thesis submitted in partial fulfilment of the requirements for the degree of Master of Engineering Science in Renewable Energy Engineering.

WWW.UNSW.EDU.AU

First edition, Friday 18th November, 2022

Acknowledgements

Thank you to my supervisor Dr Merlinde Kay for guiding me through my project and keeping me on task.

Thank you to the UNSW IT support team, for answering my enquiries regarding use of the Katana computational cluster.

Thank you to the ECMWF specialist support team, for answering my enquiries regarding the ERA5 dataset.

Thank you to the NOAA-PSL data team, for answering my enquiries regarding their climate indices.

Thank you to the presenters who ran the American Meteorological Society's Python for Climate and Meteorology 2021 Short Course, including those from the Data Carpentry and MetPy teams, who provided me the basic understanding of relevant Python libraries to complete this thesis project.

Thank you the development team for the xarray Python package (especially staff from the National Center for Atmospheric Research who created relevant tutorials), the Pangeo community, and the Project Pythia community, who created the various online resources and examples which I drew from in creating the code for this project.

Thank you to the Australian Bureau of Meteorology, for providing access to the BARRA reanalysis dataset, and the NSW Department of Planning and Environment, for providing access to urban density datasets, even though a change in project scope meant these datasets were not used.

Thank you to Dr Jean-Paul Ebejer from The University of Malta, who created this LaTeX thesis template and made it available for general use.

And in general, thank you to all the people who contributed to the literature, as well as software, which made this research possible.

This research includes computations using the computational cluster Katana supported by Research Technology Services at UNSW Sydney.

Abstract

There has been extensive conversion of natural forest into farmland in southwest Western Australia since European settlement. This has led to significant changes in atmospheric patterns, and is implicated for an estimated 10% loss of water vapour flows over this region. This work seeks to understand the mechanisms behind surface wind patterns surrounding these atmospheric changes. This work argues that beyond changes in surface friction, conversion of forest into farmland has fundamentally altered the thermodynamics of the region. We present evidence of how atmospheric energy conversions and surface energy fluxes can be sharply delineated by land cover differences. We present evidence suggesting a possible weakening of summer daytime sea breezes which resulted from historical clearing, which in theory would have led to decreased energy supply from coastal wind farms at the same time of increased energy demand from less cool relief for Perth. We also discover anomalies which point towards an unacknowledged contribution from atmospheric condensation. A set of general heuristics is formulated for assessing the likely interactions between future land cover change and circulations. A better understanding of these land-atmosphere interactions allows more accurate assessments of long-term project risk for wind energy developments, but also has import ramifications for cognate fields such as hydrology, climate science, environmental sustainability and hydroelectricity generation.

Author contribution All code used was personally written from scratch, although small sections occasionally draw heavy inspiration from examples in online tutorials and help forums. All results and analysis were personally produced.

Contents

List of Figures

List of Tables

List of Abbreviations

1

Introduction

1.1 | Background

1.1.1 | Brief history of land cover in southwest Western Australia

The southwest region of Western Australia (WA) has experienced extensive Land Cover Change (LCC) over the past two centuries since European settlement (Narisma and Pitman, 2003), including an intensive period from 1950 to 1980 (Xinmei et al., 1995). This has primarily taken the form of clearing native trees for livestock pastures, with subsequent adoption of wheat as the main agricultural crop in the region (Narisma and Pitman, 2003; Xinmei et al., 1995). This change has been heavily implicated for significant atmospheric changes in the region, including an estimated 10% decrease in water vapour flows, significant decline in rainfall, and subsequent drying of the region (Gordon et al., 2003).

Subsequent studies have then noted that wheat in the area, which is light in colour and has an annual growing season supported by irrigation, and for which the accompanying farmland is often left bare between harvest and the next growing season, has produced a marked seasonality in the surface temperature and surface energy balances in the agricultural region (Lyons et al., 1996). As water vapour flows indict the effect of winds, and temperature is known to correlate with wind speeds (Lapworth, 2003, 2006), it is then natural to suspect that there have also been changes in surface winds which are attributable to the LCC.

1.1.2 | Broader context

It is well known that agricultural cover induces less friction upon surface winds than taller tree cover (Geiger, 1950). But delineations by the State Boundary Fence of Western Australia (SBFWA) between agricultural and native vegetation show similar roughnesses (Lyons et al., 2001) yet still display dramatically different atmospheric conditions

(Ray et al., 2003). So other effects are likely at play. A better understanding of the driving mechanisms behind these historical changes allows better assessment of what effect future land cover change is likely to have.

Parallel with these developments has been unprecedented anthropogenic change in other regions and countries as well. Studies across different areas often produce seemingly disparate and often contrasting results (Xu et al., 2022). But this also provides opportunity for a comparative study to elicit the general principles behind air circulation. This project seeks to further understanding into this by studying in detail the unique land cover delineation observed in southwest WA, then placing this in a broader picture consistent with literature findings.

1.2 | Motivations

The question of how LCC affects Surface Wind (SW) is poorly understood, as evidenced by the limited literature attempting this direct link. From the perspective of wind generation, wind is often viewed as a passive resource for exploitation. But to the extent that the future of winds can be highly variable to the path of land cover trends, this represents an additional risk which may not be internalised in project considerations.

Furthermore, although this thesis was conducted primarily under the context of wind energy generation, the subject of this research also has important ramifications for cognate fields such as hydrology, climate science, environmental sustainability and hydroelectricity generation. As winds affect moisture convergence patterns and subsequent rainfall, this may have important social, geopolitical, and ecological consequences.

1.3 | Broad research aims

The broad research aims of this project are:

- Understand what are the main drivers behind local atmospheric circulations.
- Understand the general principles behind land cover-wind interactions.
- Deduce what ramifications future LCC may entail.

1.4 | Objectives and scope

- Analyse how historical and future LCC may have affected or may affect the surface wind resource in southwest WA.
- Articulate the likely impacts future LCC may have on wind energy operation.
- Evaluate the role which temperature gradients and atmospheric condensation have on the diurnal and seasonal variability of atmospheric energy conversions and surface energy balances.
- Devise, using a combination of project results and literature findings, a set of general heuristics for assessing how land cover affects surface wind patterns.

1.5 | Thesis statement and hypothesis

LCC has led to a significant change in the surface wind patterns of southwest WA. These changes cannot be solely attributed to roughness length changes. There should at least be some effect from surface temperature and energy balance changes, possibly then leading to changes in atmospheric energy conversions. Changes in wind patterns should then produce non-trivial effects on wind energy generation.

1.6 | Overview and structure of thesis

1.6.1 | Chapters

Literature Review Following this introductory chapter, we first present a literature review (Section 2) of research into recent Near Surface Wind Speed (NSWS) changes, debates regarding the relative contribution between urbanisation and large-scale atmospheric oscillations towards observed changes and disparate literature on vegetation-atmosphere interactions.

Methodology Secondly, we present the methodology (Section 3) used in our analysis, including justifications for our choice of study regions and periods, statistical summaries tailored for investigating diurnal and seasonal variations, as well as the variables, datasets and software used in our analysis.

Results and Discussion of Findings Next, we present our results and discussion of findings (Section 4), for different types of comparisons including diurnal, seasonal and cross-period analysis punctuated by significant vegetation cover change. We discuss what these results indicate regarding the general principles behind atmospheric circulations, and look at how this is likely to affect wind energy operation.

Extended Discussion Then, we present an extended discussion (Section 5) on a conceptual framework we developed for making sense of apparently contradictory observations in the project results as well as literature. We also discuss the limitations, improvements and future directions given the overall approach taken in this project.

Conclusions and Summary Finally, we provide our conclusions and summary (Section 6) of the key insights and progress achieved over this project.

1.6.2 | Ancillary focus on water vapour

1.6.2.1 | Reasons for ancillary focus

Throughout this thesis, there is a heavy ancillary focus on atmospheric water vapour.[1] This is true for the selection of research in the literature review, the choice of study variables in the methodology, and all subsequent analysis. There is an inherent link between winds and atmospheric water vapour since the former is the means by which transport of the latter occurs. More explicit reasons for this focus include:

- There is a limited amount of literature which directly addresses the link between LCC and SW. In contrast, there is a wealth of literature directly addressing how LCC affects atmospheric moisture trends, from which the effects on wind are implicit and from which many valuable insights can be drawn.
- Reanalysis datasets represent gridded averages, which often omit surface wind observations since the open terrain stipulated by World Meteorological Organization (WMO) Automatic Weather Station (AWS) standards are not well represented in grids with large extents.[2] In the case of the ECMWF Reanalysis v5 (ERA5) dataset used in this analysis, wind speeds at 100 m (the relevant height for wind generation) are modelled using assimilations from aircraft and atmospheric sounding data for higher pressure levels, then extrapolating downward to

[1] We have used the terms "water vapour" and "moisture" interchangeably in this report.

[2] This is only the case for terrestrial winds. Modelled output for oceanic surface winds often assimilate ship and buoy observations (ECMWF, 2016).

the 100 m height (ECMWF, 2016). But this only represents discrete flight paths or locations. Satellite irradiance data is also assimilated for global coverage, but this in large part relies back on observations of water vapour, making wind velocities at least an extra step removed away from direct observation (ECMWF, 2016).[3]

- Starting from first principles, the atmospheric energy budget consists of (gravitational) potential, internal (excluding latent), latent and kinetic energy. Wind energy is affected by conversion of other forms of energy into kinetic. Because gravity is always directed downwards, conversion into potential energy can only be an intermediate step rather than an actual driver of the circulation (see Section 5.1.1). So conversions into kinetic energy ultimately derive from internal energy (related to temperatures) and latent energy (related to *atmospheric moisture*).

- There is also (in our opinion) strong theoretical justification for the existence of Condensation-Induced Atmospheric Dynamics (CIAD), where latent energy plays a dominant role in driving circulations, often with a contribution an order of magnitude higher than that attributable to temperature differences (see Section 2.5.3 and Appendix B.3). This is a theory which we actively investigate in our project.

1.6.2.2 | Interpreting atmospheric moisture findings in terms of wind

Where a link is not explicitly drawn between observed atmospheric moisture patterns and surface winds, the following heuristical principles apply:

- Direction of moisture transport in most cases should coincide with that of winds.

- Convergence of moisture and winds should in most cases coincide.[4]

- Cloud formation will often coincide with moisture convergence.

- The position of cloud liquid and rainfall may be offset from that of cloud formation, due to the effect of winds. If the source of moisture for the cloud can be deduced, then a judgement on wind direction can be made as the position of cloud liquid and rainfall should be downwind of the moisture source.

- Storms represent events of increased turbulence and extreme winds.

[3]Again, this is only the case for terrestrial winds. Modelled output for oceanic winds also assimilates satellite scatterometry data (ECMWF, 2016).

[4]We have used the terms "wind convergence", "atmospheric convergence" and "mass convergence" interchangeably in this report.

1.6.2.3 | Additional considerations regarding air flow in general

- Upward air movements from convergence must eventually descend due to gravity. To the extent that air mass is not lost to surroundings and there is no intervening phenomena, air descending nearby will in many cases diverge near the surface and return to the point of convergence for a closed circulation.
- Friction against air masses just outside the volume of this primary circulation may then induce a secondary circulation.
- Fluxes of convergence and divergence need not be parallel with the direction of flow. Even if two streams of air are flowing in the same direction, there can be localised changes in mass density which propagate from one stream to the other along the transverse direction.
- A corollary to fluxes of localised mass density anomalies[5] is a mass flux which *might* affect wind energy generation.

[5] "Anomalies" here in the meteorological sense as meaning distinct from background values.

2

Literature Review

This review broadly categorises the effects of LCC on SW into those resulting from vegetation cover change and those resulting from urbanisation, then examines these separately in the following subsections. The two cannot be completely dissociated since a loss of vegetation cover usually accompanies urbanisation. But a rough distinction can be made in that the latter pertains to effects particular to urban development that are not necessarily applicable to other LCC types and which is mainly described in terms of thermal and mechanical characteristics, while the former pertains to effects which can be attributed to changes in natural characteristics (which may be present even without urbanisation as in the case of vegetation loss) and incorporates biospheric feedback mechanisms.

2.1 | Methodologies for analysing the effect of land cover change

In a review of recent progress in NSWS change research in China (Zha et al., 2021), broadly categorised studies on the effect of LCC into Urban minus Rural (UMR), Observation minus Reanalysis (OMR) and Friction Wind Models (FWMs). UMR examines the difference between observational data from urban and rural weather stations. As it uses direct observations, results have higher fidelity than modelled results, but is particularly weak for regions where there is a lack of data (mainly rural areas and developing countries). OMR compares observational data against reanalysis with inputs simulating unchanged land cover. OMR methods can be used up to a global scale but the data can have model-introduced artefacts, especially at smaller spatial scales due to the coarse resolution of General Circulation Models (GCMs) (Zha et al., 2021). FWMs quantify effects based on simple dynamic models, but it ignores important effects such as turbulent flux, horizontal advection, temporal changes in horizontal winds, and is also difficult to use in complex terrain (Zha et al., 2021).

2.2 | Datasets and models

Studies have been complicated by the sparsity of AWS data (especially in rural areas and developing countries), as well as biases present in reanalysis datasets. Reanalysis datasets often overestimate Surface Wind Speeds (SWSs) (Fan et al., 2021), and there is an especially large disparity for Daily Maximum Wind Speeds (DMWSs) (Zhang et al., 2022, 2020). Zhang et al. (2019) found that SWSs from the Japanese 55-year Reanalysis (JRA55) reanalysis dataset had the closest agreement with observations in China, but Ramon et al. (2019) noted that this dataset has unusually high interannual variability, and that ERA5 instead offers the best agreement with observational wind speeds and interannual variability on a global scale. The latter is consistent with analysis by Torralba et al. (2017) which found that JRA55 displayed intensified trends.

2.3 | Observed changes in near-surface wind speed over the last few decades

2.3.1 | Slowdown and "global terrestrial stilling"

Much of the recent research regarding the effect of LCC on SW has been under the context of a global decline in NSWS observed in recent decades, a phenomenon which has come to be known as "global terrestrial stilling". LCC was heavily implicated as a cause for this NSWS decline, but recent analyses such as (Zeng et al., 2019) have identified a reversal in this decline at different periods for various continents, which along with other other evidence such as historical multidecadal declines found in centennial-scale reanalysis (Shen et al., 2021), suggests that large-scale oscillations in atmospheric circulations may be at play.

Most existing studies on LCC-NSWS interactions have been on the various regions of China, perhaps because of the country's rapid urbanisation eliciting stronger wind responses in recent decades coinciding with the rise of AWS NSWS measurements, and because of close monitoring accompanying large-scale afforestation efforts to combat wind erosion. Focus studies on regions outside of China have occasionally been conducted (summarised in Table 2.1), but these have yielded limited insights beyond what has already been learned in China. However, there has been a wealth of research on the climatic effects of LCC more generally and these often yield additional information into SW changes. A challenge in research has been to dissociate these changes and quantify the component which is due to LCC.

Table 2.1: A summary of research specifically studying SWS changes in a region outside of China (non-exhaustive).

Country (Study)	Time Period	Wind speed change (m/s/yr)
Australia (McVicar et al., 2008)	1975-2006	-0.009
India (Jaswal and Koppar, 2013)	1961-2008	-0.024
Portugal and Spain (Azorin-Molina et al., 2014)	1961-2011	-0.0016
	1979-2008	-0.001
Sweden (Minola et al., 2016, 2022)	1956-2013	-0.006
	1979-2008	-0.001
	1997-2003	-0.044
	2003-2019	-0.004
Saudia Arabia (Azorin-Molina et al., 2018b)	1978-2001	-0.0089
	2001-2003	+0.0057

Using weather station observations from 1960 to 1999, Li et al. (2008) found that NSWS in China decreased by 0.013 m/s/yr from 1960 to 1968, 0.023 m/s/year from 1969 to 1991 and 0.003 m/s/yr from 1991 to 1999 (punctured by changes in measurement instruments around 1970). Furthermore, the authors analysed the effect of LCC using the OMR method but with reanalysis data where surface observations of temperature, moisture and wind were omitted. They found that NSWS had a declining decadal trend north of Shandong irrespective of LCC, but that the exclusion of LCC south of Shandong resulted in an increasing trend instead. However, the methodology of excluding surface observations from reanalysis data to simulate natural land cover is controversial since it might not capture crucial surface properties, and rural weather station data availability was relatively sparse. Subsequent studies have then sought to quantify effects on a more nuanced basis such as by comparing between cities of different sizes and urbanisation rates (discussed later).

2.3.2 | Results confounded by instrument drift

It is important to note that part of these declines may in part be due to measurement drift in ageing anemometers. A study by Azorin-Molina et al. (2018a) compared new and old SEAC SV5 anemometers (the dominant anemometer model used by the Spanish Meteorological Agency since the mid-1980s), and found median biases of around 0.3 m/s. Assuming a linear drift over 30 years this could constitute around 0.01 m/s/year of wind speed changes (on the order of the observed declines), but results need to be interpreted carefully since not all studies made bias corrections and other regions use different anemometer models which are subject to different weather conditions. Furthermore, such drifts do not necessarily invalidate the attributed effects of LCC and large-scale atmospheric oscillations since observations on the geospatial variability of NSWS changes still implicate these factors (discussed in later subsections).

2.4 | The effect of urbanisation

2.4.1 | Urban minus Rural

Guo et al. (2011) found similar decreases in NSWS (0.025 m/s/yr from 1969 to 1990 and 0.006 m/s/yr from 1990 to 2005) as Li et al. (2008), and furthermore divided the results between urban and rural weather stations. The authors found a comparable rate of decrease between urban and rural from 1969 to 1990, a cotemporaneous decrease in the 850 hPa pressure-gradient force within the region from reanalysis data, and that much of this decline manifested in weaker strong wind events - the former two points suggesting that weakening winds were associated with large-scale atmospheric circulations.

2.4.2 | Wind speed anomalies

Guo et al. (2011) also discovered a temporary increase in urban wind speeds from 1990 to 1995 while rural winds were still decreasing, in spite of the fact that peaking Chinese urbanisation in the late 1980s to early 1990s would have increased urban frictional drag. The authors cited a similar discovery in southeast Queensland and northeast New South Wales, Australia by McVicar et al. (2008) and suggested the effect for further investigation. It's not clear whether there is a causal relationship between urbanisation and the wind speed increase, but a regional-scale urban Venturi effect is one possible explanation (although this would require further examination).

The wind increase from 1990 to 1995 could also be associated with enhanced turbulence mixing in momentum from a deepened Atmospheric Boundary Layer (ABL) and interactions with geostrophic accelerations, in what Droste et al. (2018) called an Urban Wind Island (UWI) effect. Droste et al. (2018) conducted simulations using a surface model with different urban local climate zones, along with a conceptual bulk model with idealised assumptions representing the mixed layer. The results showed that contrary to standard assumptions, "the mean wind in cities can exceed the wind in the rural surrounding", and that this UWI enhancement occurs primarily during daytime with a typical early afternoon peak of 0.5 ms-1.

2.4.3 | Extreme winds

Urbanisation may also influence the occurrence of extreme wind events. Results by Zhang et al. (2022, 2020) show a decline in DMWS in areas of China, with the highest declines observed in regions with high urbanisation rates. Furthermore, the decline was found in observational data but not reanalysis datasets such as NCEP-NCAR1 and ERA5, suggesting that changes are more likely a result of urbanisation than atmospheric circulation changes.

Furthermore, earlier analysis by Gero et al. (2006) studied the effects of LCC on storms in the Sydney Basin, Australia using numerical modelling simulations. The authors found little effect on frontal storms, greater horizontal accelerations over smooth agricultural land during convective storms, and that "in a special case, the dense urban surface of Sydney's city core appears to trigger an intensive convective storm." However, it isn't clear whether this manifests as an increased prevalence in storms and extreme wind events, nor whether this has been observed in other regions.

2.4.4 | Rate of urbanisation and size of cities

Building on previous work by Guo et al. (2011), Zha et al. (2017a) further examined the difference in China's NSWS declines between large and small cities. The authors found that the urbanisation rate of a city was positively correlated with greater NSWS declines, with a 10% higher urbanisation rate roughly associated with a 0.11 m/s faster decline. By first correcting for systematic errors then applying the OMR method, the authors found that the LCC could account for decreases of 0.057 m/s/yr and 0.030 m/s/yr in large and small cities respectively (despite large cities having a lower mean NSWS to begin with). The authors noted that comparisons were confounded by geographically uneven development and so studied adjacent large-small city pairs using the UMR method, again finding that LCC effects on large cities were more significant, but also that accounting for geographical uneven development in this way produced closer agreement with the OMR method. Interestingly, the authors found that the phase of annual and seasonal NSWS cycles were the same across both large and small cities - evidence that NSWS changes are not due to urbanisation alone but also large-scale atmospheric circulation changes.

In similar studies by the same authors, Zha et al. (2016, 2017b) divided up the results into 6 different wind speed categories and 4 climate zones, finding that urbanisation narrowed the NSWS probability distribution and led to a stronger decline in strong wind categories, consistent with earlier discoveries by Guo et al. (2011). Furthermore, it was found that the NSWS probability distribution of similar-sized cities were different across climate zones, again suggesting that a holistic account of NSWS changes needs to incorporate both the effect of LCC and regional climate change.

2.4.5 | Urban heating

Guo et al. (2011) also noted that temperature increases from urbanisation may affect the pressure-gradient force so that declining winds cannot be attributed to large-scale circulations alone, and indeed later analysis by Zhang et al. (2021) suggests a likely contribution from uneven heating. This is also consistent with earlier findings by Kitada et al. (1998), who conducted simulations using a mesoscale meteorological model and found that urban heating effects in the Nohbi Plain of central Japan established a pressure-gradient force adverse to topographically induced winds, resulting in a weak wind zone downwind of the urban area. Urban areas can also delay sea breezes through their drag effect, as was confirmed in numerical simulations by Rajeswari et al. (2022).

Simulation results for the Beijing-Tianjin-Hebei Region by Wang et al. (2020) using the OMR method in addition show a strong geospatial correlation between LCC and subsequently reduced NSWS. The results also showed seasonally-dependent modifications of mountain/valley and land/sea breezes, and that the magnitude of NSWS decline from urbanisation was relatively low during daytime. The last point is particularly interesting because analysis using observational data by Yu et al. (2009) found that wind speeds in this region and beyond are typically much higher during daytime, so when considered as a percentage of the mean wind speed the daytime NSWS decline relative to nighttime is even more dramatic. However, it is not clear what causes this effect.

2.4.6 | Summary

In summary, there is convincing evidence that the global decrease in NSWS over the last few decades was strongly associated with regional-scale atmospheric circulations. The slowing down then subsequent reversal of global stilling is indicative of a cyclical dynamic, and similar periods have appeared in centennial-scale studies. Furthermore, regional-scale 850 hPa pressure-gradients were found to decline during this time, there was a comparable magnitude in wind speed decreases between rural and urban areas during the recent stilling period, annual and seasonal cycles between large and small cities had the same phase, and similar sized cities had different probability distribution changes according to climate zone.

However, attempts to dissociate from this the effect of LCC have also found strong evidence that urbanisation had at least localised contributions. Several studies have found a positive correlation between magnitude of wind speed decrease and rate of urbanisation as well as city size. Aside from NSWS decline, urbanisation clearly also changes the SW resource in terms of local circulation patterns. Urban areas have seen changing convergence regions, wind speed increase anomalies and weakening of the pressure-gradient force. Modelling further suggests the possibility of wind speed enhancement within an urban area (UWI effect), compensatory increases in its periphery, and changes in extreme wind patterns - all of which require further research.

2.5 | Vegetation-atmosphere interactions and the effect of agricultural expansion

2.5.1 | Roughness length changes

Vegetation has the obvious effect of increasing surface roughness and hence imparting frictional drag upon SW. Afforestation efforts in China were in part deliberately targeting reduced local wind speeds in order to combat wind erosion, with research finding that vegetation cover of at least 10% was necessary to reduce wind speeds (Jiang et al., 2019). In contrast with urban constructions, mechanical characteristics in vegetation cover display more pronounced seasonal characteristics. For example, using an old oak stand in a forested area in Schweinfurt, Germany, Geiger (1950) found that although wind speeds below the tree crowns decreased upon leafing, wind speeds above the crown saw a significant increase - possibly a manifestation of the Venturi effect.

Mesoscale modelling studies have also suggested that large-scale deforestation in

Australia over the last 200 years has significantly changed near-surface wind patterns and that some of these effects have even been vertically propagated (Narisma and Pitman, 2003). In the case of southwest Western Australia, similar modelling by the same authors has suggested increased horizontal wind speeds (owing to reduced roughness length) and decreased vertical velocities in areas with LCC, but increased vertical velocities inland of these areas associated with changes in where winds converge (Pitman et al., 2004).

2.5.2 | Surface temperature, pressure and energy balance

2.5.2.1 | The Bunny Fence Experiments

An interesting experimental study was conducted by Nair et al. (2011) around the rabbit-proof fence in southwest Australia which sharply delineates native vegetation cover on the eastern side from agricultural land on the western side. The authors used a mix of OMR methods, regional atmospheric numerical modelling, aircraft observations and 3-hourly paired radiosonde releases (20 km east and west of the fence) to examine meteorological differences between vegetation cover types within the summertime and wintertime west coast trough of Australia.

The results show significantly deeper convective development over native vegetation associated with increased cloud cover and a deeper ABL (to heights greater than the lifted condensation level). The results also show that a lower mean sea level pressure would be present on the western side of the fence had it still been native vegetation instead of agricultural land, that surface convergence would have occurred closer to this lower pressure region, and that wind field anomalies correlate well with anomalies in ABL height, precipitation and surface convergence. This is consistent with simultaneous radiosonde and modelling studies in the Amazon rainforest by Wang et al. (2009); Xu et al. (2022), who found lower and more shallow cloud cover over deforested areas also associated with ABL height changes.

Interestingly, the results by Nair et al. (2011) also show that latent heat fluxes above native vegetation do not vary substantially between summer and winter (unlike agricultural vegetation), suggesting a controlled regime with biophysically damped changes in evapotranspiration and subsequent condensation above native vegetation. Such effects are important since convective developments often drive SW, while the ABL height affects among other things the vertical wind shear and presence of low-level jets, and understanding of the latter's effect on winds has in fact been identified as an area of increasing importance for the wind energy and meteorological communities (Peña et al., 2013).

Earlier results in the Bunny Fence Experiment series include contributions by Lyons (2002); Lyons et al. (1993, 1996, 2001); Ray et al. (2003), with the dramatic delineation in atmospheric conditions best illustrated in Figure 2.1.

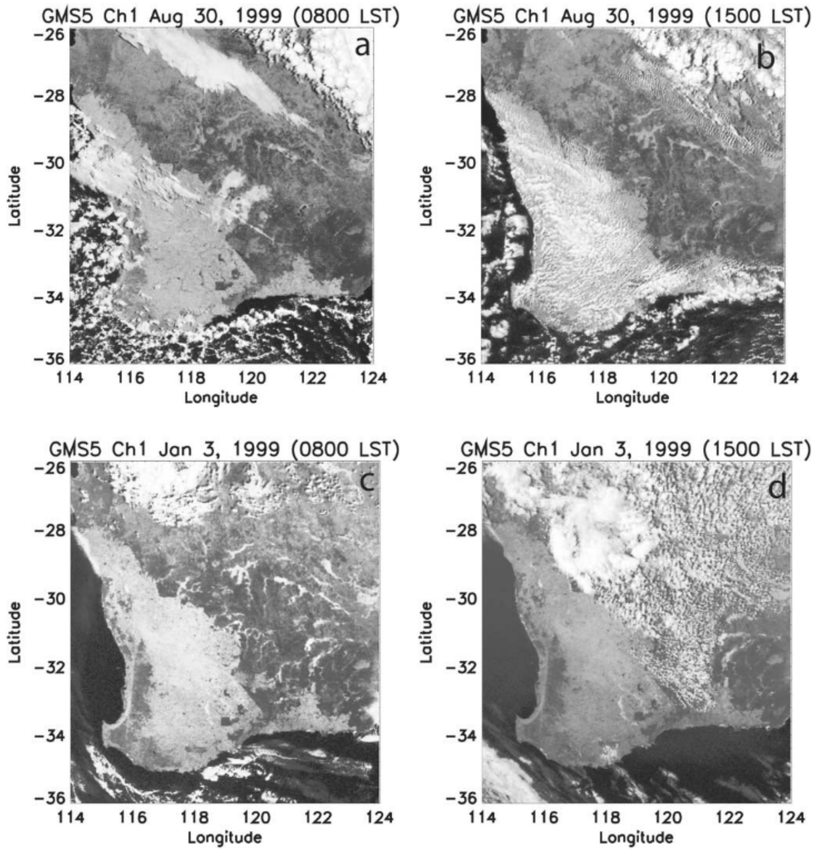

Figure 2.1: "Preferential development of cumulus clouds in Southwest Australia. (a and b) The preferential development of cumulus clouds over agricultural areas from 0800 to 1500 LT during the winter agricultural season. (c and d) The preferential development of cumulus clouds over native vegetation from 0800 to 1500 LT during the summer dry season." Image and caption copied directly from Ray et al. (2003).

2.5.2.2 | Mesoscale circulations and vegetation breezes

There are even internal inhomogeneities within contiguous regions under a single land cover classification. In studying Yatir Forest, Israel, Kröniger et al. (2018) found that older and denser growth regions had higher temperatures and produced stronger updrafts for weakly and strongly convective scenarios, pushing up the ABL height and establishing a low pressure area leeward from the older growth at half the ABL height. Being a planted pine forest in an arid region, Yatir Forest had lower albedo, higher net radiation and twice the sensible heat flux (latent flux was negligible in this arid area) compared to the surrounding shrubland. Thermal convections were stronger over the forests (particularly over the older growth areas) which in turn triggered secondary circulations which were coupled with the surrounding shrubland.

A comprehensive review of research on the biogeophysical aspects of LCC-climate interactions by Mahmood et al. (2014) also concluded that "biogeophysical impacts of LCC on local and regional-scale are significant, undeniable and discernible." On effects pertaining to the wind resource, the authors noted discoveries such as convective clouds developing first over moister vegetated surfaces then secondly over neighbouring dry wheat in humid weather but the converse for a dry atmosphere, increased probability of dust devil formation over cleared agricultural land, and the presence of mesoscale circulations where there is a gradient or abrupt transition in vegetation cover.

The last point is consistent with work by Hong et al. (1995); Zhuojia and Xinyuan (1995) using mesoscale biophysical, meteorological models. The results suggested the presence of vegetation breezes at the interface between well irrigated crops and bare soil, arising from a horizontal pressure gradient which is established by uneven surface heating and turbulent mixing in the atmosphere forcing the relatively cold and humid air produced near the canopy by evapotranspiration.

A mesoscale modelling study by Mahmood et al. (2011) in Western Kentucky, USA similarly found mesoscale circulations along land cover discontinuities and increased ABL height over forest cover. Interestingly, in a comparison between existing land cover and increased forest cover, the results also suggested in the latter case the presence of increased vertical wind speeds and horizontal velocities towards the regions of increased forest cover (convergence) - again suggesting a relationship between vegetation cover and distant advection.

2.5.2.3 | Temperature and winds

Observations over a 5-year period by Lapworth (2003) at a flat rural inland surface on arable land in Bedfordshire, England found a linear relationship between NSWS during evening cooling and screen temperature measured relative to the evening transition. A follow-up study then found that this linear relationship also held for morning heating and that the slope of this relationship showed little change with heating rate, suggesting that NSWS during boundary layer transitions were in quasi-equilibrium with temperature (i.e. there was little evidence for temperature-independent temporal fluctuations)

(Lapworth, 2006).

He et al. (2013) analysed wind and temperature from 2007 to 2011 at heights of 10, 20, 40, 80, 140 and 200 m using observational data from a meteorological mast in Cabauw, Netherlands (situated in open, flat pastureland). The authors compared the wind speed probability distributions between clear-sky and low-cloud conditions for daytime and nighttime (as determined using a simple algorithm on ceilometer data). The results show a reduced vertical gradient in potential temperature and wind speed during daytime hours, especially for clear-sky conditions - evidence of momentum mixing by thermally-driven turbulence. However, these focus studies were all on flat rural cropland and it's not clear whether these results hold for other types of land cover.

2.5.3 | Condensation-induced atmospheric dynamics

2.5.3.1 | Theory

Condensational force, power and pressure gradient In a series of papers, Makarieva and Gorshkov (2009b) derived from fundamental thermodynamics principles the existence of what they termed an "evaporative-condensational force" (Makarieva and Gorshkov, 2010) with associated "condensational power" (Makarieva et al., 2014), and applied this over natural forests (where there is huge amounts of evapotranspiration sustaining this proposed mechanism) to suggest that this is a major driver of atmospheric circulations (Makarieva et al., 2013b).

This theory holds that upon atmospheric condensation (when the mass density of H_20 shrinks upwards of a thousandfold), there is an associated drop in the partial pressure of water vapour and hence pressure of air in general. Local to the point of condensation is an ascension of air from the upwards directed evaporative-condensational force. Over large-scales, this manifests as a horizontal pressure gradient, sustained by condensational power, which affects or gives rise to atmospheric circulations.

The Biotic Pump The authors further theorise that forests play an active role in maintaining a higher rate of atmospheric condensation above land than sea (through evapotranspiration from high leaf surface area), so as to advect oceanic moisture inland to replace gravity-induced runoff, in what is known as the "Biotic Pump" (Makarieva et al., 2009, 2013a). On top of sound (personal judgement) theoretical physics, Makarieva et al. (2009, 2013a) propose as empirical evidence a set of coast-to-inland transects which demonstrates a sudden increase in precipitation (implicit increase in atmospheric and moisture convergence) from ocean to coast which then remains relatively uniform with inland distance over intact forests.

The results also show a seasonality which corresponds with forest activity: the Amazon which is active year round controls annual precipitation with tamed season variability, while the Eurasian forest displays precipitation which is greater than that over ocean and is uniform with inland distance only during boreal summer (Makarieva et al., 2013a). The seasonal variability in the latter is especially distinct, with terrestrial precipitation which is not only lower than that over ocean in winter, but which also decreases exponentially with inland distance (Makarieva et al., 2013a). Meanwhile, degraded or unforested areas such as Australia display a year-round precipitation which is less than over ocean and which undergoes exponential decay with distance, with minimal seasonality(Makarieva et al., 2009, 2013a).

Controversy This theory has attracted controversy in part because it goes against the standard view that atmospheric circulations are driven primarily by temperature gradients. In this picture, warmer air rises and leaves behind a low pressure region at the surface, the rising air eventually sinks to create a high pressure region at a neighbouring surface, then surface winds flow from high to low surface pressure. Although it is well-established that this effect exists, theoretical models predict wind energies which fall short by an order of magnitude compared with observations for planetary-scale circulations such as the Hadley cell (Caballero et al., 2008; Held and Hou, 1980; Makarieva et al., 2013b; Schneider, 2006), down to toy-scale circulations in a purpose-built enclosure specifically investigating this effect (Bunyard et al., 2015, 2017, 2019).

Criticisms have also been formulated on physical grounds regarding whether the evaporative-condesational force is theoretically sound[1], one of these being that condensation should induce isotropic net flows which cancel each other out (Bunyard et al., 2015, 2017). However, a series of experiments by Bunyard et al. (2015, 2017, 2019) convincingly demonstrates that anisotropic flow is possible, and anistropic flow from cloud formation is in fact regularly targeted by paragliders for additional lift (Pagen, 1992, 2001) (see Section 2.5.3.2). Furthermore, there are good heuristical justifications for why anisotropic flow should result (see Appendix B.3).

2.5.3.2 | Observational evidence by paragliding community

Unpowered aircraft enthusiasts have long noted strong lift forces due to condensation near cloud base in a phenomenon known as "cloud suck" (Gadd; Pagen, 1992, 2001), with close-up video evidence also showing a thinned column at the point of conden-

[1] See exchanges between Meesters et al. (2009) and Makarieva and Gorshkov (2009a), as well as between Jaramillo et al. (2018, 2019) and Makarieva et al. (2019).

sation resulting from horizontal air advection (Benz, 2021b). Also striking is the observation that rising air parcels generating lift exist even on overcast days with little surface heating, with greater prevalence at higher altitudes (Benz, 2021a; Rejmanek, 2018). Given that latent heat release occurs above cloud base, and in light of work by Gordon et al. (2003); Jiang and Liang (2013); Yan and Zheng-Hui (2013); Zhang et al. (2016) strongly suggesting a causal relationship from vegetation cover to water vapour availability via evapotranspiration, vapour pressure drops from condensation may play a mediating role between vegetation cover and long-range advection as suggested in theoretical work by Makarieva et al. (2013b).

2.5.3.3 | Satellite observations display preferential atmospheric convergence over *current* forest cover

Results from the transect studies by Makarieva et al. (2009, 2013a) are corroborated by satellite video feeds from EUMETSTAT (2018). Video from EUMETSTAT (2018) shows that terrestrial cloud formation occurs almost exclusively over *current* forest cover. If forest growth was just a passive byproduct of geophysical forces with little influence from forest cover, then there is no reason why clouds shouldn't also form over areas cleared by human activity over recent centuries. So even if forest cover does not actively regulate atmospheric convergence, evidence points towards a modulating effect.

Careful inspection of video from EUMETSTAT (2018) also reveals a regular diurnal cycle in cloud cover over forests, typically peaking around the evening ABL transition. There is also marked seasonality in this cloud cover for forests outside of the tropics.

2.5.3.4 | Reanalysis of water vapour flows

(Li et al., 2020) found that increased vegetation induced a strengthening of winds favourable for water vapour transport towards South China, slow the eastward progression of Rossby waves, and that "In addition to local cooling effects, spring greening was found to cause a decrease in geopotential height ... which exerts a significant influence on Ta [surface air temperature] in the Arctic via atmospheric teleconnections ... pressure gradients between the Arctic and China are reduced proportionately, resulting in a reduction in the strength of the westerlies over Mongolia." Interestingly, the authors also found that "Biophysical feedback from atmospheric circulation only emerge over Southeast China, where total cloud cover increases", and in supplementary figures 5 to 8 present a series of graphs where higher wind speed changes appear to have a geospatial correlation with higher changes in latent energy, humidity and Precipitable Water (PW). These results together suggest that biospherically mediated water vapour condensation may have a significant effect on the SW resource, consistent with theoretical formulations by Makarieva et al. (2013b).

Interestingly, similar geospatial correlations seem to appear in earlier OMR results by Zhao and Pitman (2002) which mostly simulated natural vegetation cover loss. By selectively subtracting the changes in 1000 hPa wind velocity between different simulations (each which had different regional exclusions) and comparing by visual inspection, the results seem to indicate that were India and China to have retained their natural vegetation cover then changes in oceanic wind velocities would be biased towards these landmasses themselves. Similar subtraction of latent heat flux results between scenarios suggests an increase in latent heat flux for these same landmasses.

An even earlier study by the same authors (Zhao et al., 2001) using a similar methodology identified regions with increased precipitation resulting from LCC, and the direction of changes in 1000 hPa wind velocity appears to also point towards these regions in December-January-February (DJF). Since latent heat flux is indicative of condensation and subsequent precipitation, biospheric interactions with the hydrological cycle are again implicated for wind speed changes. It could also be argued that converging winds cause condensation into clouds (and hence an increase in latent heat flux) rather than the other way around, but this does not explain why there would be an increase in convergence towards where natural vegetation cover was simulated.

Consistent with this finding and also the strengthening of winds towards South China described in (Li et al., 2020) are findings by Matthew and Ohunakin (2017) who used a regional circulation model interfaced with general circulation, mesoscale, radiative transfer and biosphere-atmosphere transfer models to simulate the effect of 7 hypothetical afforestation scenarios on the wind resource of Nigeria. The results suggest a country-wide decline in wind power density in the 4 scenarios where afforestation has random geographical distribution, which the authors attributed to increased surface roughness and weakened temperature gradients. But interestingly the results also suggest that for the 3 zonal afforestation scenarios (where afforestation is concentrated in a single horizontal band across the north, middle or south of the country), there is an increase in wind power density upwind of the afforested area.

By comparing simulations of an ocean-atmosphere-land model with or without coupling to the Atmosphere-Vegetation Interaction Model (AVIM) over a 50-year period, Zhi et al. (2009) found that “the model coupled with AVIM enhances the simulative capability for interannual variability [of atmospheric circulation] and makes the annual cycle variability more apparent.” and that “different vegetation types have different correlations between NPP [net primary production] and the climate”. The authors also found a positive cotemporaneous correlation between the 850 hPa wind fields with precipitation as well as Net Primary Production (NPP) during June-July-August (JJA) from East Asia to the western Pacific Ocean (East Asian monsoon). It could be argued that stronger monsoonal winds bring in more water which is then more conducive towards plant growth. However, that the correlation between NPP and atmospheric circulation is dependent on vegetation type, and that the result is based on inclusion of the AVIM, suggests that the correlation is in part due to biospheric influences.

2.5.3.5 | Positive feedback between convection and cloud formation

As it is uncontroversially the case that uplift of moist air promotes cloud formation, CIAD also implies a positive feedback between convection and cloud formation.

Convective memory Cloud-resolving simulations by Tompkins (2001a,b) suggested the existence of positive feedback between convection and water vapour which may have significant effects on larger-scale ocean-atmosphere dynamics. The author also found that "water vapor plays an active role in determining the location of convection", with an especially critical role at the lower troposphere layer in convection control, and that the feedback is weakened when wind shears advect dry air.

In results supportive of these findings, Colin et al. (2019) studied the dependence of convection behaviour on its own history (convective memory) using idealised cloud-resolving simulations under scenarios of unorganised, wind shear organised and self-aggregated convection. In their simulations the authors selectively homogenised different microstate variables without changing the macrostate then observed the convection's evolution, finding that water vapour makes up the dominant part of storage (as measured by the time taken to resume the original convection).

In similar simulations but with different heights, Colin et al. (2019) also showed that the dominant contribution to memory came from the subcloud and shallow cloud layers, with the subcloud layer larger by a factor of 2 in the unorganised case, the shallow cloud layer larger by a factor of 2 in the wind shear organised case, and roughly equal contributions in the self-aggregated case. The authors concluded that "This suggests memory comes from processes that contribute to the spatial variance of low-level moist static energy (MSE) and/or make convection sensitive to it. This includes cold pools, hot thermals, and other rain-associated thermodynamic processes such as rain evaporation, and supports parameterizations coupling convection to these processes.", but to this could also be added the thermodynamic effects of water vapour condensation (which occurs mainly at the subcloud and shallow cloud layers).

Experimental understanding is scarce Despite all this, there remains a lack of understanding regarding: how significant these biospheric influences really are on larger spatial scales, what are the relevant intermediate mechanisms which give rise to observed biosphere-hydrosphere-atmosphere couplings, and how to quantify any such effects. Li et al. (2020) also listed as uncertainties the contribution of vapour pressure deficits, leaf water potential and aerosols. In a review of Europe's wind energy potential, European Environment Agency (2009) singled out forested areas and mountainous regions to be "where model prediction and observed wind velocities differed most". These also happen to be areas associated with both a relatively intact biosphere and significant condensation leading to high levels of cloud cover.

In summary, vegetation cover has complex interactions with SW beyond just imparting frictional drag. Research has strongly established the existence of vegetation-atmosphere coupling and this appears to be mediated through the hydrological cycle, possibly due to condensation-related effects, but there is still a lack of understanding on how these interactions work or how strong these interactions are. Forest cover and intact native vegetation display very different effects as compared with agricultural land. Modelling even suggests the possibility of changed horizontal pressure-gradients and distant advection towards natural vegetation cover, but further research is necessary to validate this. Vegetation cover change is furthermore associated with changes in ABL height, convective activity and mesoscale circulations but again research understanding of this remains limited.

3

Methodology

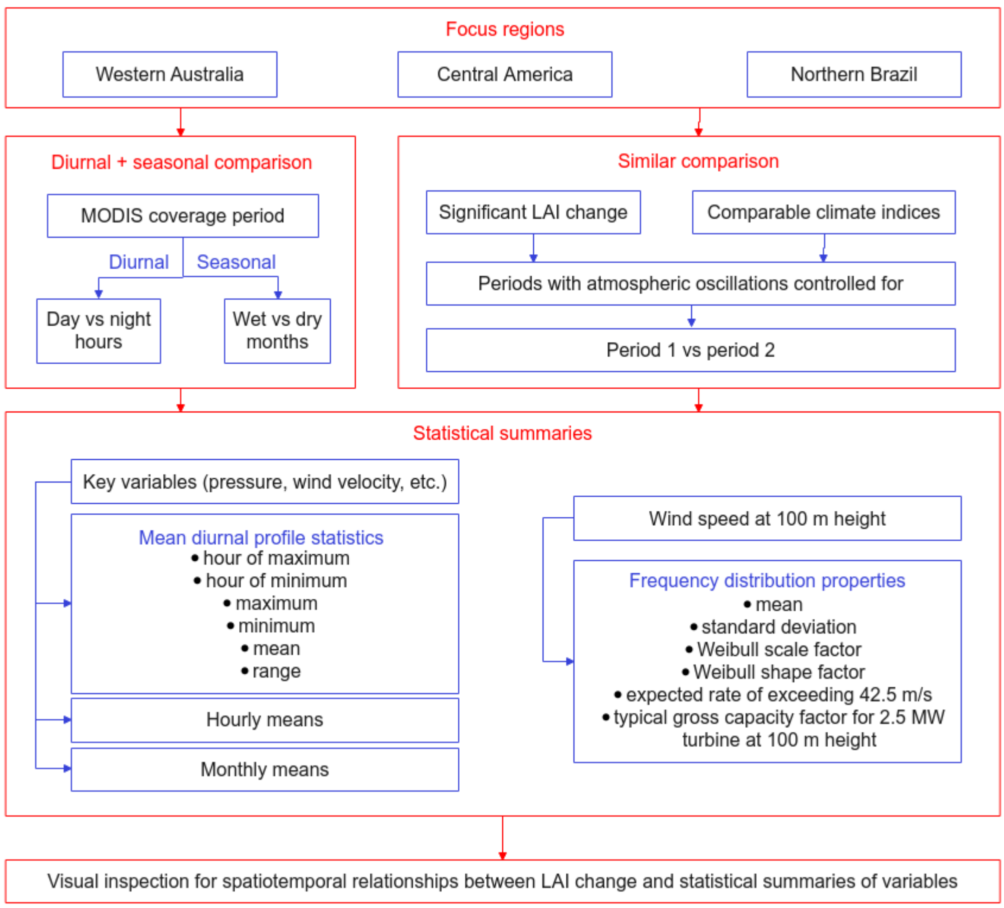

Figure 3.1: Flow chart summary for methodology. Results for all focus regions were obtained but only Western Australia was analysed due to project scope change (see Appendix A.5).

3.1 | Approach

3.1.1 | Spatiotemporal correlations

To identify how vegetation loss may affect (or has historically affected) surface winds, we produced a series of spatial plots using Global Land Surface Satellite (GLASS) data (Liang et al., 2021) and ERA5 data (Hersbach et al., 2019). These plots sought to uncover any spatiotemporal correlations between vegetation loss and key atmospheric variables such as wind speed, wind direction and mean sea level pressure. The rationale behind this was that were there to be any concrete spatiotemporal correlations, it would suggest strongly that there is some underlying dynamic between the variables (since a concrete pattern manifesting through both space and time purely by chance is unlikely), which may then shed some insight into how atmospheric circulations may change in the future.

In doing this, we first identified a focus region which was likely to yields meaningful results due to historically extensive degrees of vegetation change or other unique circumstances such as having a sharp delineation between natural and agricultural land cover. For this region, we produced three separate comparisons.

3.1.2 | Diurnal comparison

The first comparison was between the daytime and nighttime hours (which can have significant differences depending on land cover) for the period from Jan-2001 to Dec-2020[1] (years in which available GLASS data was most reliable due to an advancement of instruments), and will hereby be referred to as the "diurnal comparison".

3.1.3 | Seasonal comparison

The second comparison was between the dry and wet seasons (which can have significant differences in vegetation). also for the period from Jan-2001 to Dec-2020, and will hereby be referred to as the "seasonal comparison".

3.1.4 | Similar comparison

For the third and final comparison, we strategically selected two 5-year long historical periods with similar atmospheric conditions but extensive vegetation change, hereby

[1] All period start and end dates in this report are inclusive unless otherwise stated.

referred to as the "similar comparison". Periods for the similar comparison were selected in such a fashion so as to control (to the extent possible) for other effects such as atmospheric oscillations which may also affect the key atmospheric variables of interest (mainly wind speeds, wind velocities and mean sea level pressure).

For each of these three comparisons, we then created a series of spatial plots displaying summary statistics for the key atmospheric variables (see Section 3.4), as well as differences in these statistics between seasons or periods (other related variables which might affect the behaviour of the key variables were also studied).

3.1.4.1 | Mean diurnal profile

Central to these summary statistics was a variable's Mean Diurnal Profile (MDP) over each period, produced using a group-wise average by hour of day for all the data values in that period. This was computed for each grid cell in the data, and was used to study how vegetation change might affect the diurnal variations in key variables. Because of the difficulty in visualising the temporal variability in spatial data, we created plots for the hour of maximum, hour of minimum, maximum, minimum, mean and range of these MDP values. We also created spatial plots for the mean values over each hour of the day and month of the year, to analyse cotemporaneous diurnal and seasonal evolution of different variables respectively.

3.1.4.2 | Wind speed distribution

In addition to this, we created spatial plots for the wind speed distributional properties over each period (and the difference in these values between periods) for the wind speed at 100 m above surface such as its standard deviation, gross capacity factor for a typical wind turbine with 100 m hub height, empirical fits for the Weibull parameters, and the expected rate of exceeding 42.5 m/s (the typical speed which a turbine can withstand for 10 minutes).

3.1.5 | Visual inspection for trends

Spatiotemporal correlations were then identified by visual inspection as this was deemed more appropriate than a rigid statistic metric, since the latter will have to be computed upon gridded data and hence may miss spatial correlations between variables which are present but manifest slightly offset from each other by a few grid cells (and it is a non-trivial task to systematically correct for all the different spatial variations by which two variables can be slightly offset from each other, if possible at all).

3.2 | Focus region

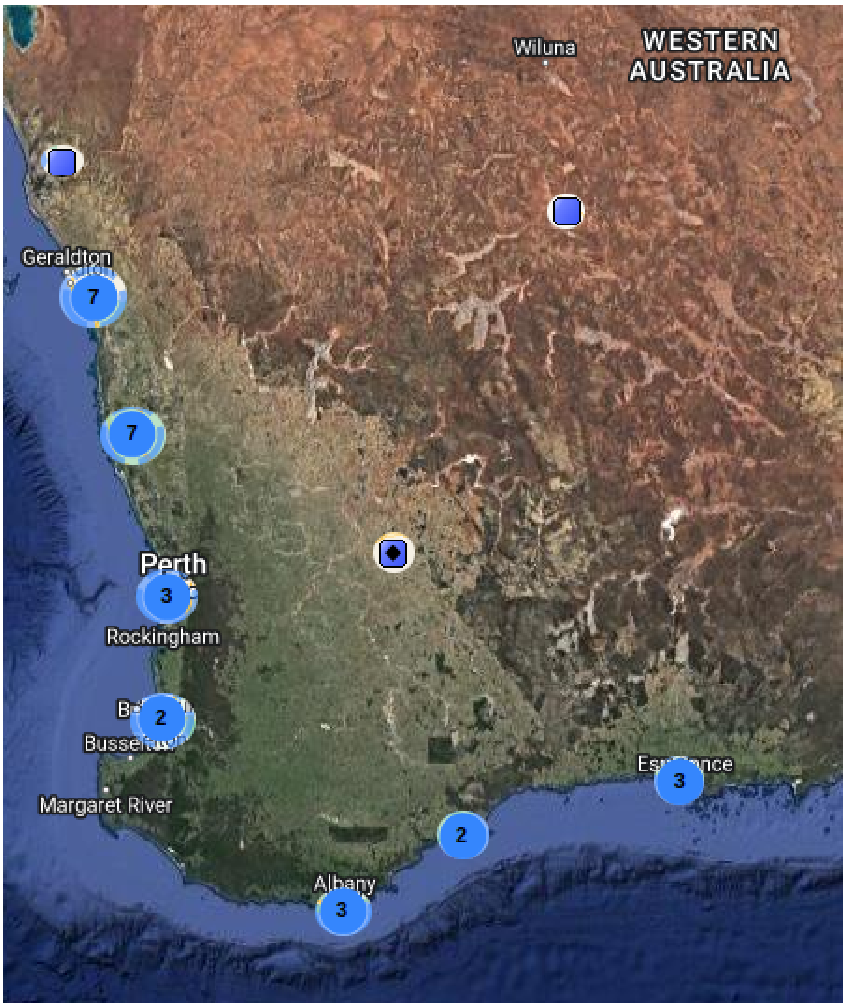

Figure 3.2: Satellite image displaying Western Australia focus region from 114°E to 124°E longitude and 36°S to 6°S latitude (Google Maps, 2022c). Markers indicating positions and number of wind farms have been edited on using data from (The Wind Power, 2022h). The State Boundary Fence of Western Australia sharply delineates agricultural vegetation on the west from native vegetation on the east.

3.2.1 | Description of region

We selected the south-west part of WA (from 114°E to 124°E longitude and 36°S to 6°S latitude; see Figure 3.2) for investigation because previous studies (Esau and Lyons, 2002; Lyons, 2002; Lyons et al., 1993, 1996; Ray et al., 2003; Xinmei et al., 1995) have suggested significantly different atmospheric conditions on each side of the SBFWA, which itself sharply delineates native vegetation (eastern side) from agricultural land (western side). The entire focus region is on the order of 1000 km, so synoptic weather features (which have a characteristic scale of this order) are less likely to produce contrasting effects over the different subregions.

Land surface characteristics on the agricultural side exhibit pronounced seasonal fluctuations due to the annual growing and harvest of wheat, after which the ground is left bare before the next growing season. This occurs along what is called the Wheat Belt Region of Western Australia (see Figure 3.3) where land usage has remained largely the same over recent decades. An excellent description of the terrain near Lake King (around the straight part of the fence) is provided by Lyons (2002):

> The native vegetation is characteristically a woodland called mallee with *Eucalyptus eremophila* the most consistent species. Patches of eucalypt woodland occur on lower ground and scrub heath and casuarina thickets are found on the residual plateau soil. The topography is gently undulating country of low relief with duplex mallee soils - that is, sand overlying clay. The native vegetation is between 0.5-6 m high, with more than 75% of this vegetation between 0.5-2 m. The adjoining farmlands cultivate winter growing annual species. Wheat is the major crop in the agricultural area and grows between May and November. Crops are generally less than 1 m high during the growing season and after harvest stubbles of about 20 cm or bare soil are common.

3.2.2 | Significance of results from this region

This focus region was selected mostly for these unique characteristics which are conducive towards eliciting insights into the general principles tying land cover with atmospheric circulation, but may also have some direct implications for wind farms in the area, most of which are situated along the coast (see Figure 3.2). Vegetation change on an annual to decadal scale has been concentrated along the south-western coastal forests (see Figure 4.12), while effects on a seasonal scale will be most pronounced along the fence. Wind farms around these subregions are the ones most likely to see a change in wind resource due to continued forest loss and future agricultural expansion respectively.

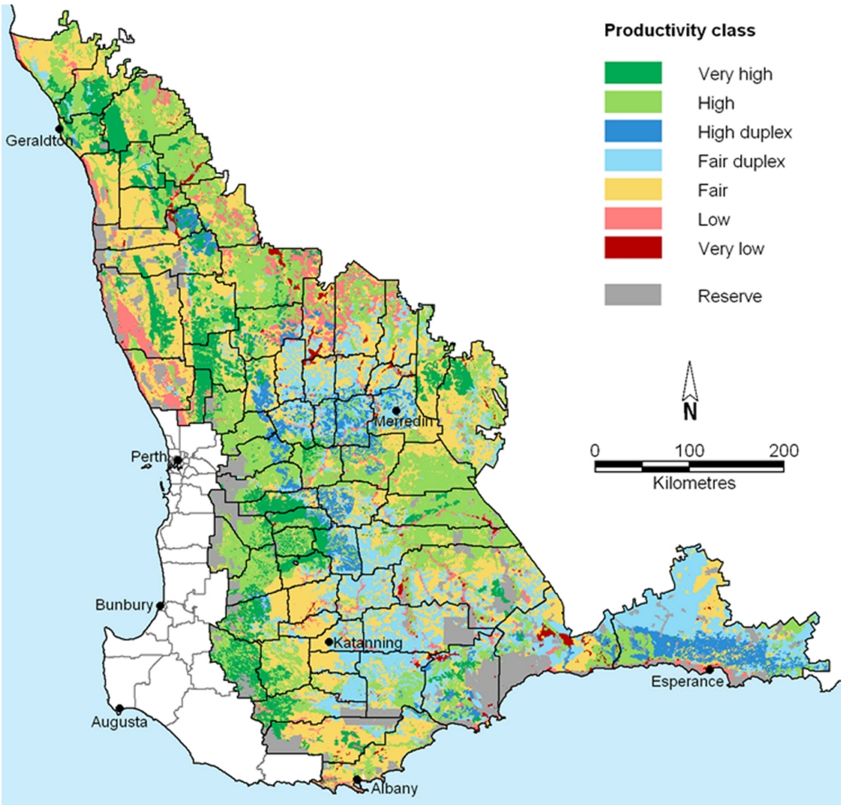

Figure 3.3: The Wheat Belt of Western Australia, with shading indicating level of productivity (WA Department of Primary Industries and Regional Development, 2021a).

3.3 | Study periods for each comparison

3.3.1 | Diurnal and seasonal comparisons

The diurnal and seasonal comparison were performed over the period from Jan-2001 to Dec-2020 (inclusive). The GLASS products derived from Moderate Resolution Imaging Spectroradiometer (MODIS), the more advanced instrument, begin around Mar-2000, with the Leaf Area Index (LAI) dataset ending Dec-2021 while the Fraction of Photosynthetically Absorbed Radiation (FAPAR) dataset ends Dec-2020 (at the time of writing). As averages starting from Mar-2000 and ending Dec-2020 would have skewed weightings for the months of January and February, we elected to use Jan-2001 as the period start instead.

The local timezone for WA is UTC+8. Where comparisons between "daytime" and "nighttime" hours have been made, the average values for hours from 8 am to 3 pm

Local Time (LT)[2] (8-9-10-11-12-13-14-15) have been selected as representative of daytime, while the average values for hours from 8 pm to 3 am local time (0-1-2-3-20-21-22-23) have been selected as representative of nighttime. Meanwhile, based on historical precipitation climatology, the months of JJA and DJF were selected as being representative of the wet and dry season respectively.

3.3.2 | Similar comparison

To control for differences arising from atmospheric oscillations, and to select periods for which there was sufficient vegetation change for meaningful results to appear, we selected a set of study periods based on the following criteria (in order of priority):

1. 5-year rolling averages for relevant climate indices were similar or at a similar phase in the oscillation
2. Change in LAI between the periods was extensive or had opposite trends in different subregions
3. Monthly values for relevant climate indices over each period displayed a similar time evolution pattern
4. Periods covered a similar amount of time spent in La Nina / El Nino events (where relevant) and Negative / Positive Indian Ocean Dipole (IOD) events (where relevant)

Period lengths of 5 years were selected since this somewhat averages out the effect of shorter-term atmospheric fluctuations. To assist in the selection of periods, we created 5-year rolling average line plots for all major climate indices (see Section 3.3.2.1) but with a focus towards those corresponding to the focus region's relevant (i.e. climate-driving) atmospheric oscillations. We also created yearly spatial plots for the 5-year rolling average of the annual difference in Mean Leaf Area Index (MLAI) (see Section 3.3.2.2).

3.3.2.1 | Climate indices

5-year rolling average line plots were produced for the following climate indices using monthly data obtained from National Oceanic and Atmospheric Administration (NOAA) (NOAA-PSL and NOAA-CPC, 2022):

[2]Unless otherwise stated, all times in this report are expressed in local time, and hour endpoints are inclusive.

- Atlantic Multidecadal Oscillation Index (AMOI), for the Atlantic Multidecadal Oscillation (AMO)
- Pacific Decadal Oscillation Index (PDOI), for the Pacific Decadal Oscillation (PDO)
- Oceanic Nino Index (ONI), for the El Nino-Southern Oscillation (ENSO)
- Dipole Mode Index (DMI), for the IOD
- Antarctic Oscillation Index (AAOI), for the Antarctic Oscillation (AAO) / Southern Annular Mode (SAM)
- Arctic Oscillation Index (AOI), for the Arctic Oscillation (AO) / Northern Annular Mode (NAM)
- North Atlantic Oscillation Index (NAOI), for the North Atlantic Oscillation (NAO)
- Eastern Pacific Oscillation Index (EPOI), for the Eastern Pacific Oscillation (EPO) / Northern Pacific Oscillation (NPO)

Overlayed upon the ONI graphs were windows indicating when La Nina and El Nino events have occurred in the past, as defined by the Japanese Meteorological Agency (JMA).[3] And overlayed upon the DMI graphs were windows indicating when Negative IOD and Positive IOD events have occurred in the past, as defined by JMA.

3.3.2.2 | Annual difference in mean leaf area index

For each calendar year with completed data in the GLASS dataset, an annual mean value was computed for the LAI at each grid point. The annual difference in MLAI for each year was then defined as the MLAI for that year minus the mean of the previous year. A 5-year rolling average centred upon each year was then produced by averaging the four annual differences calculated across the five annual means. For example, the 5-year rolling average for the year 2002 would be the average of $MLAI(2004) - MLAI(2003)$, $MLAI(2003) - MLAI(2002)$, $MLAI(2002) - MLAI(2001)$ and $MLAI(2001) - MLAI(2000)$, where the MLAI over a given year is expressed as $MLAI(year)$.

This averages out the shorter term fluctuations which may be due to rainfall anomalies around a mean trend, or other factors such as changes in cropping. Although interesting in their own right, these are only indirectly related to LCC (the subject of this report) and so are not pursued.

[3] Note that different meteorological agencies define these events differently. JMA definitions were used here because it was the only data down to a monthly resolution which was easily obtainable.

As the time difference between similar periods in terms of climate indices often exceeds 5 years, these plots were used only as a visual indicator to aid the selection process (to determine whether periods with sufficiently similar climate indices would also have extensive enough vegetation change to be worth studying). For final confirmation, separate comparison plots for the MLAI over each of the selected 5-year periods were produced.

3.4 | Variables selected for analysis

3.4.1 | Main study variables

The Land Surface Elevation (LSE) and Slope of Sub-Gridscale Orography (SSGO) were static variables derived from the ERA5 dataset, used to identify whether orographically-induced circulations would be a confounding factor. Mean Leaf Area Index (MLAI) was the primary metric used to assess the extent of vegetation change, with Mean Fraction of Photosynthetically Absorbed Radiation (MFAPAR) a secondary metric to corroborate results.

We then selected out for analysis the ERA5 variables which were most relevant to our research goals. A full list of these variables is presented in Table A.1 and also included are descriptions for wind speed distribution properties derived from ERA5 data (see Section 3.5.4). But the main ones presented in the results are:

- Mean Sea Level Pressure (MSLP)
- Wind Speed at 100 m Above Surface (WS100)
- Hourly Change in Wind Speed at 100 m Above Surface (dWS100)
- Wind Velocity at 100 m Above Surface (WV100)
- Hourly Change in Wind Velocity at 100 m Above Surface (dWV100)
- Temperature at 2 m Above Surface (T2)
- Hourly Change in Temperature at 2 m Above Surface (dT2)
- Vertical Integral of Energy Conversion (VIEC)
- Net Atmospheric Condensation (NAC)
- Vertical Integral of Divergence of Moisture Flux (VIDMF)

- Net Surface Evaporation (NSE)
- Vertical Integral of Kinetic Energy (VIKE)
- Forecast Albedo (FA)
- Surface Sensible Heat Flux (SSHF)
- Boundary Layer Height (BLH)

MSLP, WS100, dWS100, WV100 and dWV100 were natural inclusions given we are analysing the wind resource at heights relevant for wind energy generation. The other variables were targeted towards understanding the processes behind atmospheric circulation drivers, such as on surface energy balance, atmospheric energy conversions and possible effects of atmospheric condensation.

3.4.2 | Data fidelity

There was an emphasis on variables related to water vapour transport, not only because of the potential for CIAD, but also because this provides relatively high-fidelity data to corroborate the direction of tropospheric winds with that on the surface. Modelled outputs for water vapour transport are forced using satellite observations, and itself constitutes indirect measurement of tropospheric winds. But vegetation-surface wind interactions in ERA5 are modelled by extrapolating downwards from a fixed blending height and using grids with a characteristic roughness. As a result, the accumulated effects of sub-grid heterogeneity upon the trajectory of winds may not be accounted for, and in either case the surface winds are at least an extra step removed from direct measurement.[4]

3.4.3 | Net atmospheric condensation

We also derived a variable called NAC, which was meant to approximate the instantaneous balance between cloud formation and cloud evaporation at each hour of the day (see Appendix B.2 for derivation):

$$NAC\ [kgm^{-2}s^{-1}] = NSE\ [kgm^{-2}s^{-1}] - VIDMF\ [kgm^{-2}s^{-1}] \tag{3.1}$$

[4]Observations assimilated into the model for ERA5 do not include wind velocity inputs from weather stations because ERA5 is averaged over 0.25° grids which makes it incompatible with WMO conventions whereby 10 m winds are measured in open terrain. Instead, 100 m winds are extrapolated downwards from higher model levels under idealised assumptions, and the data assimilated for these higher model levels in turn derives from a mix of atmospheric soundings, aircraft and satellite irradiance data (part of which relies back on water vapour observations).

$$-\frac{d}{dt}(TCWV\ [kgm^{-2}])$$

where NSE is the net evaporation at the surface (i.e. not including atmosphere), VIDMF is the vertical integral of divergence of moisture flux, and TCWV is the total column water vapour (see descriptions in Table A.1).

3.4.3.1 | Atmospheric water budget equation

This is an accounting equation arising from the fact that Total Column Water Vapour (TCWV) can only change either due to net evaporation or condensation (on the surface and also in the atmosphere), or movement of water vapour from a neighbouring column (it is also theoretically possible for chemical reactions and sublimation/deposition to add or remove water vapour but this is assumed negligible). This equation is usually expressed in the atmospheric water vapour budget literature (Norris et al., 2020; Yan et al., 2020) as

$$\frac{d}{dt}(TCWV) = E - P - VIDMF \tag{3.2}$$

where E is surface evaporation and P is precipitation. But this equation is only valid for larger spatial and temporal scales.

At larger temporal scales, surface evaporation at the surface typically exceeds surface condensation, so NSE will be positive and is expressed as E (but note that this is using a more abstract notion of "surface evaporation" which absorbs the effect of intermittent surface condensation within the study period). To avoid confusion, we retain the use of the term "NSE" which makes explicit that surface condensation is absorbed within this variable.

Also, this literature equation is only valid if P = NAC. All atmospheric condensation eventually falls as precipitation so this equation is valid on larger spatial and temporal scales. But on smaller scales, there may be several hours of delay between condensation and precipitation, and winds may blow the condensed water droplets across several hundred km before precipitating. Since we are studying hourly diurnal profiles and using 30 km grids, we opt for NAC rather than P in this equation.

By similar reasoning, the use of Total Column Cloud Liquid Water (TCCLW) may give misleading results since prevailing winds may low cloud liquid water far from their point of formation. Thus, NAC is meant to provide a more accurate depiction of where cloud formation is occurring.

3.5 | Statistical summaries

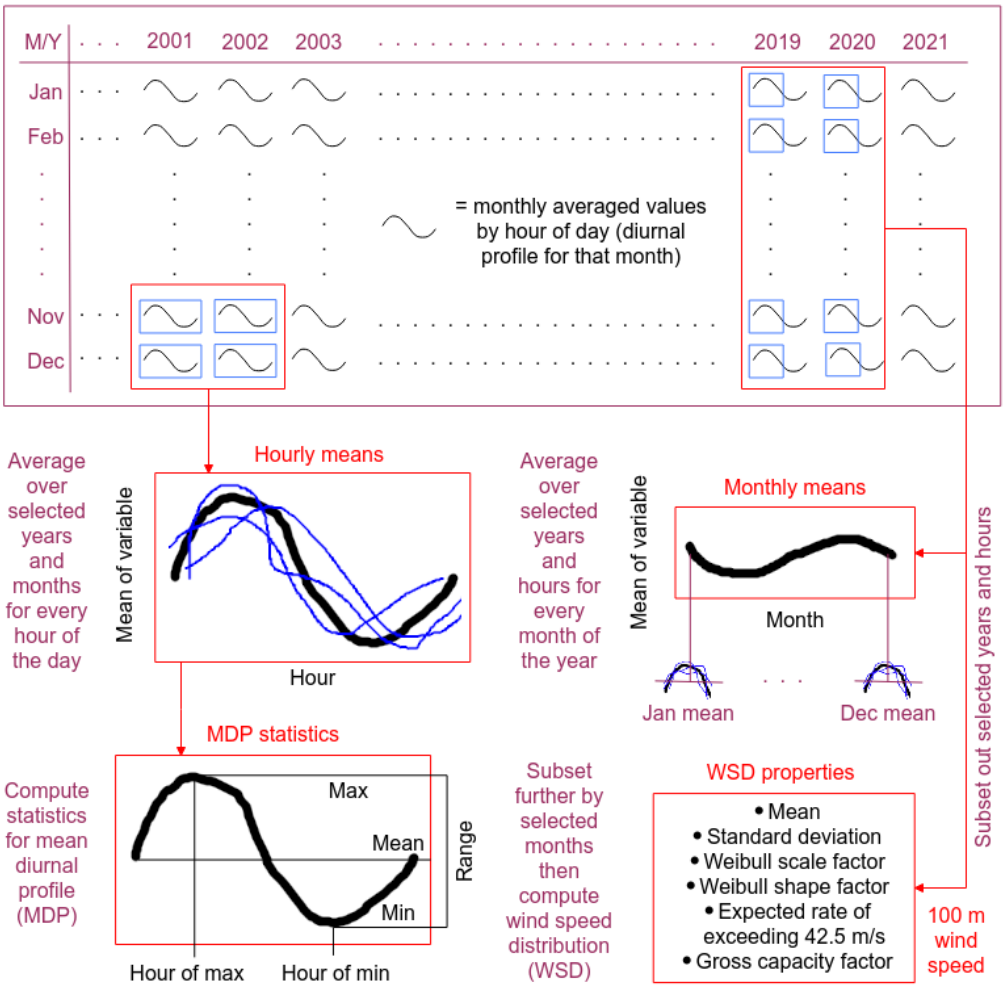

Figure 3.4: Flow chart illustrating how the statistical summaries for each variable were computed.

3.5.1 | Mean diurnal profile statistics

The "mean diurnal profile" (MDP) for a variable was defined by computing groupwise means for values by hour of day[5]. That is, the mean over all data values occurring on

[5]These averages were produced mostly by computing the mean of monthly averaged by hour of day data, which is roughly equivalent to the mean of all hourly data values. Vector variables were computed using hourly data values rather than monthly averaged by hour of day. Reasons for these choices are discussed in Appendix B.1.

the first hour of the day were computed, then the same was done for the second and all subsequent hours up until the 24th hour, and together these constitute the MDP. The MDP can be computed upon a month subset of the total data available over a period, so MDPs using values only from the wet or dry season can be obtained.

The hour of maximum, hour of minimum, maximum, minimum, mean and range for the MDP at each grid cell was then computed for visualisation[6]. Because, hour of maximum, hour of minimum, maximum, minimum and range for a vector is not well defined, we choose to apply generalised definitions for these statistics here so that: MDP hour of maximum and minimum refers to when the MDP magnitude of vector $\vec{v}$ is at a maximum and minimum respectively, MDP maximum and minimum refers to the MDP vector quantity of $\vec{v}$ at the hour of maximum and minimum, and MDP range refers to largest magnitude of all possible subtractions (corresponding to all possible hourly combinations) between the 24 MDP $\vec{v}$ values. Formally:

$$hour_{max}(\vec{v}) = i \text{ where } |\vec{v}_i| = max(\{|\vec{v}_k| : k \in \mathbb{Z} \cap [1, 24]\}) \tag{3.3}$$

$$hour_{min}(\vec{v}) = j \text{ where } |\vec{v}_j| = min(\{|\vec{v}_k| : k \in \mathbb{Z} \cap [1, 24]\}) \tag{3.4}$$

$$max(\vec{v}) = \vec{v}_i \text{ where } |\vec{v}_i| = max(\{|\vec{v}_k| : k \in \mathbb{Z} \cap [1, 24]\}) \tag{3.5}$$

$$min(\vec{v}) = \vec{v}_j \text{ where } |\vec{v}_j| = min(\{|\vec{v}_k| : k \in \mathbb{Z} \cap [1, 24]\}) \tag{3.6}$$

$$mean(\vec{v}) = \frac{1}{24} \sum_{k=1}^{24} \vec{v}_k \tag{3.7}$$

$$range(\vec{v}) = max(\{|\vec{v}_k - \vec{v}_l| : k, l \in \mathbb{Z} \cap [1, 24]\}) \tag{3.8}$$

3.5.2 | Hourly means

Hourly mean values are equivalent to the actual hourly values which constitute the MDP (as opposed to the MDP statistics).

3.5.3 | Monthly means

Monthly mean values are similar to hourly means except that it is computed separately for every month of the year (rather than a collection of months corresponding to wet or dry season), and instead can be computed over a subset of hours for comparison between day and night hours.

[6]Note here that for variables which can take on both positive and negative values, maximum refers to the most positive MDP value and minimum refers to the most negative MDP value.

3.5.4 | 100 m wind speed distribution

3.5.4.1 | Empirical Weibull fit

For the wind speed distribution, the sample mean and standard deviation was first obtained over the selected months and hours subset. An empirical Weibull fit was then performed in accordance with the methodology outlined by (Justus et al., 1977):

$$k = \left(\frac{\sigma}{\bar{V}}\right)^{-1.086} \tag{3.9}$$

$$c = \frac{\bar{V}}{\Gamma(1+1/k)} \tag{3.10}$$

where k is the Weibull shape parameter, c is the Weibull scale parameter, σ is the standard deviation of wind speed, $\bar{V}$ is the mean of wind speed, and $\Gamma(z) = \int_0^\infty t^{z-1}e^{-t}dt$ is the gamma function.

3.5.4.2 | Expected rate of exceedance

Expected Rate of 100 m Wind Speed Exceeding 42.5 m/s (EROE100) was then calculated using the tail from the empirical Weibull fit (as opposed to rate of exceedance directly calculated from the hourly data points) since the underlying probability distribution better captures risks which by chance may not have manifested in the data points. 42.5 m/s was chosen as this is the typical wind speed which wind turbines can last 10 mins in before failure (Chen et al., 2015, 2016; GE Energy, 2018).

Experimental results by Lee et al. (2012) and a review of methods by Palutikof et al. (1999) suggest that the use of a Gumbel distribution for wind gust data would have been more accurate for assessing extreme wind speeds, but this analysis was not pursued since the ERA5 dataset does not contain a field for wind gusts at 100 m, and because interpretation of Gumbel parameters are less intuitive.

3.5.4.3 | Typical gross capacity factor at 100 m

As opposed to EROE100, Typical Gross Capacity Factor for 100 m Turbine (TGCF100) was directly calculated from the hourly data points. This was deemed valid because tail wind speeds have an insignificant effect on TGCF100 as all wind speeds above the cutoff represent zero power anyway. TGCF100 was calculated by first averaging the power curves of three turbines by common manufacturers to obtain a typical power curve, then using this to calculate the average power generated over the period as a fraction of the nameplate power rating.[7] The Vestas V100/2600, Goldwind GW100/2500 and GE Energy 2.5-100 were chosen for this calculation since these were turbines at 100 m hub height with comparable rotor diameter (100 m), power rating (2500 kW), and cut-in and cut-off wind speeds.[8] Data for these turbine power curves were obtained from The Wind Power (2022c,d,g).

3.6 | Main datasets

3.6.1 | ERA5 reanalysis data

The ERA5 dataset is provided by European Centre for Medium-Range Weather Forecasts (ECMWF) and is widely used in atmospheric studies and is considered one of the more accurate reanalysis datasets for surface wind speeds (Doddy Clarke et al., 2021; Fan et al., 2021; Hersbach et al., 2019; Ramon et al., 2019; Torralba et al., 2017). We required reanalysis data to visualise spatially complete changes over an entire region (as opposed to in-situ measurements which are usually sparse). Of the available reanalysis datasets, ERA5 was chosen for its superior spatial (0.25°) and temporal (hourly) resolution, closest agreement with observed wind speeds, and relatively accurate capture of interannual variability (Doddy Clarke et al., 2021; Fan et al., 2021; Ramon et al., 2019; Torralba et al., 2017).

The superior resolution was particularly important since this project sought to investigate diurnal variations (so an hourly time resolution was desirable), and the methodology was designed to interrogate the interfaces between different types of land cover (coarser spatial resolutions may have averaged out interesting effects).

3.6.2 | GLASS satellite-derived data

The GLASS product suite includes spatially complete modelled datasets for LAI and FAPAR with temporal resolution of 8 days (constrained by satellite overpasses) and spatial resolutions down to 250 m. This dataset is widely used for analysing vegetation cover and land surface effects (Fang et al., 2019; Liang et al., 2021), and was selected because it was found to be the most consistent with Google Earth historical satellite imagery. The datasets with spatial resolution of 0.05° were selected as this provided

[7] Note that this is mathematically equivalent to computing the gross capacity factor for each of the three turbines then finding the average (see Appendix B.1).

[8] The Vestas power curve was scaled by a factor of 25/26 to make it comparable with the other turbines.

sufficient detail to distinguish land cover types at sharp interfaces without consuming too much computer storage and memory.

Other datasets such as the ERA5 LAI variables (Hersbach et al., 2019), Copernicus Climate Change Service (C3S) LAI V3 (C3S, 2022), NOAA Climate Data Record (CDR) LAI V5 (Vermote, 2022a) and NOAA CDR Normalised Difference Vegetation Index (NDVI) V5 (Vermote, 2022b) were considered, but these were found to often have missing values, data processing artefacts, discrepancy against Google Earth historical satellite imagery, or other significant data deficiencies (not shown).

3.7 | Software

All data manipulations were performed using Python 3.9.12. Statistical summaries were computed primarily using the `xarray` (Hoyer and Hamman, 2017) and `dask` (Dask Development Team, 2016) libraries, while visualisations relied on the `matplotlib` (Hunter, 2007) and `cartopy` (Met Office, 2010 - 2015) libraries.

A series of purpose-designed Python programs were created in the course of this project. These programs include a `data_download.py` script to automatically download all raw data inputs used in this project, a `calc_funcs.py` script which handles all the data processing, and a `plot_funcs.py` script which handles all the visualisations.

All programs created in the course of this project are freely available, and all results were designed to be reproducible from scratch (see Appendix C). With trivial edits, these programs can take an arbitrary variable from the ERA5 dataset, then compute and visualise the statistical summaries outlined in Section 3.5. These programs have broader applicability beyond this project as it can be used to study diurnal and seasonal variations in general, as well as how these variations differ between periods.

Due to the memory requirements necessary to process the large datasets, this research includes computations using the computational cluster Katana supported by Research Technology Services at University of New South Wales (UNSW) Sydney.

4

Results and Discussion of Findings

4.1 | How to interpret comparison plots

- The comparison plots below each consist of three columns. The leftmost column plots the spatial distribution for a statistical summary over the first study period in the comparison. The middle column does the same for the second study period in the comparison. And the rightmost column plots the differences in the statistical summaries between the two periods (second period minus first period).

- The colourbars have been standardised to allow fair comparison between periods, months and hours.

- Details on which period, month and hour being plotted are expressed in the title for each of the subplots.

- Where spatiotemporal correlations in the left or middle columns hold between an ERA5 statistic and MLAI, this is suggestive that the vegetation cover *may* be responsible for the observed variations in the ERA5 statistic.

- Where spatiotemporal correlations hold between the right column of an ERA5 statistic and the left or middle columns for MLAI, this leaves open the question of what is causing the observed variations in the ERA5 statistic, but suggests that vegetation cover *may* be responsible for modulating these variations.

- Where spatiotemporal correlations hold between the right columns of an ERA5 statistic and MLAI, this is suggestive that the variations in vegetation cover *may* be responsible for the variations in the ERA5 statistic.

4.2 | Orography

The orographic variables (LSE and SSGO) for the WA focus region are displayed in Figure 4.1 for reference.

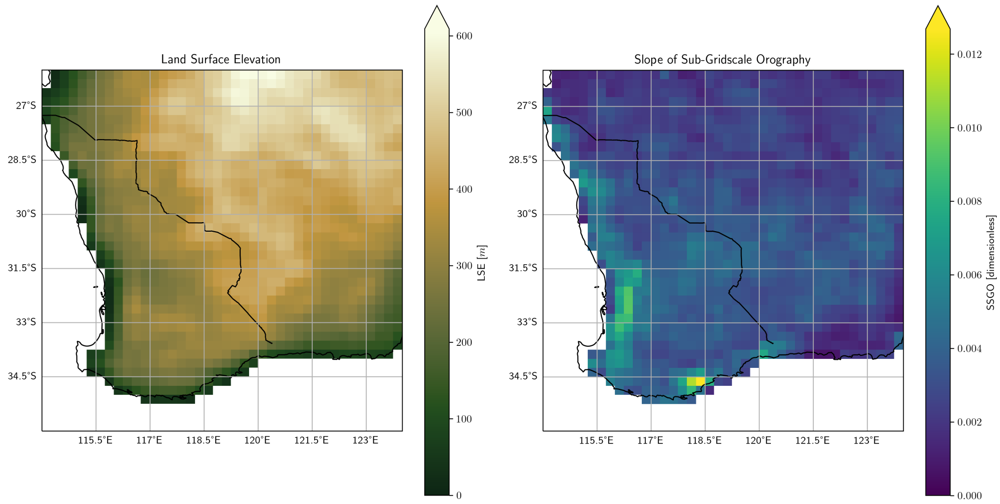

Figure 4.1: Land Surface Elevation (LSE) (left) and Slope of Sub-Gridscale Orography (SSGO) (right) for the WA focus region.

4.3 | Diurnal comparison for January mean

4.3.1 | VIEC delineation along fence

VIEC mean values computed over January displayed a marked distinction across the State Boundary Fence of Western Australia (SBFWA), with more strongly negative values on the native side of the fence during both the day and night (see Figure 4.2).[1] During daytime, this also marks the distinction between positive VIEC values on the agricultural side and negative values on the native side. Negative VIEC values indicate a greater prevalence for upwards air movement (kinetic energy converted into gravitational potential energy), while positive values indicate the opposite.[2]

[1]The following results are also observed to varying degrees for the months of February, October, November and December, but we present January because this month displays these trends most distinctly.

[2]There are better variables than VIEC in the ERA5 dataset to analyse upwards and downwards air movement since VIEC lumps internal and gravitational potential energy together, but these other variables were not included in the original analysis and time constraints in this project did not allow for modification of the methodology. See Section 5.2.1.

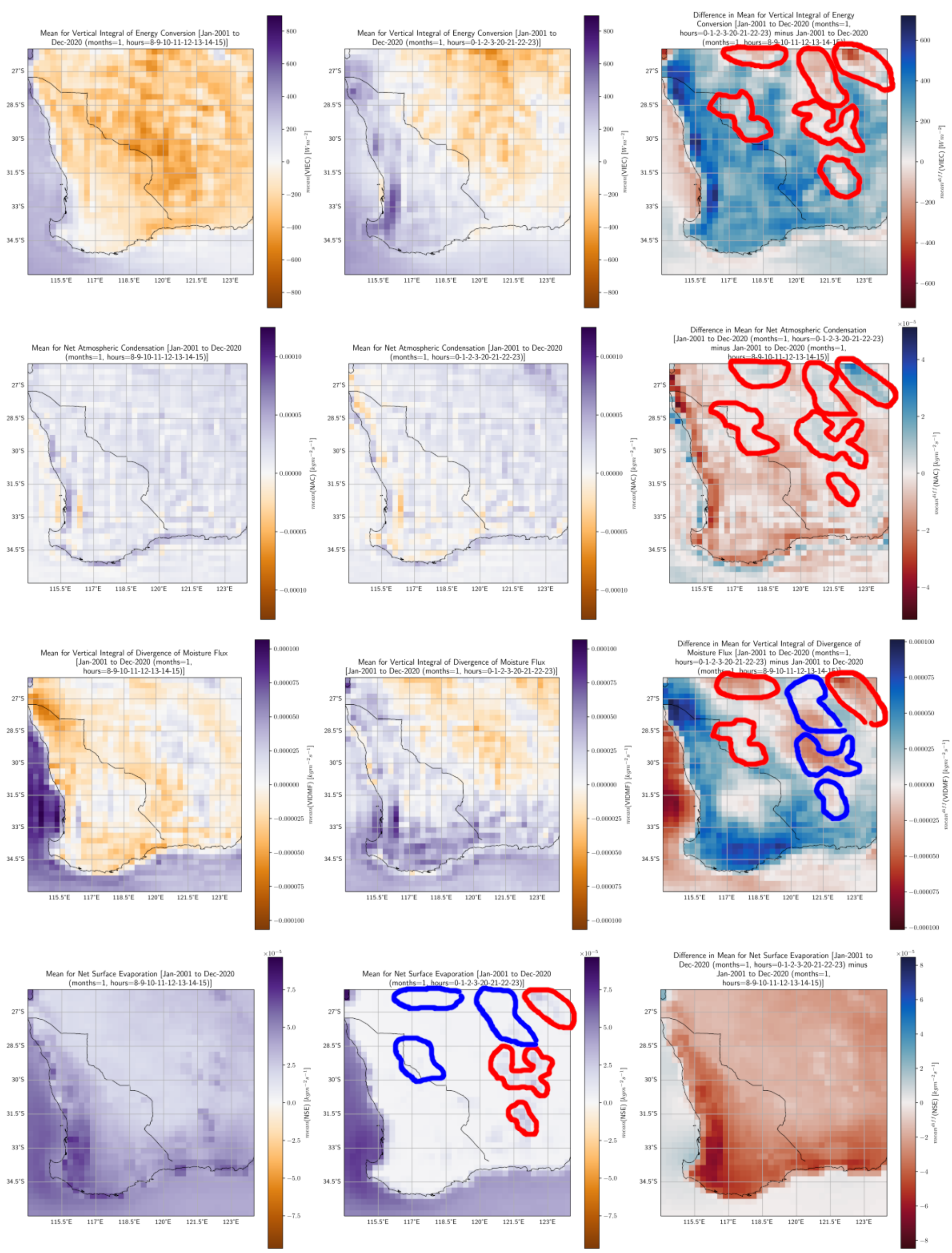

Figure 4.2: January mean daytime and nighttime values for VIEC, NAC, VIDMF and NSE. Red markings indicate selected areas which are distinct from background trends. Blue markings indicate areas where such a distinction did not exist, but did exist for VIEC.

The large-scale patterns observed for VIEC^{diff} in arid WA are mostly a reflection of warmer temperatures during daytime, and warmer temperatures on the native side due to thermal retention and lower albedo of native vegetation compared to bare agricultural soil in January. Evidence for this is a remarkable large-scale spatial correlation between T2, MSLP and VIEC for all months of the year (not shown, but January results are displayed in Figure 4.3). This suggests that the large-scale tendencies for vertical air mass movements in inland areas[3] are driven by surface heating, in accordance with standard theory.

4.3.2 | Localised anomalies

However, there are local-scale features which act contrary to this background trend. These are highlighted with red markings in Figure 4.2.[4] In these areas, VIEC becomes increasingly negative (air movements are increasingly upwards directed) from daytime to nighttime despite the decrease in temperature, and there did not appear to be any localised anomalies in T2 which could explain this (see Figure 4.3).

Interestingly, these VIEC^{diff} anomalies correspond to localised areas of positive NAC^{diff} (see Figure 4.2). Given the suspected role of CIAD, we turn to the question of whether this correlation primarily reflects a chance convergence of winds manifesting stronger upwards air movements which was then conducive towards cloud formation, or whether the actual condensation itself was responsible for the strengthening vertical motions.

4.3.3 | Contribution from lake evaporation

At least a few of these anomalies can be attributed to evaporation from ephemeral lakes[5], which calls into question how relevant chance wind convergence would be on top of this. The lakes display a relatively low magnitude of evaporation decrease going from daytime to nighttime temperatures. This can be seen in the difference plot (right column) for NSE in Figure 4.2 but for visual clarity, these lakes were marked in red for the nighttime plot (middle column) instead.

Furthermore, given the low magnitude of NSE over these lakes relative to background trends, we would have expected increased water vapour *divergence* via diffusion (positive VIDMF^{diff}). But instead, what we observe is that these lakes correspond

[3]Coastal effects are treated separately in Section 4.4.

[4]The use of coloured markings with a thick outline somewhat distorts perception of these features. For an unmarked version of the figure, see Appendix A.1.

[5]Although ephemeral, use of Google Earth satellite images confirms that these lakes contained water for all December months within the study period (and the water is presumably still there by January).

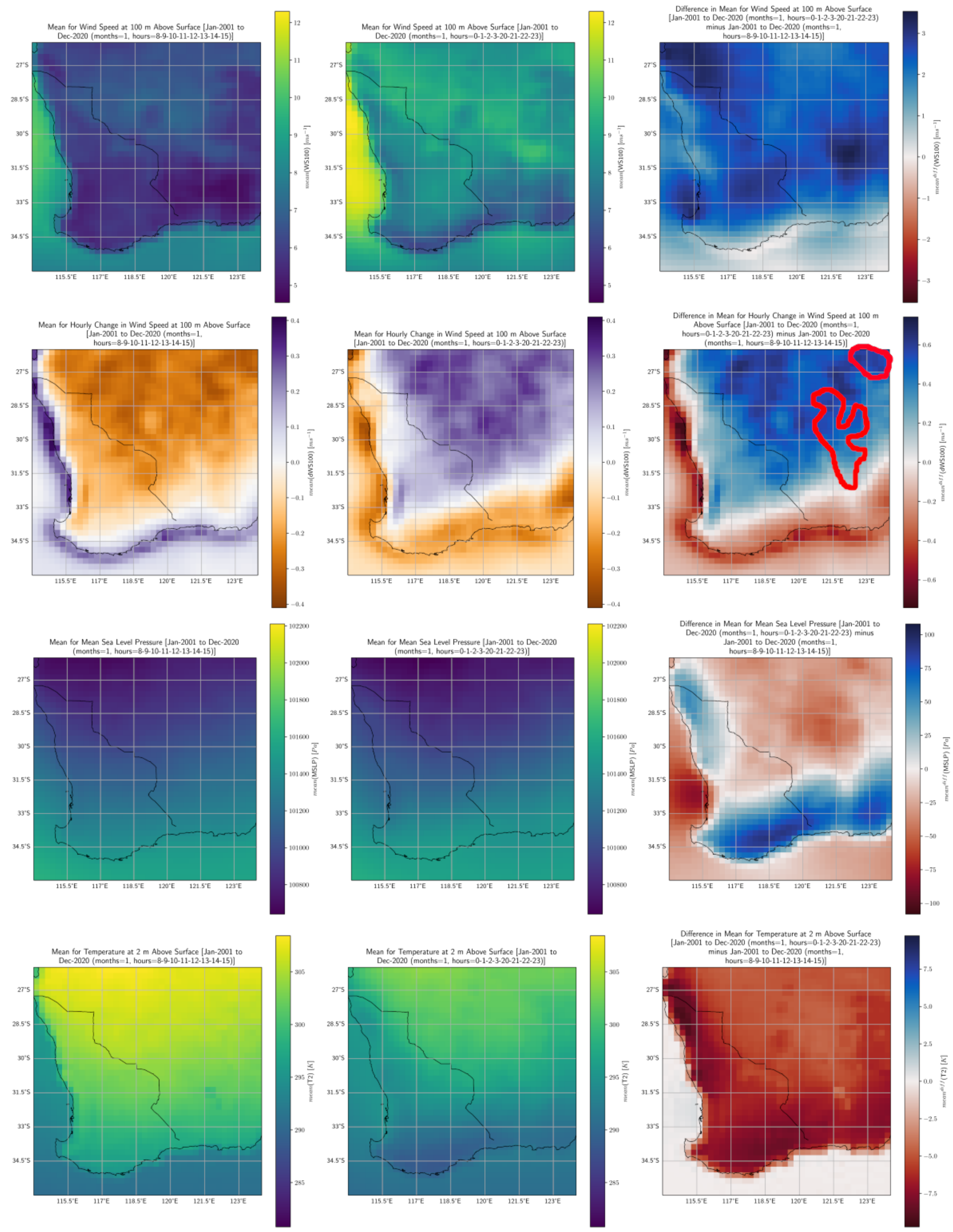

Figure 4.3: January mean daytime and nighttime values for WS100, dWS100, MSLP and T2. Red markings indicate selected areas for dWS100 which are distinct from background trends but which deviate from orographic spatial patterns.

to areas of *negative* VIDMF^{diff} (indicating increased water vapour *convergence*). Given it is unlikely for a chance convergence of winds to coincidentally conform to the extents of the lakes, this flags the possibility of CIAD as to our knowledge there has been no other proposed mechanism which would explain this anomaly. That is, continued evaporation combined with cooler temperatures during night time leads to increased atmospheric condensation, and under this may form a localised area of low pressure which advects air and moisture towards itself for sustenance.

4.3.4 | Implications for surface wind resource

In studying implications for wind energy generation, we turn towards 100 m wind speed (WS100) as well as the *hourly change* in 100 m wind speed (dWS100). The latter allows us to analyse effects upon WS100 which may be slight and difficult to visually identify from a plot of WS100 itself since the signal is dominated by synoptic effects.

4.3.4.1 | WS100 higher on native side of fence

Despite lower roughness on the agricultural side of the fence in January (when there is no crop and often bare soil), WS100 is higher on the native side of the fence and shows some signs of being delineated along the fence itself. This is likely a reflection of surface air pressure differences arising from temperature differences (see Figure 4.3 left and middle columns; note how the fence delineations for WS100, MSLP and T2 do not hold along the southern part of the region from 34.5°S to 31.5°S). Given that results for T2 shows a clear demarcation along the fence in Figure 4.3, it then follows that wind speed variations beyond the effect of surface roughness can in part be attributed to the type of vegetation cover. Future changes to vegetation cover (such as eastward agricultural expansion, or change in crops being grown) which cause a decrease in temperatures may possibly reduce wind speeds (and the converse for increases in temperature).

4.3.4.2 | Anomaly for diurnal difference in MSLP on native side of fence

Decrease in pressure despite convergence of mass and decrease in temperature Although the spatial pattern observed for MSLP^{diff} is similar to that of T2^{diff} in Figure 4.3, a large area of the focus region (mostly on the native side of the fence) sees a *decrease* in surface pressure going from day to night despite a decrease in temperature. So mass flux directed away from the surface of this area (i.e. decreasing surface pressure) does not appear to be caused by surface temperature changes inducing *upwards* air movement. Nor does it appear to be caused by *outwards* (horizontal) mass transport given that much of this area displays increased moisture *convergence* (negative VIDMF^{diff}) in Figure 4.2 (in turn implicating increasing *convergence* of winds and air mass in general).

Possible explanations The remaining explanations are either that there is some climate feature in the upper atmosphere or outside of this focus region or which interacts with the surface of this focus region to produce a reduction of pressure towards nighttime, or that the reduction in surface pressure actually arises from a drop in air density as gaseous water condenses out as liquid.

The latter appears to only be mildly supported by the NAC results in Figure 4.2. An increase of condensation only occurs in certain parts of the area where there is negative MSLP^{diff}, and these parts do correlate with especially negative MSLP^{diff} values, but it is not clear whether these distributed localisations of condensation can produce the area-scale effect seen for MSLP^{diff}. However, it should be noted that much of the patchiness observed in NAC could possibly result from the fact that NAC is a hybrid value derived a mixture of instantaneous and accumulated ERA5 variables (see Appendix B.2).

Possible implications for surface wind If it is indeed the case that atmospheric condensation is responsible for the surface pressure drop and hence increase in wind speeds, then this is yet another mechanism by which the surface wind resource depends on land cover, given results by (Lyons, 2002; Ray et al., 2003) which clearly demonstrates that land cover modulates cloud formation preferences (also see Section 4.5.4).

4.3.4.3 | Anomalies in dWS100

dWS100 correlated with LSE, VIEC and NAC The spatial pattern observed for dWS100 corresponds mostly to the LSE displayed in Figure 4.1. Higher elevations are correlated with more negative dWS100 values during the daytime, more positive values during nighttime, and hence a greater magnitude of increase from day to night. Selected areas which display the opposite trends are highlighted with red markings in Figure 4.3.[6]

Interestingly, these areas correspond with the lakes identified earlier, and actually show an especially positive value for $\mathrm{dWS100}^{diff}$ (strengthening of winds). A more negative VIEC^{diff} (less conversion of internal and gravitational potential energy to kinetic) in these areas should imply a more negative $\mathrm{dWS100}^{diff}$ (weakening of winds) all other things equal, so it is not clear what is causing this anomaly. One possibility is that convection associated with increased NAC (cloud formation) in these areas at nighttime

[6]For an undistorted view, see the figure without markings in Appendix A.1.

lead to favourable energy exchanges between the boundary layer and free atmosphere, and a reversal of this effect in the daytime manifests as a greater decrease in wind speed.

Possible implications for surface wind If it can be shown that positive NAC^{diff} consistently correlates with especially positive dWS100^{diff}, then land cover is again implicated through land cover modulation of cloud formation, with the effect that native vegetation induces a greater ramp rate in wind speeds in summer (when clouds preferentially form over the native side of the fence).

4.4 | Seasonal comparison for 1400 mean

4.4.1 | Seasonal difference in MLAI

Figure 4.4 displays a comparison for the Mean Leaf Area Index between the months of JJA and DJF. Native vegetation on the east of the SBFWA show negligible differences. There is a significant loss in MLAI towards the DJF months as the wheat and barley crops which were grown from May to November are harvested in November (Lyons et al., 1996). The extents of the MLAI loss correspond well with the Wheat Belt region of Western Australia (see Figure 3.3). Slight (relative to JJA base value) greening appears to occur in the coastal Jarrah forests through the spring and summer months.

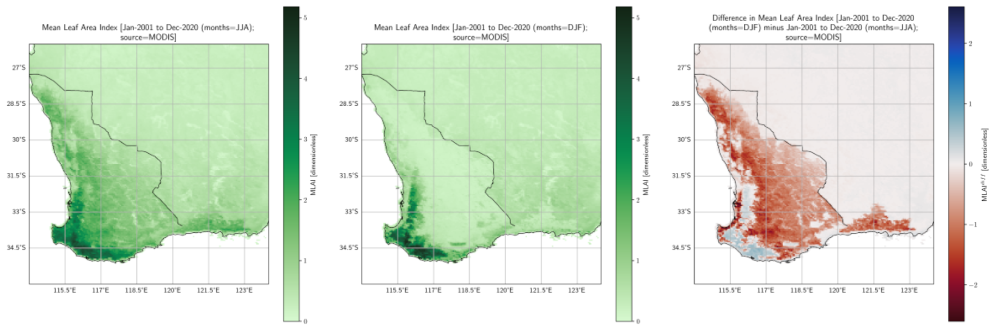

Figure 4.4: MLAI computed over JJA and DJF (left and middle), as well as the difference in these values between the two seasons (right).

4.4.2 | Correlation between VIEC and NAC

VIEC mean values computed over 1400 LT display a remarkable spatial correlation with that of NAC. This is especially apparent near the coast for JJA means, and in general for the difference plots between JJA and DJF (leftmost and rightmost columns in Figure 4.5

respectively). More positive NAC and NAC^{diff} values are correlated with more negative VIEC and VIEC ^{diff} values respectively. T2^{diff} (see Figure 4.6) shows a relatively uniform pattern and is consistent with the large-scale trend in VIEC ^{diff} (warmer air tends to rise more), but it does not capture any of the smaller-scale trends that NAC^{diff} does.

We choose to display results for 1400 LT here because results for this hour are most distinct, but the following is actually more or less observed for all hours of the day in the hourly means analysis and all months of the year in the monthly means analysis (not shown):

- For both JJA and DJF results, we observe that on the native side of the fence, most areas of negative VIDMF^{diff} (increased moisture *convergence*) correlate with areas of positive NSE^{diff} (increased evaporation) but positive NAC, contrary to what is expected from diffusion but consistent with CIAD.

- None of the variables from which NAC is derived display similar local-scale spatial variations to VIEC across most of the focus region (VIDMF and NSE for 1400 are displayed in Figure 4.5, TCWV not shown at all). Only NAC itself is similar to VIEC.[7]

- The concentrated band of negative VIEC and positive NAC means along the southwestern coastline for JJA is present regardless of whether the band is upwind or downwind of the coastline, and whether the temperature gradients are producing a land or sea breeze (see T2 and dWV100 in Figure 4.6 for 1400 LT results).

The final point indicates that coastal orography and differential heating are unlikely to be responsible for the concentrated band along the southwestern coastline. And these points together conspire to heavily implicate the possibility of CIAD.

4.4.3 | The role of coastal geography

One way in which negative VIEC (rising air) could theoretically be concentrated along the coastline is if low-lying oceanic winds experience a sudden change in surface elevation and are deflected upwards from coastal cliffs and urban structures. But this does not explain why the observed bands in Figure 4.5 extends out into the oceans, nor why the band is observed on the southernmost part of this region (around 35°S) where winds are blowing from relatively high terrestrial ground to relatively low ocean surface (see

[7]Exceptions occur for hours 0500-0700 LT and 1700-1900 LT due to data artefacts in ERA5, but this should not affect the conclusions. See Appendix A.4 for discussion.

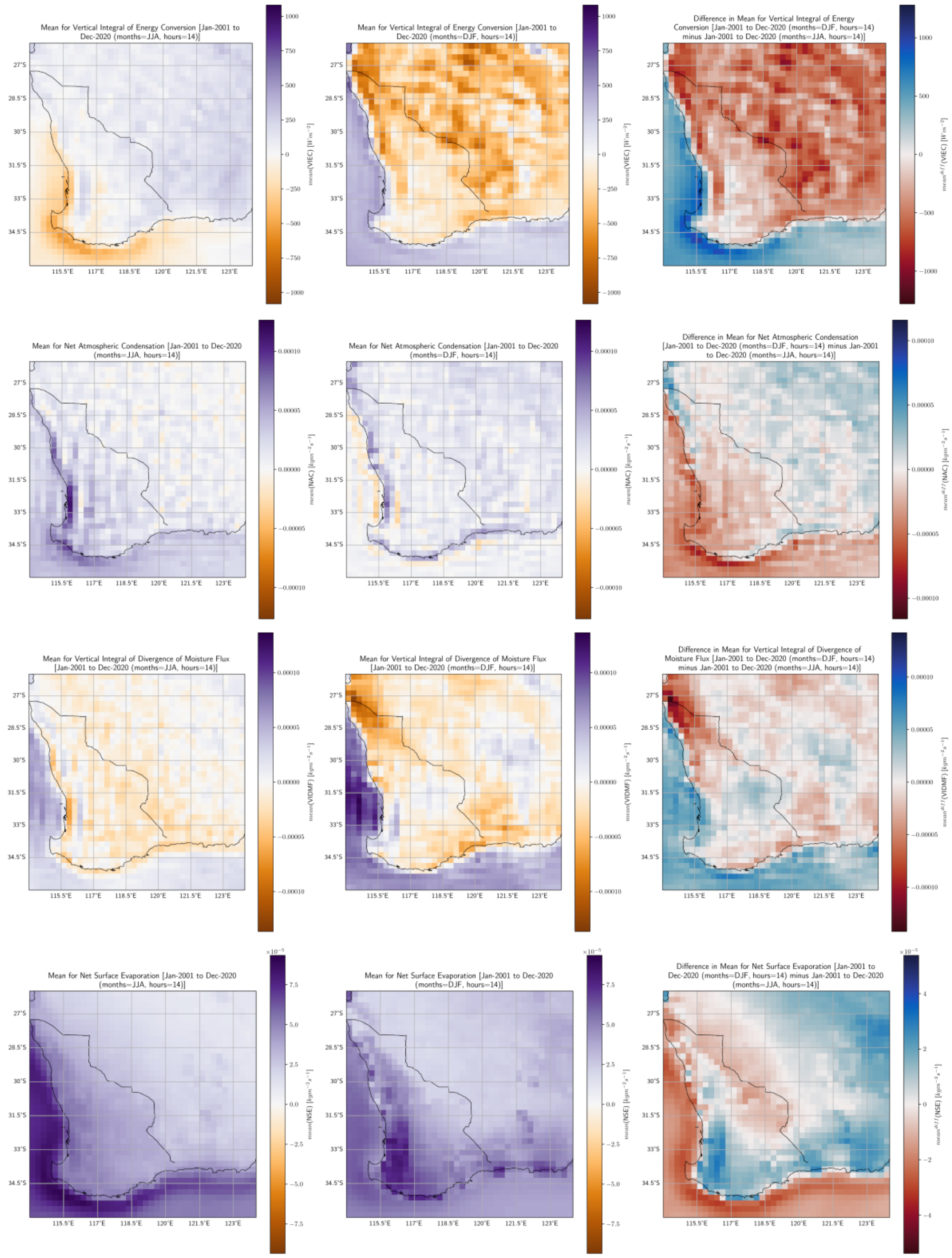

Figure 4.5: 1400 mean JJA and DJF values for VIEC, NAC, VIDMF and NSE.

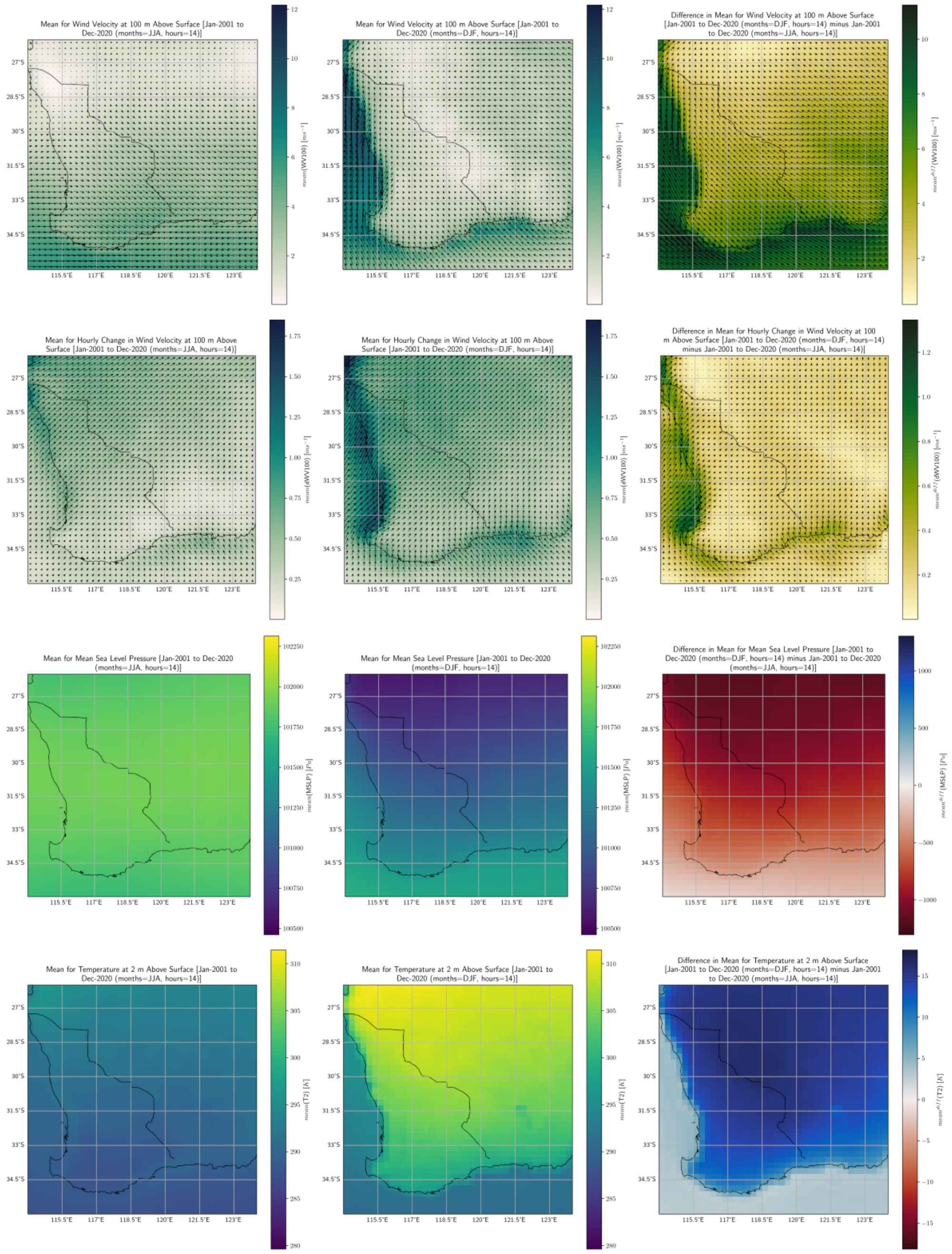

Figure 4.6: 1400 mean JJA and DJF values for WV100, dWV100, MSLP and T2.

WV100 in Figure 4.6). Furthermore, much stronger winds are blowing onshore during the DJF months yet this coastal band is not observed for these months (compare VIEC in Figure 4.5 with WV100 in Figure 4.6). So it seems extremely unlikely that coastal orography is the cause.

4.4.4 | The role of coastal differential heating

Another way in which negative VIEC (rising air) could theoretically be concentrated along the coastline is if a localised pressure gradient (arising from a temperature gradient) along the coastline adverse to the wind direction caused a bunching up of mass such that air had to be directed upwards. But results indicate the presence of this band regardless of the strength and direction of the coastline temperature gradient relative to prevailing winds. For the case of 1400 LT, Figure 4.6 displays a negligible coastal pressure gradient, temperature gradient and magnitude of dWV100 in JJA, yet the band exists for these months but not DJF where these parameters are much more significant. So it also seems highly unlikely that differential heating is the cause.

Although Figure 4.6 displays a negligible coastal gradient in *air* temperature for JJA at 1400 LT, the Leeuwin (Ocean) Current during these months actually brings about a significant increase in Sea Surface Temperature (SST) for the continental shelf waters (Berthot et al., 1997). This can be seen in Figure 4.5, where offshore evaporation is significantly higher in JJA than DJF despite lower solar irradiance.

4.4.5 | The role of coastal condensation

4.4.5.1 | Atmospheric condensation as cause for convective initiation

Summary of conclusions from seasonal comparison thus far In summary, the coastal concentration of negative VIEC (upwards air movements) occurs in continental shelf waters where *air* temperature is comparable to that on land, but where *water* temperatures are higher than that of air due to the winter presence of the Leeuwin Current. There is additional atmospheric moisture from the warmer waters which contributes to air buoyancy but analysis of Convective Available Potential Energy (CAPE) values reveals no coastal concentration whatsoever (not shown).[8] So having ruled out mechanical deflection of winds from coastal geography, localised pressurisation from coastal differential heating, higher offshore *air* temperatures leading to upwards thermal ex-

[8]This is in spite of the fact that CAPE in the ERA5 dataset is known to occasionally give unrealistically high values (ECMWF, 2022).

pansion, and additional air buoyancy from increased atmospheric moisture, CIAD is to our knowledge the only proposed mechanism consistent with the results.

Direction of causation In the CIAD picture, additional winter atmospheric moisture from the Leeuwin Current is conducive towards coastal cloud formation, and it is this atmospheric condensation (positive NAC) which initiates convection and subsequent uplift of air (negative VIEC). That is, the direction of causation for *initiation* of local circulations is from condensation to convection. In the ensuing circulation, the direction of causation is ill-defined as there is a positive feedback loop between the two. The circulation persists until the available moisture (latent energy) is unable to sustain the air motions.

4.4.5.2 | Interactions with temperature gradients and surface energy fluxes

On top of this, there is the effect of coastal temperature gradients in determining the spatial distribution of atmospheric moisture available for condensation, and the effect of SSHF inland in determining whether there is sufficient convective mixing for the BLH to penetrate the Lifted Condensation Level (LCL) for condensation to occur.

Consistency with JJA results Weaker winds from temperature gradients in JJA compared to DJF means the buildup of oceanic moisture along the coasts has a high condensation rate relative to moisture convergence flux to inland areas. For the 1400 LT case, this is reflected in JJA by low WV100 magnitude, low dWV100 magnitude and weak coastal T2 contrast in Figure 4.6, as well as a less positive VIDMF offshore (west of the coastline) despite higher NSE in Figure 4.5. The result is that VIEC displays a similar band to NAC along the coast. This is also supported by the fact that the negative VIEC band is absent from around 29°S to 27°S, which coincides with where dWV100 is especially strong.

DJF results and flux of moisture convergence towards fence On the other hand, stronger winds from temperature gradients in DJF imply the converse. The ratio of inland moisture flux transport to coastal condensation rate is relatively high (in part due to lower coastal moisture from absence of Leeuwin Current), so no coastal band of negative VIEC is observed. Instead, there is increased condensation (relative to JJA) on the native side of the fence, possibly due to higher SSHF, and this is where negative VIEC concentrates instead. This would seem to be supported by VIDMF results which show for DJF how moisture convergence (negative VIDMF) moves inland ahead of moisture divergence (positive VIDMF) as the day progresses, eventually reaching a point where convergence is concentrated on the native side of the fence (see Figure 4.7).

4.4.6 | Implications for surface wind resource

4.4.6.1 | Effect on coastal breezes

The replacement of native vegetation with annual crops, where there is irrigation in winter, bare cover after harvesting in summer, and lower albedo year round, has likely led to the lower surface temperatures observed on the western side of the SBFWA year round. These lower temperatures were observed in the monthly means analysis for T2 (not shown) but can also be seen in Figure 4.6 for the case of 1400 LT in DJF. Assuming that native vegetation cover which existed in the southwest region prior to agricultural clearing had similar temperatures to that currently observed on the native side of the fence, diurnal monthly means analysis (not shown) suggests that the agricultural clearing has led to:

- For daytime during warmer months (Oct to Mar): a weakening of the sea breeze
- For nighttime during warmer months (Oct to Mar): a slight strengthening of the land breeze, with possibly a reversal from slight sea breeze to slight land breeze
- For daytime during cooler months (Apr to Sep): a slight strengthening of the land breeze, with possibly a reversal from slight sea breeze to slight land breeze
- For nighttime during cooler months (Apr to Sep): a very slight strengthening of the land breeze

4.4.6.2 | Inland drying and coastal flooding

In all cases this points towards a loss in inland atmospheric moisture, and may partly explain the well documented loss of rainfall and water vapour in the southwest region (Gordon et al., 2003; Junkermann et al., 2009; Narisma and Pitman, 2003; Pitman et al., 2004). To the extent that atmospheric moisture is oceanic in origin (as opposed to from plant transpiration), as is often the case given the coastal location and dry climate of this region, a corollary to reduced inland moisture flux is an increased flood risk from the coastal buildup of moisture.

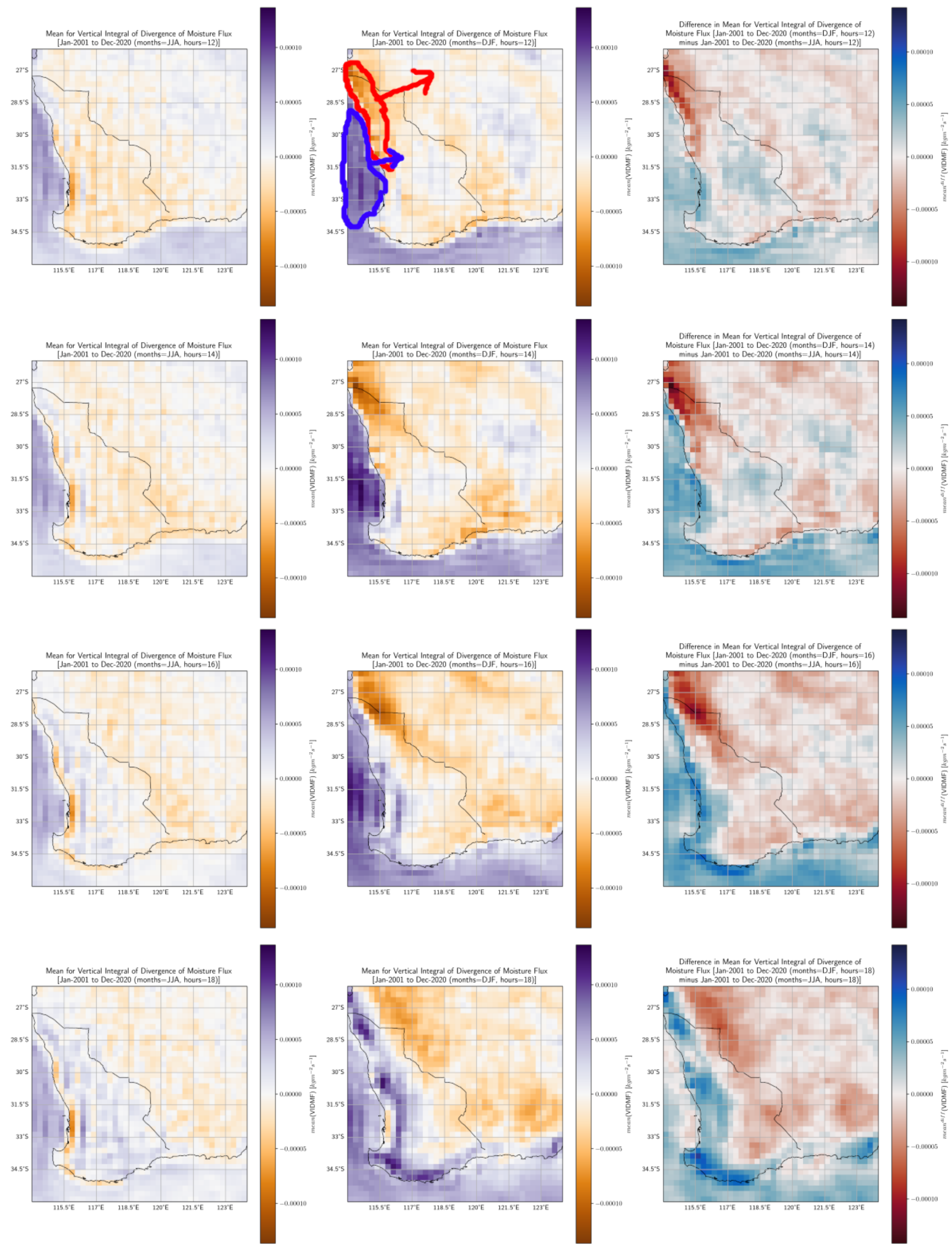

Figure 4.7: 1200-1800 mean JJA and DJF values for VIDMF. Red and blue markings illustrate how moisture convergence and divergence respectively is initially concentrated near the coastline then moves inland as the day progresses, eventually reaching a point where convergence is concentrated on the native side of the fence.

4.4.6.3 | Possible exacerbation under CIAD

The available evidence appears to support the CIAD framework moreso than it does the notion that cloud formation is a passive byproduct of moist air masses rising (whether due to surface heating, orography or chance convergence of winds). This is unless there is some systematic error in the ERA5 dataset which we are not aware of and which just so happens to produce misleading results.

Assuming this isn't the case and also assuming that the CIAD framework is valid, then beyond ocean-land temperature differences from native vegetation clearing there would have been an additional contribution from reduced atmospheric condensation. That is, the drop in air pressure which accompanies atmospheric condensation becomes less prevalent, so even less air and moisture is advected inland. And the result is further exacerbation to inland rainfall loss and coastal flood risk.

4.4.6.4 | How this affects wind energy operation

Operational revenue and risk The strengthening and weakening of breezes has a direct impact on how much energy coastal wind farms are able to generate. Coastal breeze changes appear to only be slight except in the case of daytime during warmer months (Oct to Mar). These months also happen to be when energy demand from air conditioning is at its highest so all other things equal, this translates to a loss in wind generation revenue compared to if current agricultural cover was instead native vegetation cover. This is especially so since a weakening of the sea breeze also means less cool relief for the urban centre of Perth.

Coastal flooding also constitutes a tail risk for wind energy operation. There is obvious damage that can be done to both turbine structures as well as accompanying electrical infrastructure. Despite the context of continued climate change, such increases in risk might not yet be internalised within project costs. Failure to properly capture these risks may produce losses which deter future investment.

Future changes in land cover There is further risk embodied within uncertainty of what future land cover will be. Afforestation efforts are a real possibility given increasing environmental consciousness by the public. Changing geopolitical-economic conditions, climate and public favour may also give way to the growing of different crops (including summer crops) in this region. Continued agricultural expansion is another possibility. In all these cases, it matters what species of trees or crops are being grown and how, as this determines the subsequent surface energy fluxes, temperature, and roughness.

Large-scale coastal afforestation using eucalypts with low albedo and high SSHF, for example, are likely to strengthen the summer daytime sea breeze due to higher coastal temperatures (but it is unclear how sustainable this will be without the appropriate matter flux feedbacks (e.g. water, nutrients) granted by appropriate biodiversity). The large-scale adoption of summer crops with irrigation on the other hand, is likely to weaken the summer daytime sea breeze due to lower inland temperatures.

Possible changes in turbulence and condensation hotspots If CIAD is valid, then the previous comments apply even more so. This also implies that land cover determines the concentration and spatial distribution of turbulence from rising air masses (negative VIEC) via atmospheric condensation (positive NAC). This in turn can introduce fatigue to turbine components and complex wake effects which inhibit energy generation. On top of this, future mining activity may change condensation hotspots and hence circulation patterns via changes in lake geochemistry affecting Cloud Condensation Nuclei (CCN) production (Junkermann et al., 2009).

4.5 | Seasonal comparison for MDP statistics

4.5.1 | Likely influence of agriculture on VIKE

4.5.1.1 | Delineation along fence

Figure A.5 displays a delineation along the SBFWA for $range$(VIKE) and $hour_{max}$(VIKE) in JJA. None of the other MDP statistics for VIKE displayed remarkable results, and this spatial pattern may just be a coincidence. But the JJA value for $range$(VIEC) shows not only a delineation along the fence, but also along the edges of the coastal forests (compare with Figure 4.4). However, this can also be interpreted as a coastal effect extending inland which is unrelated to the forests (it is difficult to distinguish between these since the forest cover follows the shape of the coastline).

4.5.1.2 | Description of trends

The JJA values for VIKE on the agricultural side show a smaller range, and an hour of maximum which is around two hours earlier. This is around the time of the morning boundary layer transition. VIKE includes upper atmospheric air, so may be related to the surface via the boundary layer-free atmosphere interface. However, it is still unclear whether this is relevant and what is causing the observed spatial pattern. It is

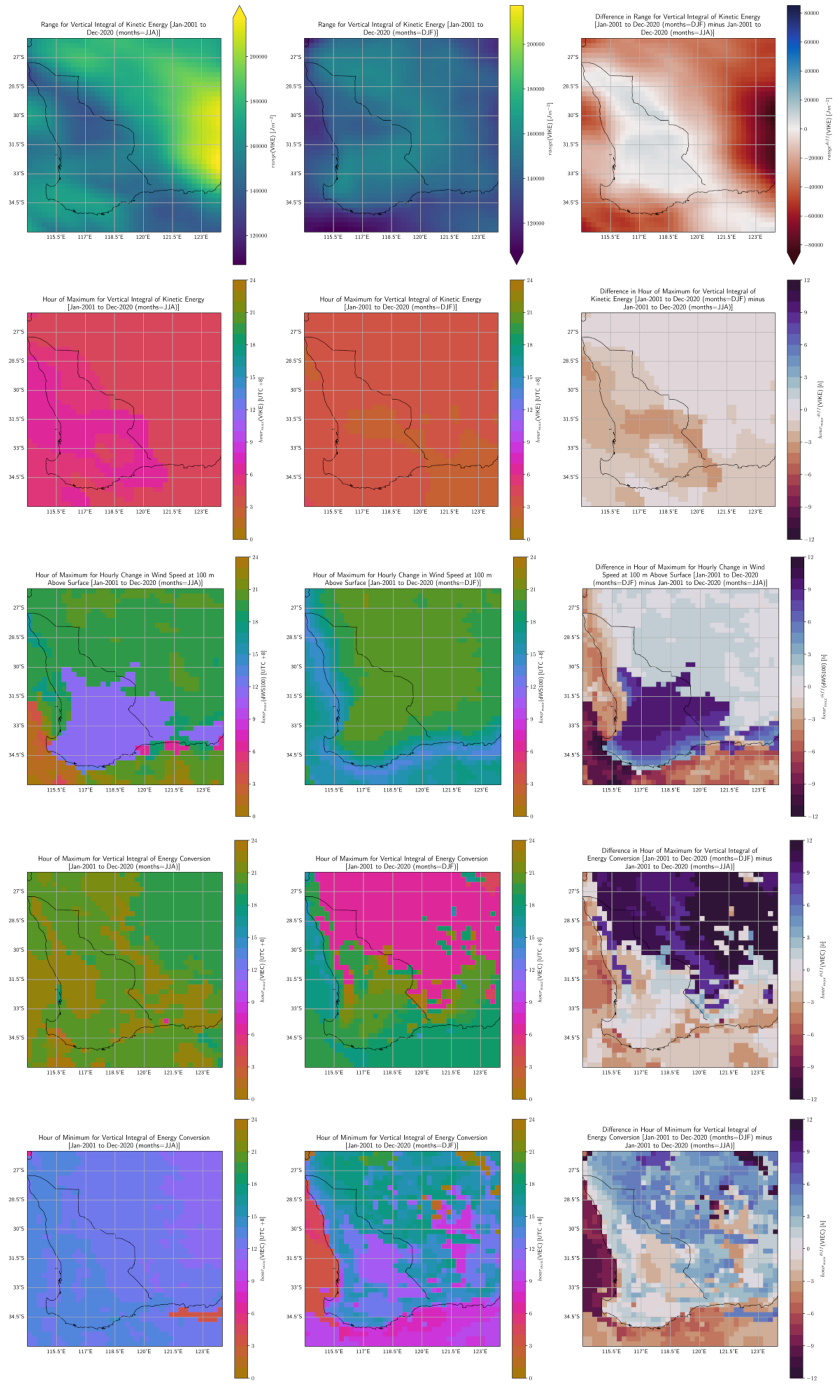

Figure 4.8: Selected MDP statistics (across various variables) which displayed delineations along the fence. Top to bottom: *range*(VIKE), $hour_{max}$(VIKE), $hour_{max}$(dWS100), $hour_{max}$(VIEC), $hour_{min}$(VIEC).

difficult to assess what effect cloud formation (which happens near the boundary layer-free atmosphere interface) might have, because NAC is affected by assimilation cycle artefacts during these hours (see Appendix A.4).

4.5.1.3 | Possible role of soil moisture

Modelling by Martius et al. (2021) suggests that soil moisture can have significant effects on the upper atmosphere. But to the extent that this is generally true of GCMs, the spatial pattern can also be interpreted as an artefact arising from sensitivities in the ECMWF Integrated Forecasting System (IFS) (which produces the ERA5 dataset). As VIKE is a measure of *horizontal* kinetic energy, this may affect the surface wind resource. But it is not clear how ($range$(WS100) does *not* show a similar pattern; not shown).

4.5.2 | Possible influence of agriculture on dWS100

Figure A.5 displays a somewhat marked distinction across the fence for $hour_{max}$(dWS100) in JJA. But the distinction does not sharply match the fence delineation. The results appear to suggest that wind speeds increase at the fastest rate around noon on the agricultural side and around the evening ABL transition on the native side. max(dWS100) displayed an increase from JJA to DJF over the entire region, with no obvious distinction across the fence (not shown). It is not known what is causing these results and whether this is reflecting an assimilation cycle artefact in ERA5 which we missed (see Appendix A.4).

4.5.3 | Effect of native vegetation on phase of VIEC diurnal cycle

4.5.3.1 | Minimum VIEC

Figure A.5 displays a delineation along the SBFWA for $hour_{max}$(VIEC) and $hour_{min}$(VIEC) in DJF. The bare agricultural cover in DJF sees most negative VIEC around noon, probably due to surface heating producing uplift of air. The native side sees most negative VIEC (maximum uplift) at around the evening ABL transition, well past the prime hours for solar heating. This is possibly associated with atmospheric condensation (in line with the CIAD framework), but this is difficult to confirm due to assimilation cycle artefacts in NAC during these hours (see Appendix A.4).

4.5.3.2 | Maximum VIEC

Interestingly, most positive VIEC (minimum uplift) on the agricultural side also occurs around the evening ABL transition. This indicates the possibility for atmospheric energy exchanges across the fence, where rising air on the native side spreads outwards then sinks on the agricultural side before returning to the native side. This would be consistent with the flux of atmospheric moisture convergence towards the native side of the fence noted in Section 4.4.5.2.

4.5.3.3 | Divergent wind changes during evening

Hourly means analysis for WV100 in DJF reveals that surface winds have a southeasterly to southwesterly direction around this time (see Figure 4.9), and is perpendicular to the fence only in the northern part of the fence, so any fence breezes which exist appear to be weak relative to the synoptic background. Nevertheless, there is evidence for a fence breeze effect in dWV100, as strengthening of the southeasterly winds near the southern part of the region (marked by red arrows in Figure 4.9) is biased towards divergent directions (towards both the coast *and* the fence). Similar results appear for hourly means analysis from 1600-2000 LT (not shown).

Modulation of convergence That is, there is a component of energy exchange flux across the fence, as well as a component of the moisture convergence flux towards the fence displayed in Figure 4.7, which appears to occur in a direction *perpendicular* to that of the prevailing wind direction. In this picture, the native vegetation is not necessarily increasing moisture convergence on the native side of the fence by drawing winds directly to itself, but rather it does so by modulating where atmospheric convergence (reflected by effects on VIEC) occurs so that there is a flux of localised mass density changes across the fence.

Possible evidence for CIAD A further observation is that the magnitude of dWV100 in DJF near the northern part of fence is higher than that at the nearby coast despite there being a weaker contrast in dT2. So delineations of temperature change along the fence alone appear unable to account for the observed patterns, especially since higher elevations on the native side of the fence (see Figure 4.1) imply a weakening agricultural breeze during the evening transition on top of this. But these results would be consistent under the CIAD framework due to atmospheric condensation during the evening transition causing a decrease in pressure on the native side of the fence. Hourly means analysis for NAC does indeed show a local maximum around the evening transition

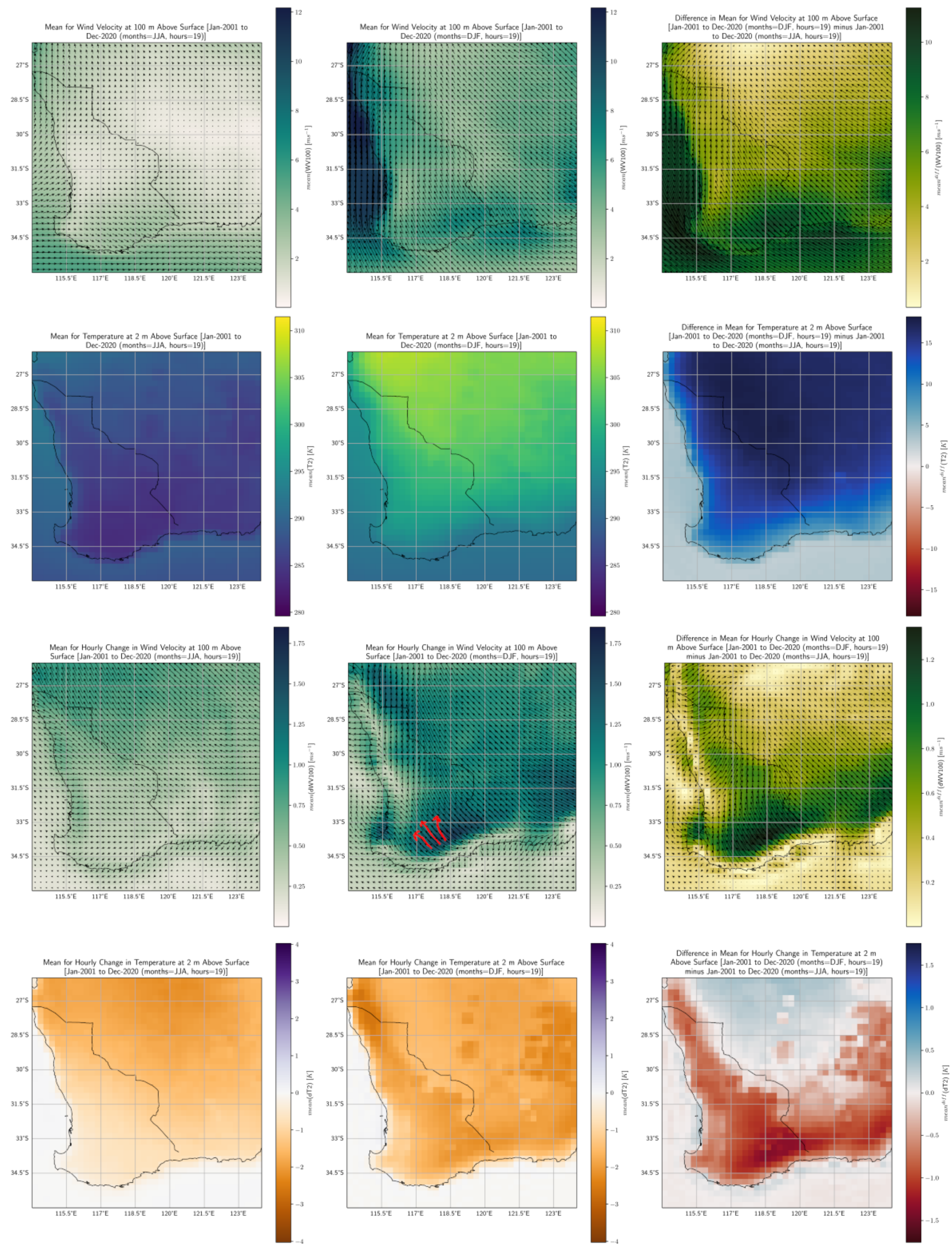

Figure 4.9: 1900 mean JJA and DJF values for WV100, T2, dWV100 and dT2. Red arrows (exaggerated) highlight the divergence in hourly wind changes. Magnitude of dWV100 near northern part of fence is higher than nearby coast despite weaker contrast in dT2.

(not shown) but results are confounded by assimilation cycle artefacts in ERA5 (see Appendix A.4).

4.5.4 | Direct link between native vegetation and NAC

4.5.4.1 | Clouds prefer native vegetation, in summer

Studies by Lyons (2002); Lyons et al. (1993, 1996); Nair et al. (2011); Ray et al. (2003) already clearly demonstrate the sensitivity of cloud formation to type of vegetation cover (see Figure 2.1), and argue this is the result of differences in surface heat flux partitioning causing differences in boundary layer thickness.

MDP means for DJF in Figure 4.10 display significantly greater values for SSHF, BLH and NAC on the native side of the fence, with sharp delineation at the fence (and these appear to arise from lower albedo), giving further support to these authors' arguments and the notion that "clouds prefer native vegetation" (Lyons, 2002) (at least in summer).

4.5.4.2 | Other contributions to NAC

However, this may not be the full picture as the trends for SSHF, BLH and NAC do not fully correlate with each other. BLH appears to also be correlated with LSE (compare with Figure 4.1) and this may possibly arise from wind shear effects.

CCN particle size distributions resulting from native vegetation Volatile Organic Compound (VOC) release forming Secondary Organic Aerosol (SOA) may also affect NAC patterns. Hourly means analysis reveals that night time condensation on the native side of the fence for DJF is slightly higher than on the agricultural side of the fence, even when SSHF is practically the same on both sides. If the CIAD framework is valid, then another possible contribution is that moisture advection towards the native side of the fence (as observed in Figure 4.7) may then have a domino effect in making condensation further west of the fence more likely.

4.5.4.3 | Revisiting causation between VIEC and NAC

Throughout the analysis of our results, we have turned to the question of whether positive NAC (cloud formation) is primarily the result of negative VIEC (rising air) or whether it is other way around (in line with the framework of CIAD). Given that more positive NAC in large part appears to directly result from surface energy balance effects, it calls into question yet again what additional causation VIEC might have on top of this.

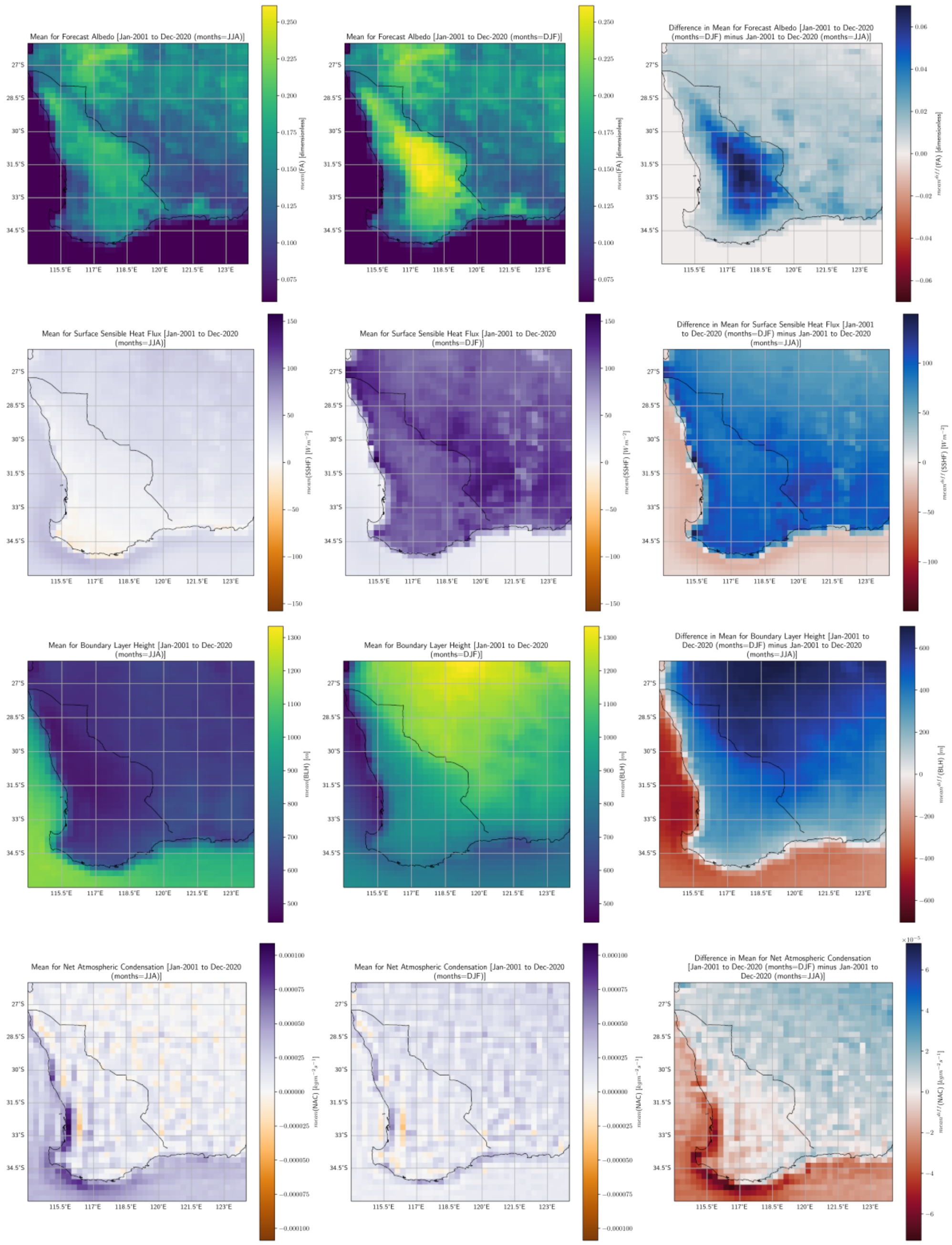

Figure 4.10: MDP means for FA, SSHF, BLH and NAC illustrate how the lower albedo of native vegetation leads to a thicker boundary layer via increased sensible heat for convective mixing, which in turn promotes increased atmospheric condensation (cloud formation).

Contribution from SSHF There is very limited causation from VIEC to SSHF since the former is an atmospheric process and the latter is mostly a surface effect. So the remaining argument against CIAD is either that SSHF (perhaps in confluence with topography) produces the observed uplift of air masses which then leads to condensation (i.e. VIEC is an intermediate cause between SSHF and NAC), or that SSHF simultaneously causes similar patterns in VIEC and NAC via separate mechanisms (i.e. SSHF is a confounding factor leading to a spurious correlation between VIEC and NAC).

SSHF alone cannot account for VIEC But neither of these seem to be the case because while the correlation between VIEC and NAC continues to hold during the JJA months, hourly means analysis reveals that SSHF actually displays the opposite trend to these variables as it does in DJF. That is, SSHF during JJA is suppressed over agricultural land due to irrigation of crops, but all the while there is increased condensation with a very likely cause from increased evapotranspiration, and there is a correlated change to more *negative* VIEC values (more uplift) despite the *decreased* SSHF. Analogous results also apply on the native side of the fence with decreased evapotranspiration from native plants during JJA. Furthermore, SSHF is not at all correlated with any of the coastal effects observed in JJA (see Section 4.4.5).

In summary, the idea that NAC plays a causative role in VIEC (possibly then leading to feedback) appears better supported by the available evidence than the idea that NAC is a passive result of VIEC.

4.6 | Similar comparison

4.6.1 | Study periods

4.6.1.1 | Selected periods

For WA, the selected periods for the similar comparison was from Jun-1997 to May-2002 and from Sep-2010 to Aug-2015 (see Figure 4.11).

Between these periods was extensive vegetation loss concentrated along the coastal forests (see Figure 4.12), resulting from a mix of drought events and human activities such as mining and forestry (beyond vegetation clearing, these activities are also implicated in causing a drop in the region's water table (Gordon et al., 2003; Johnson and Wright, 2003; WA Department of Water and Environmental Regulation)).

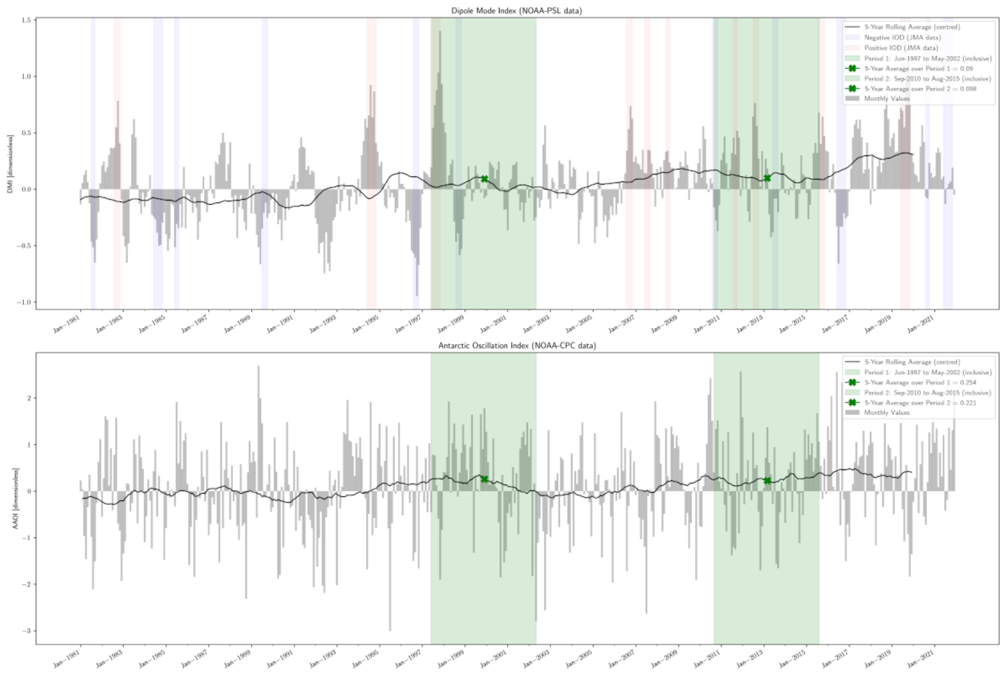

Figure 4.11: NOAA climate indices for climate drivers in WA. Green shading highlights selected periods. Blue and red shading highlight negative and positive IOD events respectively.

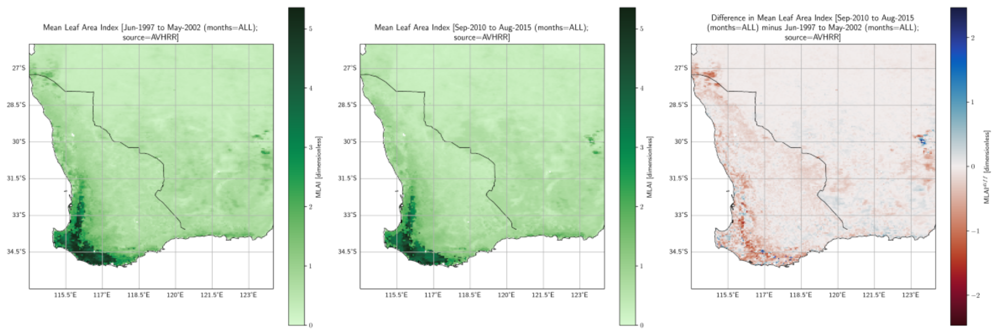

Figure 4.12: MLAI computed over each period in the similar comparison (left and middle), as well as the difference in these values between the two periods (right).

4.6.1.2 | Comparable values in climate indices

The main climate drivers for this region are the IOD and AAO (also known as SAM) (WA Department of Primary Industries and Regional Development, 2021b). The corresponding indices are the DMI and AAOI respectively, and these = have similar averages over these periods. In fact, the 5-year averages over all the indices apart from the EPOI (which is distant and not expected to have significant effects[9].) have very similar values (not shown), although they appear to span across different phases for the longer-term oscillations.

4.6.1.3 | Summary of IOD events

The period from Jun-1997 to May-2002 contains one Negative IOD event and one Positive IOD event, both of which display relatively high magnitudes for monthly values. Although the period from Sep-2010 to Aug-2015 contain two Negative IOD events and two Positive IOD events, each of these display relatively low magnitude in monthly values and so should still be comparable against the first period.

4.6.2 | Findings

No obviously remarkable correlations with coastal MLAI loss was observed. Occasional delineations along forest cover did occur, but were too inconsistent to rule out the possibility of spurious relationships. It was also difficult to distinguish whether the occasional trends resulted from coastal MLAI loss or modulation of atmospheric differences by the coast itself. However, sharp delineations along the fence are observed again in JJA MDP statistics despite minimal MLAI loss around here, indicating that land cover imposes a local modulation upon changes in the synoptic background.

A change in JJA synoptic conditions between periods sees an increase of MSLP through the region despite increased T2. The MSLP increase in the northern part of the focus region is especially weak due to being offset by increased temperatures (especially on the native side of the fence). There is increased cloud formation (positive NAC^{diff}) in subregions on the native side of the fence despite the increase in surface pressure. As with previous results, more positive NAC^{diff} correlates with more negative $VIEC^{diff}$. $VIEC^{diff}$, NAC^{diff} and $VIDMF^{diff}$ all show sharp distinctions along the fence, with increased moisture convergence on the native side of the fence. See Figure A.3.

While agricultural crops continued to transpire under the drier conditions, native vegetation reduced its transpiration, with a sharp decrease in its MDP maximum. This in turn led to dramatic fence delineations in the MDP maximum and minimum for NAC, although this is partially confounded by ERA5 assimilation cycle artefacts (see Appendix A.4). *range*(VIKE) for JJA continued to show delineation along the fence, but less so along the coastal forests, and a delineation is observed in the hour of *minimum* rather than maximum. It is not clear what causes these VIKE effects. See Figure A.4.

[9] Significant effects from teleconnections are possible but we have assumed this isn't the case here

5

Extended Discussion

5.1 | Conceptual framework for assessing effect of land cover on local circulations

We present here a conceptual framework for local circulations based on heuristical principles. We do not suggest that the following is a rigorous formulation but we do believe it captures the general features while being internally consistent, and explains much of the seemingly disparate findings noted in the literature (see Section 5.1.6).[1]

5.1.1 | Main circulation drivers from first principles

- All wind energy ultimately derives from solar energy and can be divided into: internal energy (related to temperatures), latent energy (related to moisture), kinetic energy (related to winds) and gravitational potential energy (related to gravity).

- Initiation or strengthening of a circulation corresponds to an increase in kinetic energy (local to the volume of air in circulation). As the sun does not directly impart kinetic energy upon the air, energy for this must be derived from internal or latent energy (which the sun's energy first induces changes upon).

- Gravity by itself cannot be a driver for convective circulations because it is always directed downward. To be clear, gravity does play a mediating role as conversions from internal and latent energy into kinetic energy often undergo an intermediate energy conversion into gravitational potential energy first. The downwards direction of gravity imparts a directional preference for circulations upon internal energy conversion into kinetic (colder air masses sink while warmer air masses

[1]Although, it should be noted that this framework and the heuristical procedure in Section 5.1.4 were created with the thesis results and literature findings in mind. So general applicability of this framework and the heuristical procedure remains to be tested in an "out-of-sample" setting.

rise due to their relative densities), and as we'll argue later, also for latent energy conversion into kinetic.

- In an idealised circulation which is localised in space, the long-run average conversion of gravitational potential energy to kinetic is zero as parcels of air that go up also come down in the other leg of the circulation. This is in contrast to internal and latent energy conversion into kinetic which may derive from external inputs into the local circulation (via radiative heating and moisture transport respectively). It is in this sense that we mean that gravity cannot drive circulations.
- Thus the main drivers for convective circulations must be:
  - Temperature gradients (associated mostly with diurnal heating patterns and energy balance for different surfaces): internal energy is lost as heated air decompresses to equalise built up pressure from surface heating and cools down in the process of doing so (under approximate assumptions of ideal gas so that PV = nRT and that the total volume of air in circulation is changing relatively slowly).
  - Atmospheric condensation (i.e. cloud formation): latent energy stored in water vapour is lost as the accumulated moisture from evapotranspiration condenses out and is used up by clouds.
  - In both of the above processes, energy is conserved since heated air (whether from built up internal energy or latent heat warming) eventually cools down in the return circulation so that average kinetic power generation within the volume of air in circulation is approximately zero *in the absence of external energy input into the system*. However, the sun *does* contribute an input of energy into the system in the form of daytime heating producing internal (thermal) energy and evapotranspiration of liquid water producing latent energy.
  - A crucial distinction is that whereas the former contribution is mostly localised in space and time to the volume and event of the circulation, latent energy buildup can occur at a distant point in space and over a relatively long period, then at a later time enter the volume of air in circulation. The implications of this are discussed later.
  - The condensation-induced airflows will be anisotropic and directed upwards. The possibility for anisotropic airflow is convincingly demonstrated in a series of experiments by Bunyard et al. (2015, 2017, 2019). See Appendix B.3 for a heuristical argument as to the causes of this anisotropy.

5.1.2 | The effect of temperature gradients

- Higher surface temperatures are associated with lower surface pressure (as air rises), and the converse for lower surface temperatures (as air sinks).
- Temperature at each surface is in turn governed by the surface energy balance $SLHF + SSHF = R_n - G$ where R_n is net radiation and G is ground flux.
- R_n is determined mostly by albedo, surface thermal properties and solar irradiance (which may be affected by cloud cover).
- G is determined mostly by soil moisture (for vegetation cover) and surface thermal properties (for urban cover), and for vegetation cover can in many cases be assumed approximately proportional to R_n (Lyons et al., 1996).
- The partitioning between Surface Latent Heat Flux (SLHF) and SSHF is determined primarily by plant species behaviour in relation to environmental factors such as soil moisture, temperature, solar irradiance, etc. for natural and agricultural land cover. For agricultural lands, these factors fluctuate significantly according to the cropping cycle and as a result so too does this energy partitioning.
- The greater the evapotranspiration the greater the SLHF, and so for the same R_n (assuming G is proportional to R_n) this means lower SSHF.
- SSHF in turn ends up being converted into
  - The thermal energy of the surface air up via conduction with the surface: an account of this can be used to assess likely temperature gradients.
  - The kinetic energy and gravitational potential energy from local scale convections and turbulent mixing with the result that air parcels reach a greater height and hence BLH is increased.
- SLHF corresponds with the amount of moisture being added into the atmosphere in the form of water vapour, which in turn increases relative humidity and hence a decrease in LCL.

5.1.3 | The effect of atmospheric condensation

- Atmospheric condensation occurs when BLH is greater than LCL and there is sufficient atmospheric moisture.
- Sustained condensation requires a continued supply of atmospheric moisture.

- A low pressure region forms under and around the area of condensation, which induces a circulation (whereby air is directed upward towards the site of condensation, then outward and downward in a return circulation).
- Shortly after initiation of condensation, a horizontal pressure gradient forms (due to the sudden loss in volume from water vapour condensing to liquid form) which advects surrounding moisture to sustain continued condensation. The upward air motion immediately preceding this and which was then directed outward eventually replaces the advected air to conserve matter fluxes. Meanwhile, to conserve energy fluxes, the latent heat released above cloud base and which was contained by air in the return leg of the circulation is eventually absorbed by surface air (which would have lost heat in the process of decompressing in the presence of the horizontal pressure gradient).

5.1.4 | Heuristical procedure for qualitatively assessing likely effect of land cover on strength and direction of circulations

1. Assess the BLH at each point in the study region.
   - For calm conditions, this is determined primarily by (and positively correlated with) the SSHF at each point.
   - For windy conditions, this is determined by
     - The SSHF *upwind* of each point (since wind traversing through the upwind region is subjected to buoyancy forces determined by the SSHF in that upwind region, and is then carried through by its inertia, arriving at an increased height by the time it reaches each point.
     - The surface roughness (the rougher the surface the more turbulent mixing and so the higher the BLH)
     - *Upwind* orography (winds hittin an incline may be deflected upwards upon hitting an incline)
   - Apart from upwind orography, localised peaks in the BLH at each point may also occur where there is an abrupt interface *upwind* where winds go from a surface with lower to higher roughness (in a similar effect to that of orography, the winds are slowed down and concentrate near the interface then must extend vertically to equalise the pressure buildup). This is unless the region of lower roughness happens to be very short along the direction of wind travel, and there exists another surface immediately upwind with a

roughness equal to or higher than the downwind high roughness surface (because this implies a lower volume of space for the winds to expand into then deflect upwards from upon reaching the second interface).

2. Assess the LCL at each point in the study region.
   - This is a function of surface temperature, pressure and Relative Humidity (RH), but mostly RH.
   - For initially calm conditions, RH is determined primarily by evapotranspiration, for which SLHF is an indicator for. RH for areas without high evapotranspiration but with a characteristic spatial scale much smaller than neighbouring areas which have high evapotranspiration may also have high humidity as neighbouring moisture drifts towards it.
   - For windy conditions, RH is determined primarily by *upwind* evapotranspiration, for which SLHF is a proxy for. However, unlike the case for SSHF with regards to BLH where the BLH at each point is determined by SSHF immediately upwind of the point, the evapotranspiration / SLHF can be of a very remote origin if there is negligible upwind condensation (i.e. winds may carry moisture from afar as in the case of a sea breeze).
3. Identify areas where BLH is greater than LCL.
   - This is where atmospheric condensation (cloud formation) will occur.
   - The atmospheric condensation will induce a local decrease in surface pressure and advect moisture towards itself (at least on local scales, and possibly larger scales).
4. Assess for these areas what the following moisture flow is likely to be, in context of the synoptic background.
   - If there is sufficient moisture local to where the atmospheric condensation is occurring, or there is sufficient moisture from far away sources (e.g. a sea breeze, in which case SST needs to be considered) which synoptic conditions are not inhibiting, then the atmospheric condensation can be sustained and a circulation will develop such that surface winds (and moisture) are directed towards the sites of condensation (at least on local scales). The greater the amount of condensation, the more intense the circulation and winds.

- As regards circulations and winds at a larger (e.g. synoptic) scale, the Coriolis force needs to be taken into consideration when the study region is outside of the Tropics.
- Sustained atmospheric condensation may also inhibit nearby cloud formation due to advection of moisture from neighbouring regions but also because the downward leg of the resulting circulation may increase the surface pressure of neighbouring regions (i.e. downward winds prevent moist air from rising to the LCL). This in turn may increase the net radiation and hence evapotranspiration from nearby vegetation, providing even more moisture to sustain continued atmospheric condensation (and hence the circulation).
- As such, subsequent circulation and convective developments may be dependent on initial conditions as to where and with what spatial pattern the atmospheric condensation first manifests.

5. Assess the temperature gradient across different surfaces.

   - All other things equal, circulations should be such that surface winds move from cooler regions (higher surface pressure) to warmer regions (lower surface pressure).
   - If BLH is less than LCL at almost all points or there is insufficient moisture for sustained atmospheric condensation at the points where BLH is greater than LCL, then the temperature gradient effect should dominate.
   - For cases where the predicted wind flow from atmospheric condensation and temperature gradients oppose each other, the relative contribution of each mechanism needs to be considered.

6. Some rules of thumb in assessing SSHF and SLHF.

   - Agricultural lands typically employ annual crops, which compared with natural land cover have higher albedo (lower SSHF + SLHF total), lower roughness, and greater annual variation in the Bowen ratio (which is lower during the growing season). When there is bare land cover after harvest, the albedo and Bowen ratio during this time is likely to be especially high. Where there is dry soil, clearing of vegetation may actually increase SSHF despite increases in albedo, as the Bowen ratio increases.
   - Natural land cover such as native vegetation and forests, as compared with agricultural land cover, typically have lower albedo (higher SSHF + SLHF

total), higher roughness, and a Bowen ratio which is low for ecosystems adapted towards moist conditions but high for dryland species. There will be significantly less annual variation as compared with agricultural land. Natural land cover will typically have higher SSHF than agricultural unless the latter is so bare that SLHF becomes negligible (as can be the case between harvest and the next growing season), while at the same time the former is an ecosystem adapted to wet environments with very low Bowen ratio.

- Differences in SSHF and SLHF across different land cover types can in part be offset by differences in fractional vegetation cover (Mahmood et al., 2011).
- Open bodies of water have low Bowen ratio and cool surface temperatures so they usually mark the downward leg of a circulation and daytime atmospheric condensation in these areas *may* be suppressed (Cutrim et al., 1995).
- Urban areas have an albedo which depends on local urban design, but a roughness and Bowen ratio which is typcally higher than both natural and agricultural land cover, and these variables display little annual variation.

5.1.5 | Speculations

- The initial spatial pattern of atmospheric condensation may affect how much total moisture will be advected to sustain that initial condensation over the course of the circulation's lifetime. If the same amount of water vapour is condensed over a larger volume of air and over a similar period of time, there is a lower volumetric power density (and weaker pressure gradient force per unit area perpendicular to the base surface of the cloud averaged over the period of condensation) which may not reach a critical threshold for sustained convection. Self-sustaining cumulus formation is achieved where moisture is being advected into the cloud at a quick enough rate that the resulting local power density will in turn advect more moisture at a quick enough rate to do the same and continue the cycle. In the case that the moisture is oceanic in origin, this may translate to an increase in the average amount of atmospheric condensation and precipitation for each occurrence of a condensation-induced circulation. Even if on average the total atmospheric condensation is independent of initial spatial pattern of formation, the higher volumetric power density associated with condensation over a smaller volume of air may still lead to appreciable effects in circulation such as an increased prevalence of short but intensive bursts (in favour of slow and sustained circulation).

- If the above is correct, then biogenic aerosol release (or SOA formation from biogenic VOCs) may play a role in determining that initial spatial pattern, where subsequent condensation and rainfall will be concentrated, and may also determine the amount of condensation that will occur before the cumulus can no longer sustain its own moisture and the circulation's lifecycle ends.

- If the above 2 speculations are correct, we further speculate that cloud inhibition upon neighbouring areas is a *competitive* mechanism between ecological communities (at least in flat terrain). While the downward leg of the cumulus convection inhibits upwards air movement from neighbouring regions, the horizontal return leg also advects away neighbouring moisture and possibly CCN. The ability for an ecological community to induce favourable rainfall upon itself constitutes a selectional advantage and the ordered structures required to enforce such a mechanism would be subject to decay over time (e.g. due to mutations in individual species, or weeds crowding out and changing the species in an ecological community). The fact that water is essential for terrestrial life and that this mechanism persists to this day suggests that there must have been competitive selection between ecological communities to maintain these ordered structures (whereby communities unable to do so are at a competitive disadvantage and the communities able to do so give rise to progeny who retain this feature) (Gorshkov et al., 2000). If this is correct, then in assessing circulation changes due to LCC, a distinction needs to be made between natural and managed forests, where ecosystems which have been subjected to greater anthropogenic change are likely to display more chaotic and random initiations in atmospheric condensation.

5.1.6 | Results and literature cast within conceptual framework

- Lyons (2002) noted clouds forming first and bunching up on the native vegetation of the fence during summer for southwest WA. The native vegetation in southwest WA has higher SSHF *and* SLHF (indicating evaporation for atmospheric moisture) than bare cover during summer (Lyons et al., 1996). There is also possibly the contribution of biogenic aerosols acting as CCN. Thus clouds preferentially form over the native side, but most moisture is still oceanic in origin and arrives via a sea breeze. So initial condensation occurs close to the fence itself, and subsequent condensation has a tendency to be concentrated near this initial area due to the positive feedback between condensation and convection, as well as the return circulation advecting moisture to itself. The result is a bunching up of clouds on the native side of the fence.

- Ray et al. (2003) noted preferential cloud formation in Western Australia over agricultural land in Winter but native vegetation in Summer. The summer case follows from previous comments. In the winter case, the use of irrigation and the fact that annual wheat crops transpire very heavily towards anthesis near July (with up to 80% of available energy being used as SLHF) (Lyons et al., 1996), means high surface humidity and hence a lower LCL. The result is preferential cloud formation on the agricultural side despite lower SSHF and BLH.

- Gero et al. (2006) noted the possibility of urban-induced convective storms over the Sydney basin. Moisture for this coastal location is oceanic in origin. The high SSHF from urban structures produces an uplift of the progressing sea breeze. Initial condensation produces further uplift in a self-sustaining cycle to continue feeding oceanic moisture and a convective storm results.

- Knox et al. (2011) noted increases of precipitation towards forest edges but decreases away from edges in Southwestern Amazonia. Winds blowing from farmland is likely to experience a bunching up of mass at the forest edge due to discontinuities in roughness length and SSHF. The mass buildup is relieved by upwards transport, representing a localised peak in BLH which often exceeds the LCL. In the moist environment of the Amazon, this results in cloud formation near the forest edge, and the ensuing circulation produces a downdraft away from the forest edge and moisture advection away from the immediate neighbourhood towards the forest edge in the return circulation. Thus precipitation occurs close to forest edges and decreases away from them.

- Khanna et al. (2017) noted increased rainfall downwind of deforested areas in the Amazon. Moisture here is from nearby forest evapotranspiration. Deforested areas represent localised regions of increased SSHF. Winds carrying moisture which pass through this area experience lift until it reaches the LCL for condensation but before this the moisture would have already travelled some distance downwind.

- Khanna et al. (2017) noted increased cloud cover and rainfall over small deforested areas in the Amazon but the opposite for large deforested areas. Deforested areas which are small relative to neighbouring forest cover inherits the high humidity from nearby evapotranspiration but because it does not evapotranspirate this moisture itself there was no accompanying partitioning towards SLHF. Instead, the small deforested area retains its high SLHF which produces extra uplift for increased cloud formation. Deforested areas which are large relative to neighbouring forests have relatively low humidity. Nearby evapotranspiration condenses into clouds not far (relative to the size of the area) into the deforested area. The ensuing circulations which are near the deforested area borders produce a downdraft towards the centre of the area and advects away moisture in the return circulation. The lack of moisture and downdraft leads to decreased cloud cover over large deforested areas despite higher SSHF.

- Taylor et al. (2022) noted increasing rainfall with increasing amount of deforestation with no apparent trend reversal with increasing area in coastal Southern West Africa. Taylor et al. (2022) further noted that for this location there is an *increase* in temperature associated with the coastal deforestation (unlike the southwest WA case). Unlike the Amazon, the moisture source here is oceanic in origin (rather than from forest evapotranspiration). Increased coastal deforestation here means a stronger sea breeze simultaneous with an increased SSHF (tropical plants here presumably have low Bowen ratio if clearing leads to surface warming). This not only advects more moisture inland but produces the convective mixing for the BLH to exceed the LCL more often. The result is increasing rainfall with no apparent trend reversal with size of deforested area (for now anyway).

- Taylor et al. (2022) noted a concentration of convective cores during the evening transition in coastal Southern West Africa. The sea breeze at this location leads to a buildup of inland moisture during the day. The high humidity and evening cooling conspire to produce an especially low LCL. At the evening transition convective mixing from daytime SSHF is still present and the BLH decreases at a slower rate than the LCL. The result is the LCL overtakes the BLH on the way down and condensation occurs since the condition of BLH > LCL is met. The subsequent condensation leads to convective initiation and a concentration of convective cores is observed during this evening transition window.

- Xu et al. (2022) noted contrasting effects of small-scale deforestation on cloud cover for different forest types. The different forest types, which represent ecosystems in different climatic zones, operate under different moisture regimes. The species which proliferate (under natural conditions) are the ones proven to release the right amount of moisture given its conditions (enough for moisture advection via condensation but not so much that it depletes its own water reserves). A partial corollary to this is the partitioning of surface energy fluxes between SSHF and SLHF, which then affects how much convective mixing there is to increase the BLH and how much moisture is available to lower the LCL respectively. Thus contrasting effects will be seen for different forest types.

5.2 | Limitations, improvements and future directions for research

5.2.1 | Regarding ERA5

- Analysis in this report was done under the assumption that the ERA5 dataset represents a close enough approximation to the ground truth. But all reanalysis data is modelled output and may be subject to processing artefacts. Our results include coastal analysis and ERA5 is known to have decreased reliability at coastal locations or discontinuities in surface roughness (Gualtieri, 2021). In the case of the SBFWA, artefacts over the fence should in theory be minimised by the comparable roughness between agricultural and native cover here (Lyons et al., 2001).

- In our analysis we indirectly inferred the effect of the Leeuwin Current via a combination of results demonstrating increased wintertime evaporation offshore, and literature findings (see Section 4.4). Analysing the SST directly using ERA5 data may yield more accurate insights, including on how well the coastal band of negative VIEC spatially correlates with increased SST.

- In our analysis we used VIEC as an indicator for whether air masses were rising or falling. A more appropriate variable from the ERA5 dataset to use may have been "Vertical integral of divergence of geopotential flux". For the purposes of studying atmospheric energy conversions, "Vertical integral of divergence of kinetic energy flux", "Vertical integral of divergence of mass flux" and "Vertical integral of divergence of thermal energy flux" may also be valuable (Hersbach et al., 2019).

5.2.2 | Regarding study regions

- The conclusions drawn in our analysis would benefit from a cross comparison against other study regions with different climate and geography. This allows testing for generality of the conceptual framework proposed in Section 5.1, and conflicts with principles articulated in this report may elicit novel insights. The original project scope included focus regions for Central America (CA) and Northern Brazil (NB) (see Appendix A.5), but was cut short due to time constraints. Another candidate region for study is China, which has a wealth of literature, decent weather station coverage, human significance due to the number of lives at stake with hydrological cycle disruptions, and contrasting trends between afforestation, deforestation and urbanisation in different subregions. A comparison of the east coast of Australia (and other areas such as Kangaroo Island) before and after the 2019-2020 bushfires may also yield some insights.

- Furthermore, we observed in WA that above native vegetation there are *higher* temperatures. But NB results reveal that *lower* temperatures are often observed over natural forest cover (not shown). Ecosystems in moist climates typically have lower Bowen ratios which may offset the net radiation gain from lower albedo and produces surface cooling rather than heating. To the extent that the troposphere is stratified or there is much warmer air above (i.e. a temperature inversion), a drop in surface temperature may not coincide with descending air masses from above, and may in fact contribute to a *decreased* surface pressure instead.

5.2.3 | Regarding comparisons

- The study periods chosen for the similar comparison were based on having similar 5-year averages in relevant climate indices. This was a best attempt at controlling for atmospheric oscillations but is not ideal since there are non-linearities associated with these indices (i.e. even if if the average is similar, the effects might not be, especially if the time spent in the extremes of the indices for each period are different). There may also be memory effects persisting from recent atmospheric conditions immediately preceding each period. This was likely the case for WA as the second period immediately followed the Millenium drought from 2001-2009 and displayed drier conditions.

- A further "dissimilar comparison" can be made, by selecting a set of periods for which the 5-year averages of relevant climate indicies had *dissimilar* values. The rationale behind this was that were some relationship to be identified in the analysis between *similar* periods, we could evaluate our confidence in that relationship by seeing whether it holds even under extreme differences in atmospheric conditions. This was part of the original project scope but was cut short.

- It may be valuable to apply empirical orthogonal functions analysis to decompose surface wind speeds into their principal components for comparison with LAI or variables for which there is strong evidence that vegetation cover has a modulating effect on (such as NAC, T2, SSHF, SLHF and NSE).

5.2.4 | Regarding CIAD

- It may be worth analysing CIAD patterns in regions with intact forests for a cross-comparison. CIAD in southwest WA appears to occur through modulations in atmospheric and moisture convergence under conducive conditions. As the native plants here operate under and are adapted towards a moisture-limited regime, they may not be able to achieve a condensational power to actually initiate the airflow (as this would deplete its water reserves). In our results we observed evidence of moisture flux towards itself via modulation of convergence but not the actual redirection of wind flow to itself (in the midlatitudes this is further complicated by the Coriolis force). This may be different to the Amazon and Congolian rainforests which transpire so heavily that it may actually initiate the airflow and have winds directed towards itself.

- CIAD is often conceptually described as a vertical pressure gradient forming under the cloud which then translates to a horizontal pressure gradient. But tacit to this picture are assumptions of initially calm conditions. Although this is a convenient conceptual description, it might not be empirically manifested. If mass flux in the subcloud layer toward the point of condensation is high relative to the rate of condensation, then there may be minimal disturbance to *surface* air pressure. In this case, MSLP (observations or modelled output) may not pick up this effect.

- Given speculations that biospheric mediation of CCN may play a significant role in subsequent amount of condensation and spatial pattern of circulations (see Section 5.1.5), future research can also be pursued along this line of enquiry. In the case of southwest WA, results by Junkermann et al. (2009) clearly indicate an influence. A summary of monoterpene and isoprene (VOCs) emissions by different Eucalyptus species is given in (He et al., 2000), while modelled data for various atmospheric substances including isoprene is available in the Copernicus Atmosphere Monitoring Service (CAMS) CAMS Global Reanalysis (EAC4) dataset (Inness et al., 2019).

- Our analysis included a qualitative treatment of atmospheric flows. Quantitative analysis may yield more insights. Relevant equations for this task are presented in Makarieva et al. (2014, 2017).

6

Conclusions and Summary

- The results present strong evidence that the clearing of native vegetation for agriculture in southwest Western Australia has changed atmospheric energy conversions, in part due to changes in the surface energy balance.
- The results present strong evidence that land cover produces local modulations upon background synoptic changes, with typically dampened fluctuations.
- The results present moderate but indirect evidence (from water vapour flows) that surface wind circulation patterns will be affected beyond just effects from roughness length changes.
- The results present moderate evidence in support of the existence of condensation-induced atmospheric dynamics. This includes native vegetation modulation of atmospheric and moisture convergences leading to altered mass and moisture transport respectively.
- The results present moderate evidence that historical land cover change in southwest Western Australia has led to decreases in coastal temperatures which has weakened the summer daytime sea breeze. This has likely caused the observed inland rainfall loss, decreased inland moisture convergence (possibly indicting wind convergence), and an increased coastal flood risk. Meanwhile, the effect of future land cover change is highly variable depending on what type of change takes place.
- For wind energy operation, the implications for this are decreased generation and operating revenue during peak season, increased risk of infrastructure damage from floods, and increased risk embodied from uncertainty regarding what future land cover change will take place. A weakened sea breeze also implies less cool relief to the urban centre of Perth during summer daytime, so a decrease in supply coincides with an increase in demand (see Section 4.4.6).

- A conceptual framework for understanding how land cover affects surface winds was created, along with a heuristical procedure for qualitatively assessing the likely effect of future land cover change on circulation patterns.
- A series of purpose-built Python programs was developed for analysing how vegetation change affects the diurnal and seasonal variations of an arbitrary variable from the ERA5 dataset (see Appendix C).

A

Supplementary information

A.1 | Unmarked figures

A.1.1 | January means for selected variables 1 (unmarked)

The use of coloured markings with thick outline in Figure 4.2 somewhat distorts perception of the trends. For an undistorted view, see Figure A.1.

A.1.2 | January means for selected variables 2 (unmarked)

The use of coloured markings with thick outline in Figure 4.3 somewhat distorts perception of the trends. For an undistorted view, see Figure A.2.

A.2 | Similar comparison results

A.2.1 | Selected MDP means for similar comparison

See Figure A.3 for MDP means results discussed in Section 4.6.2.

A.2.2 | Selected MDP stats for similar comparison

See Figure A.4 for MDP statistics results discussed in Section 4.6.2.

A.3 | Full list of study variables

Some of the key variables studied in this project were presented in Section 3.4. For a full list of variables used in this study, including those which were analysed but for which there were no significant findings, see Table A.1.

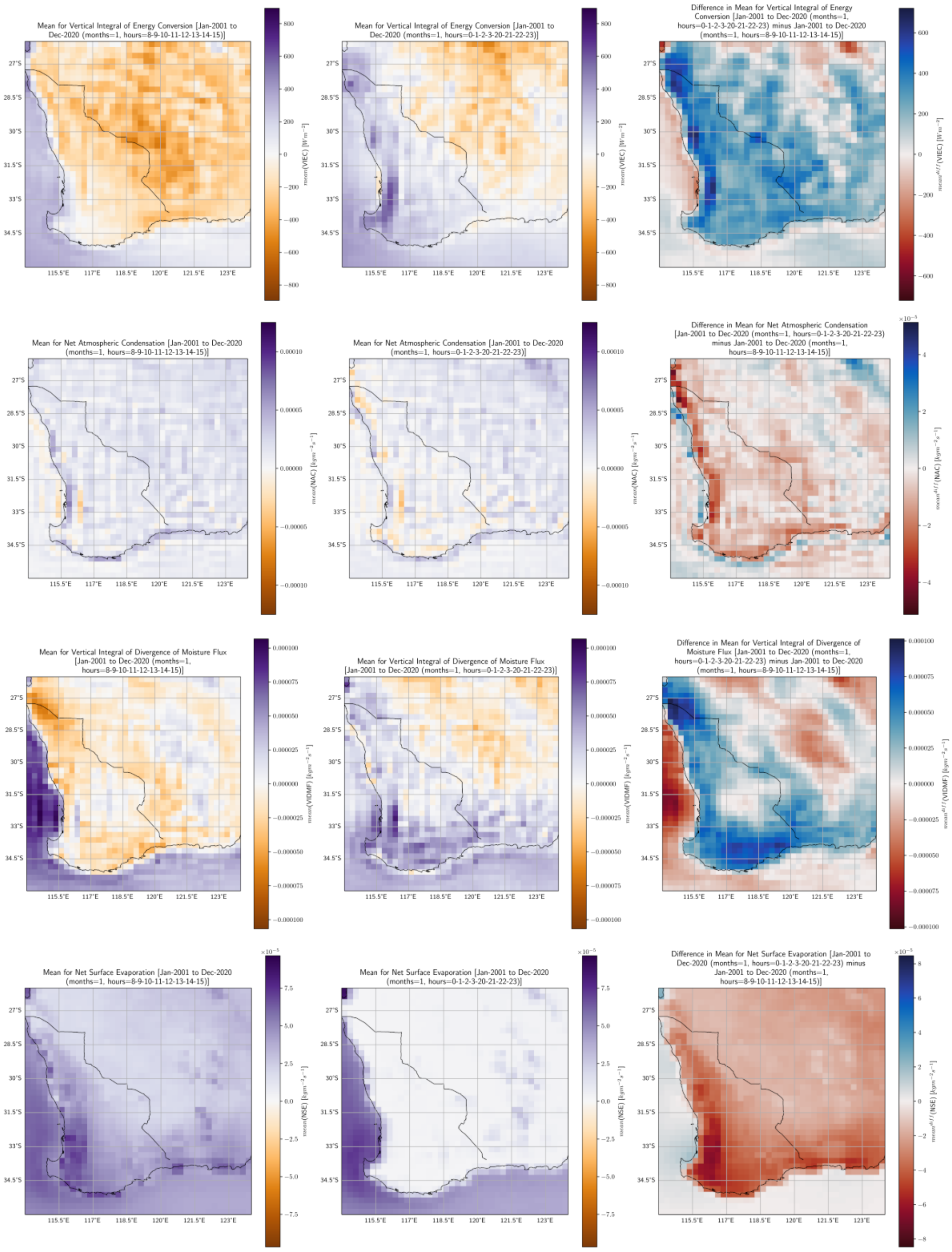

Figure A.1: January mean daytime and nighttime values for VIEC, NAC, VIDMF and NSE.

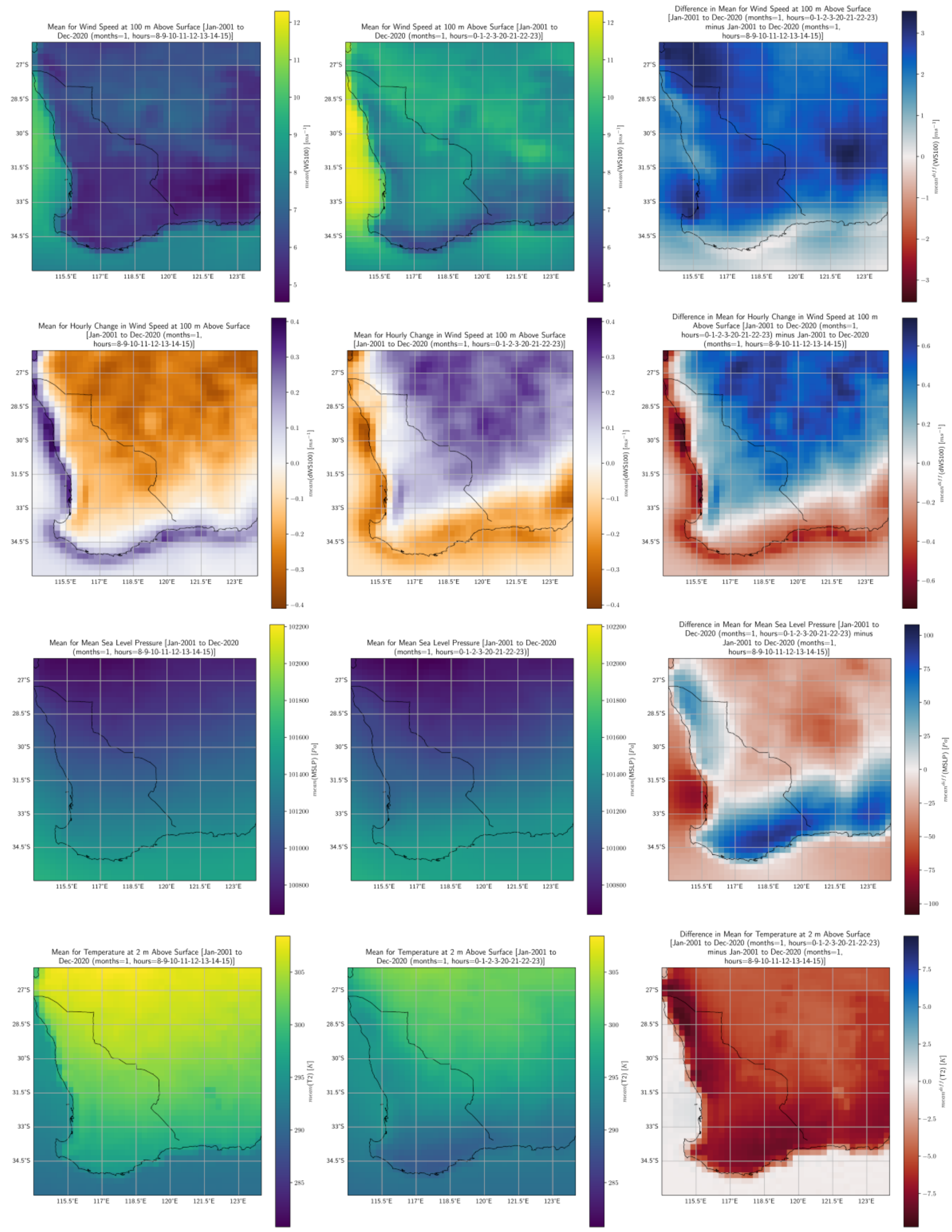

Figure A.2: January mean daytime and nighttime values for WS100, dWS100, MSLP and T2.

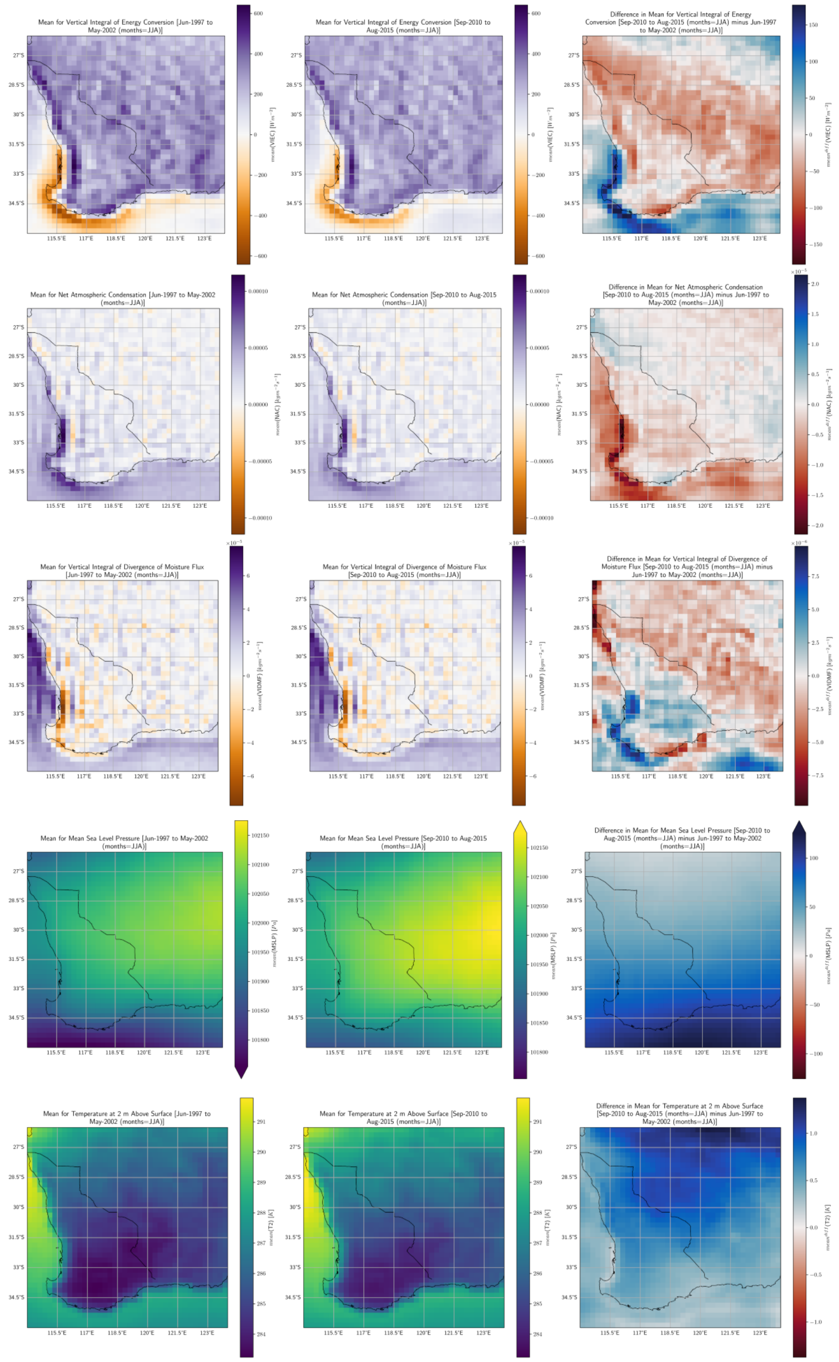

Figure A.3: Selected MDP means (across various variables) for similar comparison which displayed delineations along the fence. Top to bottom: *mean*(VIEC), *mean*(NAC), *mean*(VIDMF), *mean*(MSLP), *mean*(T2).

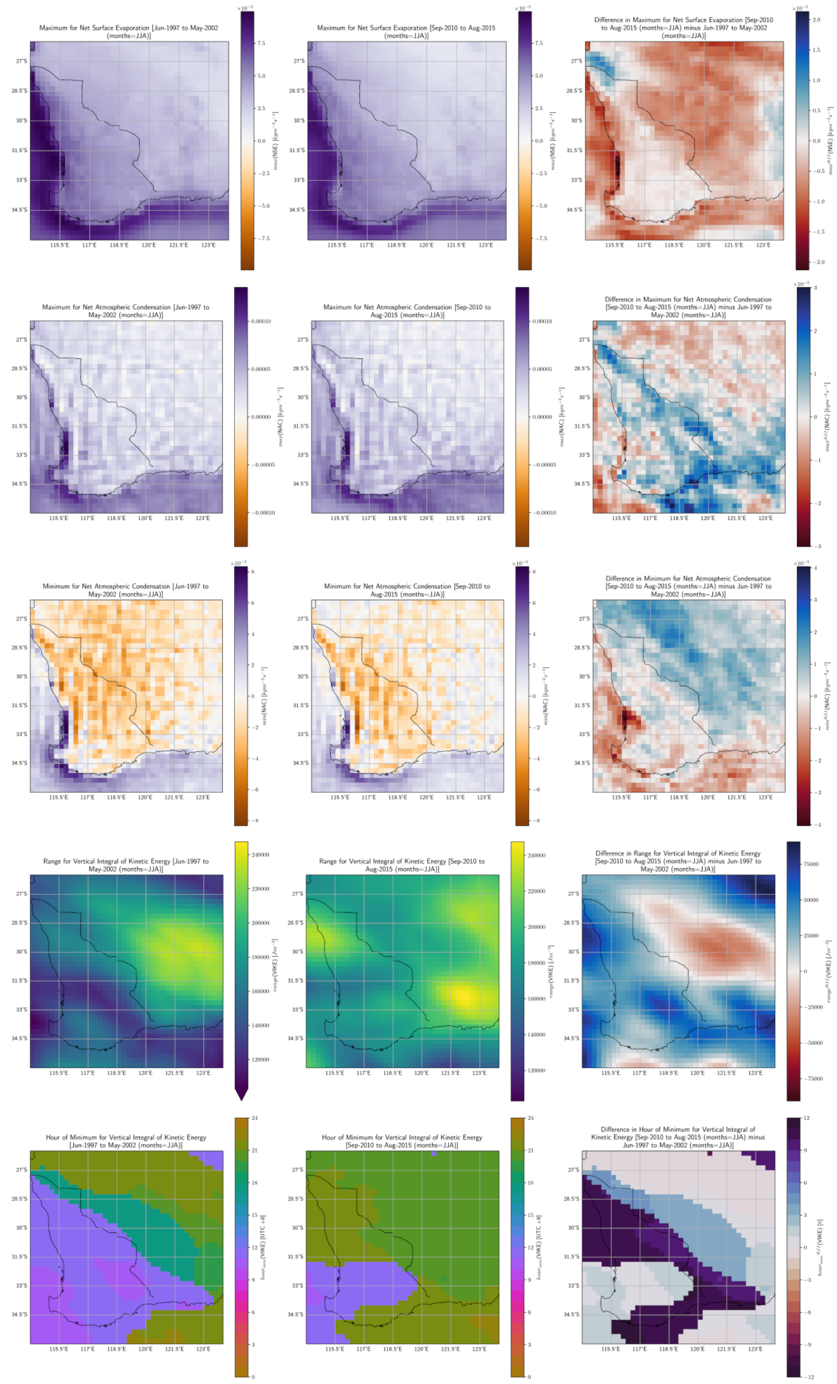

Figure A.4: Selected MDP statistics (across various variables) for similar comparison which displayed delineations along the fence. Top to bottom: max^{diff}(NSE), max^{diff}(NAC), min^{diff}(NAC), $range$(VIKE), $hour_{min}$(VIKE). Note that NAC stats have artefacts (see Appendix A.4).

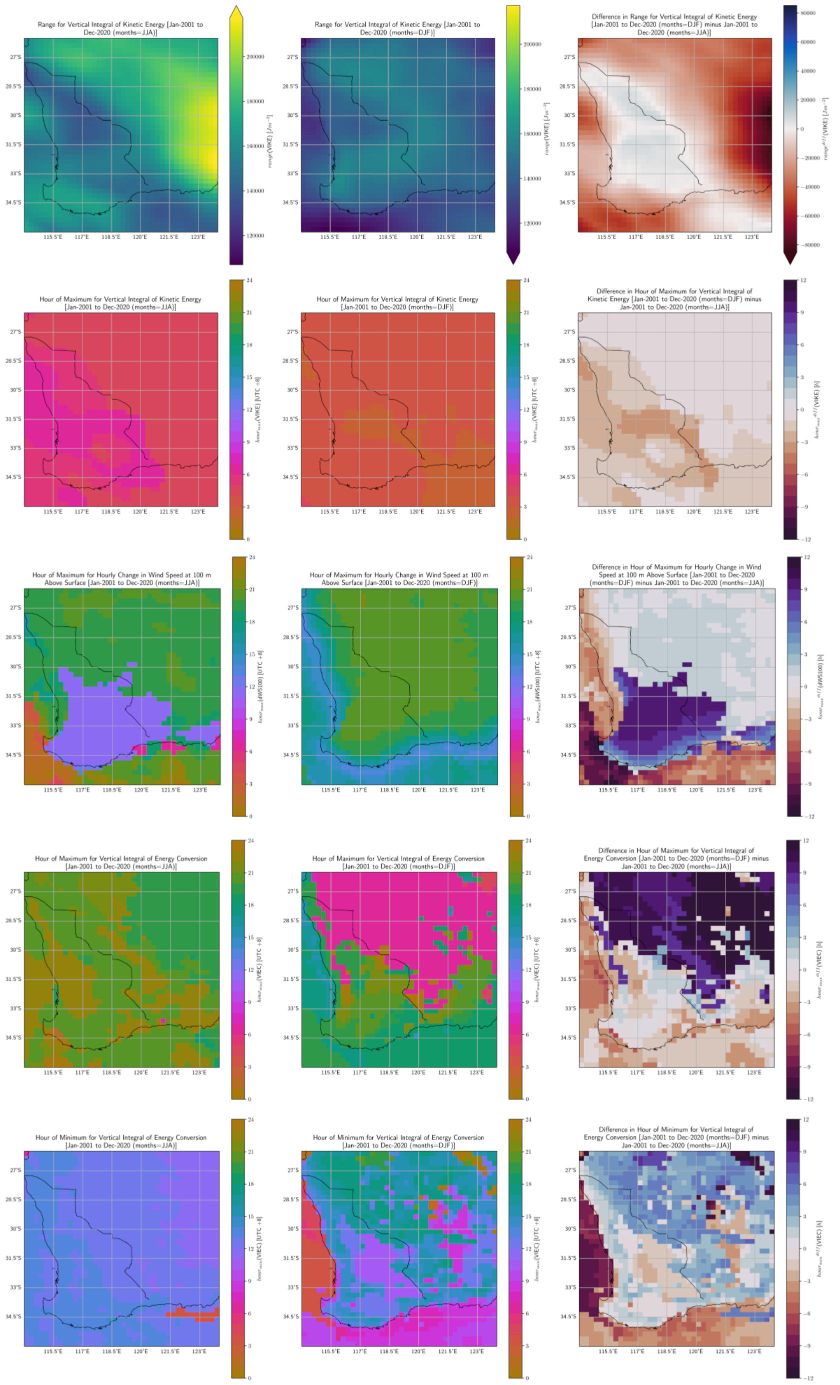

Figure A.5: Selected MDP statistics (across various variables) which displayed delineations along the fence. Top to bottom: *range*(VIKE), $hour_{max}$(VIKE), $hour_{max}$(dWS100), $hour_{max}$(VIEC), $hour_{min}$(VIEC).

Table A.1: A full list of variables which were analysed. Abbreviations for these variables as used in the report are provided, along with descriptions of each variable.

Abbreviation	**Variable**	**Description**
LSE	Land Surface Elevation	Units in m. Elevation of the land surface above sea level. Obtained by converting from ERA5 geopotential data using the MetPy Python library (May et al.).
SSGO	Slope of Sub-Gridscale Orography	Dimensionless. Represents slopes of orographic features such as mountains and hills which are present down to a scale of 1 km. Flat surfaces have value 0 while vertical cliffs have value 1.
MLAI	Mean Leaf Area Index	Dimensionless. The LAI index for a grid cell is the total leaf area divided by ground area of that cell. MLAI is the mean of this over the study period. This was the main metric used in assessing vegetation cover and vegetation cover change.
MFAPAR	Mean Fraction of Photosynthetically Absorbed Radiation	Dimensionless. The FAPAR for a grid cell is the fraction of radiation between 400-700 nm wavelength absorbed within that cell. MFAPAR is the mean of this over the study period. This was a supplementary metric used in assessing vegetation cover and vegetation cover change.

(continued. . .)

Abbreviation	Variable	Description
BLH	Boundary Layer Height	Units in m. Height of the depth of air for which surface effects are significant. This was used to assess level of convective mixing and likelihood fo cloud formation.
CAPE	Convective Available Potential Energy	Units in Jkg^{-1}. Work which would be performed on an air parcel if it rose through the atmosphere. This was used to indicate atmospheric stability. The more positive the more air will rise, the more negative the more air will sink.
CBH	Cloud Base Height	Units in m. Height for base of lowest cloud. This was used to assess how height of cloud formation may affect atmospheric circulations.
FA	Forecast Albedo	Dimensionless. Fraction of short-wave radiation reflected from surface. This was used to assess how reflectivity of different land cover affects the surface energy balance.
MSLP	Mean Sea Level Pressure	Units in Pa. Pressure of atmosphere adjusted to sea level. This is one of the main variables affecting wind. High values typically coincide with calm conditions while low values coincide with windy. This was also used to identify synoptic features.

(continued. . .)

Abbreviation	Variable	Description
NAC	Net Atmospheric Condensation	Units in $kgm^{-2}s^{-1}$. Condensation minus evaporation in atmosphere (does not include surface). Positive values indicate more cloud formation than cloud evaporation. Calculated using ERA5 data for TCWV, NSE and VIDMF (see Appendix B.2). This is one of the major factors affecting the partitioning of the atmospheric energy budget.
NSE	Net Surface Evaporation	Units in $kgm^{-2}s^{-1}$. Evaporation minus condensation at surface (does not include atmosphere). For vegetation, positive values indicate a greater amount of evapotranspiration than dew formation. Instantaneous values are approximated by averaging consecutive ERA5 accumulation values.[1]
SLHF	Surface Latent Heat Flux	Units in Wm^{-2}. Rate at which energy at the surface is being used for evapotranspiration. Instantaneous values are approximated by averaging consecutive ERA5 accumulation values (see NSE footnote).
SSHF	Surface Sensible Heat Flux	Units in Wm^{-2}. Rate at which energy at the surface is being used to induce convection and warming of the air mass above it. Instantaneous values are approximated by averaging consecutive ERA5 accumulation values (see NSE footnote).

(continued...)

[1]ERA5 parameters come in instantaneous and accumulation values. Instantaneous values are calculated for that point in time at each hour whereas accumulation values represent a sum compiled over the course of the previous hour window. NSE, SLHF and SSHF are accumulation values whereas the remainder are instantaneous. Averages for these variables were computed to approximate "instantaneous" values in order to allow an apples to apples comparison.

Abbreviation	Variable	Description
T2	Temperature at 2 m Above Surface	Units in K. This is one of the major factors affecting the partitioning of the atmospheric energy budget.
TCC	Total Cloud Cover	Dimensionless. Fraction of grid cell covered by cloud.
TCCLW	Total Column Cloud Liquid Water	Units in kgm^{-2}. Total cloud liquid content averaged over grid cell. Does not include rain water droplets.
TCWV	Total Column Water Vapour	Units in kgm^{-2}. Total amount of water vapour averaged over grid cell. Often referred to as precipitable water (PW).
U10	Zonal Component of 10 m Wind Velocity	Units in ms^{-1}. East-West component of wind velocity at 10 m above surface. Positive values indicate that wind has a westerly component (blowing *to* the east).
U100	Zonal Component of 10 m Wind Velocity	Units in ms^{-1}. East-West component of wind velocity at 100 m above surface. Positive values indicate that wind has a westerly component (blowing *to* the east).
V10	Meridional Component of 10 m Wind Velocity	Units in ms^{-1}. North-South component of wind velocity at 10 m above surface. Positive values indicate that wind has a southerly component (blowing *to* the north).

(continued…)

Abbreviation	Variable	Description
V100	Meridional Component of 100 m Wind Velocity	Units in ms^{-1}. North-South component of wind velocity at 100 m above surface. Positive values indicate that wind has a southerly component (blowing *to* the north).
VIDMF	Vertical Integral of Divergence of Moisture Flux	Units in $kgm^{-2}s^{-1}$. The average rate at which water vapour in a grid cell is leaving to neighbouring grid cells.[2] Positive values indicate water vapour is diverging (leaving grid cell) while negative values indicate water vapour is converging (entering grid cell).
VIEC	Vertical Integral of Energy Conversion	Units in Wm^{-2}. Rate at which energy is being converted from internal plus potential energy into kinetic energy.[3] Negative values indicate kinetic energy conversion into internal plus potential energy.
VIKE	Vertical Integral of Kinetic Energy	Units in Jm^{-2}. Total kinetic energy from the *horizontal* motion of air masses through the grid cell, averaged over the grid cell. This was used to study how land cover change affects partitioning in the atmospheric energy budget.

(continued…)

[2]Note that ERA5 has a similarly named parameter called **VIMF!** (**VIMF!**) which is an accumulation rather than instantaneous parameter, but with the crucial difference that "moisture" in this variable refers to the total of water vapour, cloud liquid and cloud ice. The ERA5 documentation for VIDMF also refers to "moisture" and it is not apparent that this actually uses a different definition where it only includes water vapour, but this was indeed confirmed to be the case via correspondence with ECMWF specialist support.

[3]By ERA5 definitions, internal energy refers to the microscopic energy of the air molecules excluding latent energy (this is treated as a separate part of the atmospheric energy budget) which may be different to definitions used in chemistry. Potential energy here refers to macroscopic gravitational potential energy (as opposed to internal air pressure within the grid cell, as this is implicitly accounted for within internal energy). Kinetic energy refers to kinetic energy from the *horizontal* motion of air masses.

Abbreviation	Variable	Description
VIPILE	Vertical Integral of Potential, Internal and Latent Energy	Units in Jm^{-2}. Total of gravitational potential energy, internal energy and latent energy (see footnote for VIEC). This constitutes the total atmospheric energy budget minus kinetic energy. This was used to study how land cover change affects partitioning in the atmospheric energy budget.
WS10	Wind Speed at 10 m Above Surface	Units in ms^{-1}. Scalar quantity for wind speed at 10 m above surface.
WS100	Wind Speed at 100 m Above Surface	Units in ms^{-1}. Scalar quantity for wind speed at 100 m above surface. This is the quantity most directly relevant for wind energy generation.
WV10	Wind Velocity at 10 m Above Surface	Units in ms^{-1}. Vector quantity for wind velocity at 10 m above surface.
WV100	Wind Velocity at 100 m Above Surface	Units in ms^{-1}. Vector quantity for wind velocity at 100 m above surface. This quantity is also directly relevant for wind energy generation and furthermore highlights how wind direction changes.
d{VAR}	Hourly Change in {VAR}	Units vary. Change in the value for each of the above ERA5 or ERA5-derived values, as compared with its value in the previous hour. This was used to study how the rate of change of a variable was correlated with land cover change.

(continued…)

Abbreviation	Variable	Description
C10	Weibull Scale Parameter for 10 m Wind Speed	Units in ms^{-1}. Scale parameter for the Weibull distribution fit to the wind speed at 10 m above surface. The empirical Weibull fit was obtained using the equations of (Justus et al., 1977).
C100	Weibull Scale Parameter for 100 m Wind Speed	Units in ms^{-1}. Scale parameter for the Weibull distribution fit to the wind speed at 100 m above surface. The empirical Weibull fit was obtained using the equations of (Justus et al., 1977).
EROE100	Expected Rate of 100 m Wind Speed Exceeding 42.5 m/s	Dimensionless. The *expected* rate for wind speed at 100 m exceeding 42.5 m/s, which in practice is the typical wind speed which wind turbines can last 10 mins in before failure (Chen et al., 2015, 2016; GE Energy, 2018). This is the *expected* rate calculated from the tail of the Weibull distribution fit rather than the actual observed rate of exceedance.
K10	Weibull Shape Parameter for 10 m Wind Speed	Dimensionless. Shape parameter for the Weibull distribution fit to the wind speed at 10 m above surface. The empirical Weibull fit was obtained using the equations of (Justus et al., 1977).
K100	Weibull Shape Parameter for 100 m Wind Speed	Dimensionless. Shape parameter for the Weibull distribution fit to the wind speed at 100 m above surface. The empirical Weibull fit was obtained using the equations of (Justus et al., 1977).
mean(WS10)	Mean of 10 m Wind Speed	Units in ms^{-1}. Mean of wind speed at 10 m above surface. This is roughly equivalent to the mean of the mean diurnal profile for Wind Speed at 10 m Above Surface (WS10) (see Section B.1.2).

(continued...)

Abbreviation	Variable	Description
mean(WS100)	Mean of 100 m Wind Speed	Units in ms^{-1}. Mean of wind speed at 10 m above surface. This is roughly equivalent to the mean of the mean diurnal profile for WS100 (see Section B.1.2).
std(WS10)	Standard Deviation of 10 m Wind Speed	Units in ms^{-1}. Standard deviation of wind speed at 10 m above surface. This is used with Weibull Shape Parameter for 10 m Wind Speed (K10) to analyse how the variability in wind speed changes along with land cover.
std(WS100)	Standard Deviation of 100 m Wind Speed	Units in ms^{-1}. Standard deviation of wind speed at 10 m above surface. This is used with Weibull Shape Parameter for 100 m Wind Speed (K100) to analyse how the variability in wind speed changes along with land cover.
TGCF100	Typical Gross Capacity Factor for 100 m Turbine	Dimensionless. Gross capacity factor which a typical 2.5 MW turbine with 100 m hub height would have had over the study period. This was computed by first averaging the power curves for similar 2.5 MW turbines from Vestas, Goldwind and GE Energy, then computing the energy generation for each hour in the study period using ERA5 data for the wind speed at 100 m above surface (see Section 3.5.4).

A.4 | Assimilation cycle artefacts in ERA5

A.4.1 | Artefacts in TCWV

The hourly mean results for Hourly Change in Total Column Water Vapour (dTCWV) at hours 0600 LT (2200 UTC) and 1800 LT (1000 UTC) indicate a discontinuous change in TCWV (not shown). These values represent the change in TCWV from 2100-2200 UTC and 0900-1000 UTC respectively. The humidity (and by extension TCWV) values in ERA5 are known to have a mismatch between the end of one assimilation cycle and the beginning of the next, which happen at exactly these time windows (ECMWF, 2022).

A.4.2 | Artefacts inherited by NAC

Because the NAC value at hour i is derived using the TCWV values at hours i-1 and i+1 (see Appendix B.2), the NAC value at hours 0500-0700 LT and 1700-1900 LT inherit these discontinuities (see Figure A.6). These discontinuities are not observed for any of the other variables which NAC is derived from (NSE and VIDMF).

A.4.3 | Results relatively unaffected

Figure A.6 shows how this leads to unusually large Hourly Change in Net Atmospheric Condensation (dNAC) means from 1700-1900 LT. But importantly, the increases at 1700 LT are offset by a spatially correlated decrease of comparable magnitude at 1900 LT. Analogous results were found between 0500-0700 LT (not shown). So the means computed over the course of this project should be relatively unaffected. This applies even for the diurnal comparison where means were computed over a subset of hours, since daytime and nighttime hours were defined as 0800-1500 LT and 2000-0300 LT respectively (see Section 3.3.1), which falls outside of the hours with artefacts. This does mean, however, that MDP statistics apart from the mean (hour of maximum, hour of minimum, maximum, minimum and range) need to be interpreted with care when it comes to TCWV, dTCWV, NAC and dNAC.

A.4.4 | Other affected variables

None of the other key study variables apart from FA were found to have similarly obvious assimilation cycle discontinuities, but FA was only used for one result (Figure 4.10) which was a mean over all hours of the day so results should still be relatively unaffected.

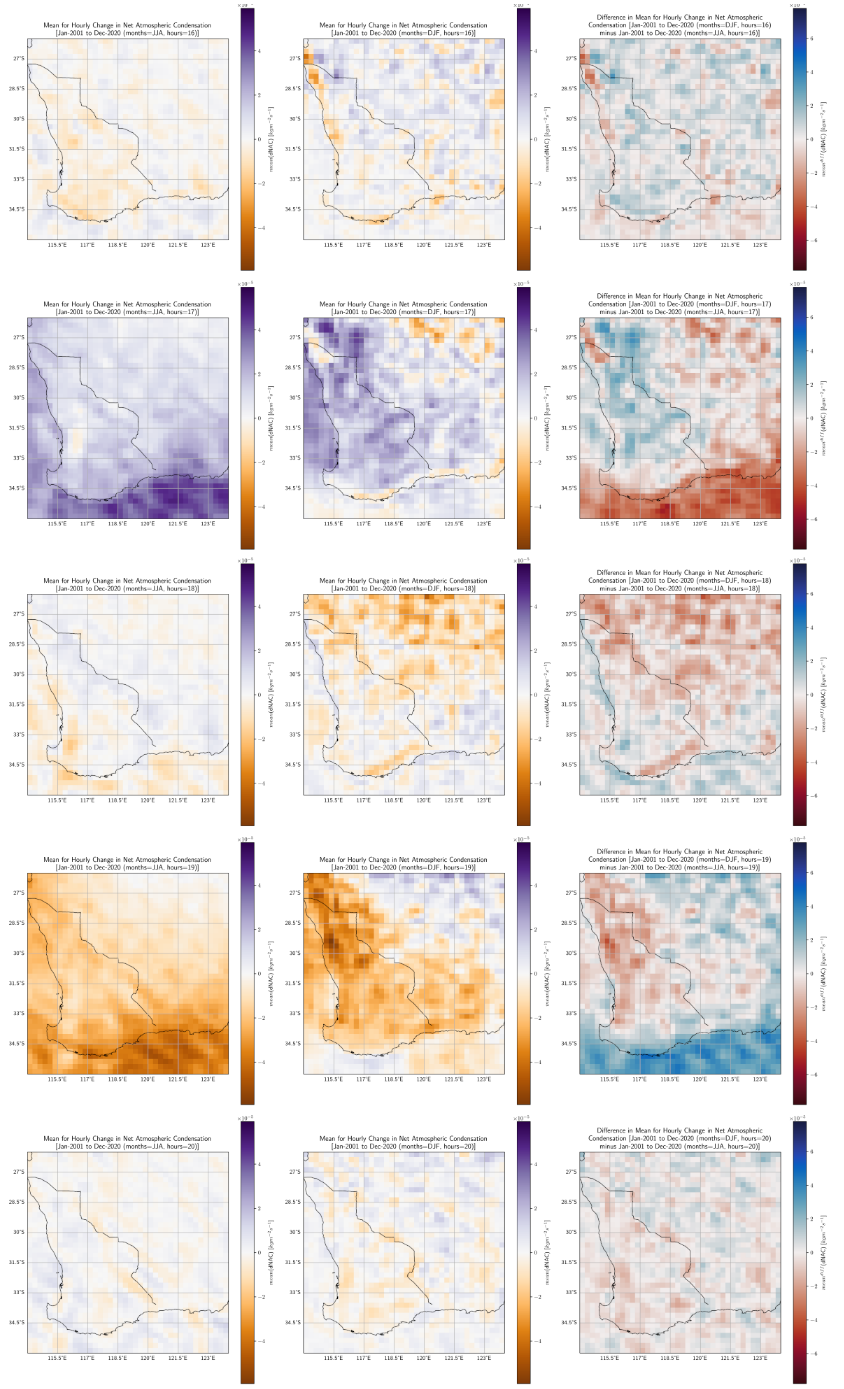

Figure A.6: 1600-2000 mean JJA and DJF values for dNAC. 1600 and 2000 means are in line with means in remaining hours. Artefacts inherited from TCWV assimilation cycles show opposite trends at 1700 and 1900.

A.5 | Other focus regions in original project scope

The original project scope included results for CA and NB but time did not allow for detailed analysis, discussion and presentation of these results. Included below is a summary for each of these regions, as well as the selected periods for the similar comparison. This may be used for future research.

A.5.1 | General

A.5.1.1 | Periods for diurnal and seasonal comparison

For all focus regions, the diurnal and seasonal comparisons were performed over the period from Jan-2001 to Dec-2020 (inclusive). The GLASS products derived from MODIS, the more advanced instrument, begin around Mar-2000, with the LAI dataset ending Dec-2021 while the FAPAR dataset ends Dec-2020 (at the time of writing). As averages starting from Mar-2000 and ending Dec-2020 would have skewed weightings for the months of January and February, we elected to use Jan-2001 as the period start instead.

A.5.1.2 | Wet and dry months

Based on historical precipitation climatology, we have selected the months representing the wet and dry seasons for each region as being:

- WA: June, July, August (JJA) and December, January, February (DJF) respectively
- CA: May to October (5-6-7-8-9-10) and November to April (1-2-3-4-11-12) respectively
- NB: January to June (1-2-3-4-5-6) and July to December (7-8-9-10-11-12)

A.5.1.3 | Daytime and nighttime hours

The local timezones for WA, CA and NB are UTC+8, UTC-6 and UTC-3 respectively[4]. Where comparisons between daytime and nighttime hours have been made, the average values for hours from 8 am to 3 pm local time[5] (8-9-10-11-12-13-14-15) have been selected as representative of daytime, while the average values for hours from 8 pm to 3 am local time (0-1-2-3-20-21-22-23) have been selected as representative of nighttime.

[4]The focus region for NB spans across 35 degrees of longitude, so it actually covers multiple local timezones and over more than 2 hours of local solar timezones (15 degrees per hour). We have selected UTC-3 here because this is close to the local solar timezone for the midpoint of this region.

[5]Unless otherwise stated, all times in this report are expressed in local time, and hour endpoints are inclusive.

A.5.1.4 | Orography

The orography for each focus region is displayed in Figure A.7.

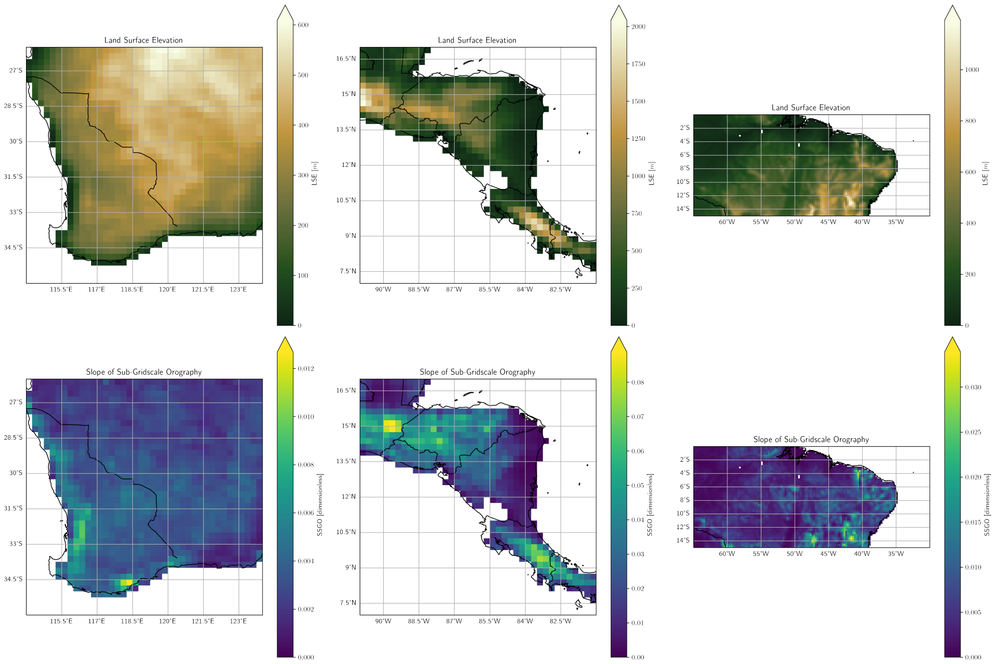

Figure A.7: Top row: Land Surface Elevation (LSE) for each region. Bottom row: Slope of Sub-Gridscale Orography (SSGO) for each region. From left to right: Western Australia, Central America, Northern Brazil.

A.5.2 | Central America

A.5.2.1 | Description of region

We selected the part of CA which runs (North to South) from El Salvador and Honduras to Nicaragua to Costa Rica (91°W to 81°W longitude and 17°S to 7°S latitude; see Figure A.8) because there existed spatially opposing trends in vegetation change. These countries had historically comparable rates of deforestation, but Costa Rica shifted towards reforestation due to policy changes in the 1990s whereas deforestation has continued in Honduras and Nicaragua. The western coastlines for El Salvador, Nicaragua and Costa Rica (where agriculture is concentrated) also have comparable cardinal orientations.

Being located near the equator, annual temperature variation at these locations are relatively minor. This is useful because it provides a comparison where one of the main variables affecting wind flow is relatively controlled for. Furthermore, the entire focus

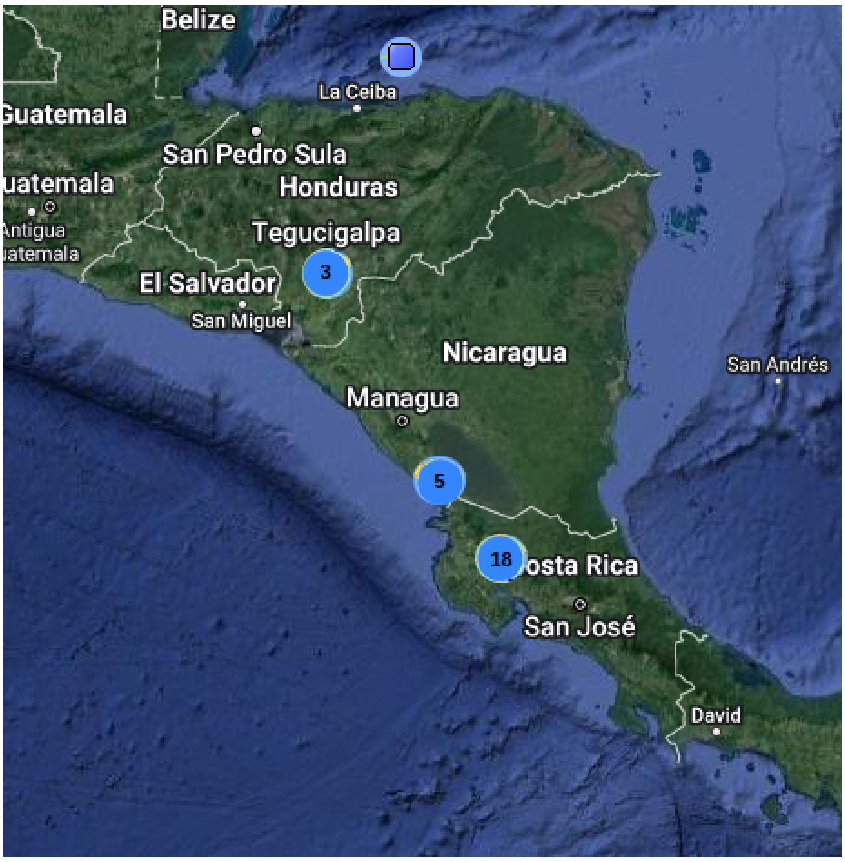

Figure A.8: Satellite image displaying Central America focus region from 91°W to 81°W longitude and 17°S to 7°S latitude (Google Maps, 2022a). Markers indicating positions and number of wind farms have been edited on using data from (The Wind Power, 2022b,e,f).

region is on the order of 1000 km, so synoptic weather features (which have a characteristic scale of this order) are less likely to produce contrasting effects over the different subregions.

A.5.2.2 | Significance of results from this region

Wind farms are concentrated on agricultural land along the western coast where there are plans for continued development. But as in the case of WA, the value of this focus region isn't necessarily in its direct implications for existing wind farms in the area, but in that it may yield some insights into the principles between land cover change and surface winds, which may then have broader implications for wind energy generation in general.

A.5.2.3 | Study periods

Selected periods For CA, the selected periods for the similar comparison was from Jan-2002 to Dec-2006 and from Jan-2014 to Dec-2018 (see Figure A.9).

Very similar values and trends in climate indices The pair of Jan-2002 to Dec-2006 and Jan-2014 to Dec-2018 was deemed most appropriate since these periods had comparable averages in relevant climate indices and appear to span across the same phase of the relevant atmospheric oscillations. This was true for all of the relevant indices: AMOI, PDOI, ONI (for ENSO), and the EPOI. The AOI and NAOI over these periods (not shown) also appeared to span across the same phase but had 5-year averages with slightly higher disparities (but these disparities were nevertheless small in terms of the characteristic size of the oscillations). The DMI and the AAOI (not shown) over these periods, on the other hand, were considerably different, but these were assumed not to be a major factor due to the distance of the Indian Ocean and Antarctica from the Americas[6].

Summary of ENSO events The similarity between these periods is particularly remarkable because even the monthly values and 5-year averages for the ONI (which has irregular oscillations) display a similar time evolution pattern. Both periods begin with the conclusion of an El Nino event and end past halfway into an La Nina event, and fully covers another La Nina event in between. The period from Jan-2014 to Dec-2018 contains an additional El Nino event not found in the period from Jan-2002 to Dec-2006 but this appears to mostly be a technicality with the definition of an El Nino event. A look at the monthly values reveals a spike in the ONI which could have qualified as an El Nino event under slightly relaxed definitions. Furthermore, the monthly values between the starting El Nino event and ending La Nina event are almost mirror images of each other.

Time difference between periods well suited for studying land cover change In the case of Costa Rica, although remote sensing indicates that the rate of forest cover increase here was highest during the 1990s, leaf area index data derived from the Advanced Very High Resolution Radiometer (AVHRR) instrument (not shown) for this region showed considerable noise and disagreement with MODIS (the more advanced instrument). Given these factors, this set of study periods was also desirable because it was

[6]Significant effects due to teleconnections are theoretically possible but we have assumed this isn't the case here

Figure A.9: NOAA climate indices for climate drivers in CA. Green shading highlights selected periods. Blue and red shading highlight La Nina and El Nino events respectively.

completely contained within the MODIS coverage period. In addition to this, a land cover classification study by Marx et al. (2017) using Landsat and Unmanned Aerial Vehicle (UAV) data in lowland Costa Rica suggested an 11-year period for a pasture to transition into secondary forest, so a 13 year difference between selected periods corresponds well with our goals for studying the effects of LCC. The change in MLAI between these periods is displayed in Figure A.10.

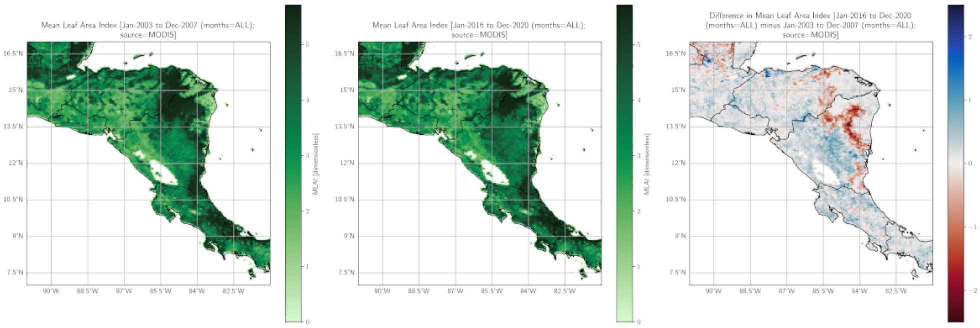

Figure A.10: MLAI computed over each period in the similar comparison (left and middle), as well as the difference in these values between the two periods (right).

A.5.2.4 | Land use and land cover change

Figure A.11 displays trends in Land Use and Land Cover Change (LULCC) at around the time of period 1 in the similar comparison.

A.5.3 | Northern Brazil

A.5.3.1 | Description of region

We selected the North to Northeast regions of Brazil (65°W to 30°W longitude and 15°S to 0°S latitude; see Figure A.12) because there has been extensive deforestation over this area and it was believed that effects resulting from LCC here were likely to be especially pronounced. The change in MLAI between these periods is displayed in Figure A.13.

A.5.3.2 | Significance of results from this region

Several studies have identified large-scale changes in precipitation and moisture convergence patterns, which indirectly implicate surface wind changes. Effects here are

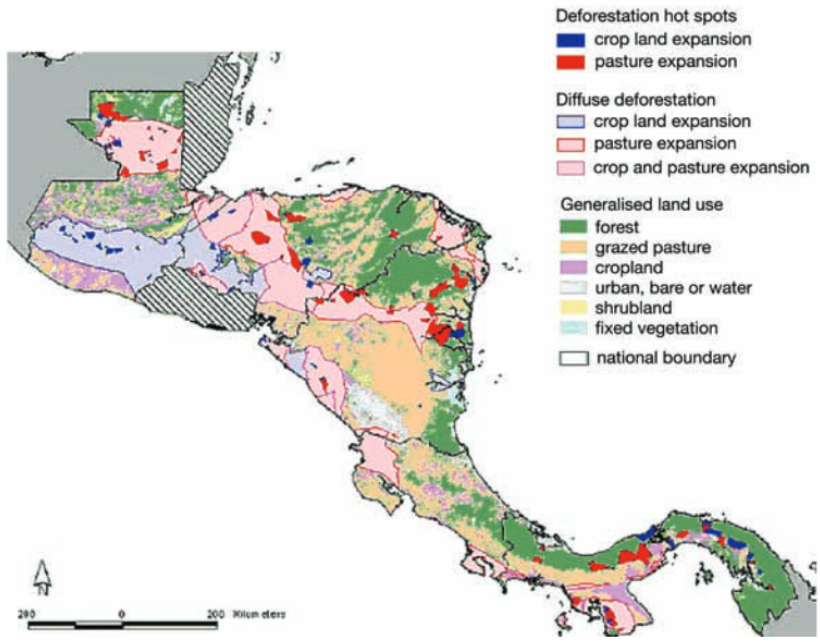

Figure A.11: Land usage and land cover change in Central America (IPCC, 2007).

Figure A.12: Satellite image displaying Northern Brazil focus region from 65°W to 30°W longitude and 15°S to 0°S latitude (Google Maps, 2022b). Markers indicating positions and number of wind farms have been edited on using data from (The Wind Power, 2022a).

likely to have immediate implications for energy generation due to the number of wind farms in this region (both existing and in the development pipeline[7]).

[7]Up to 60 GW of offshore wind near the northeastern coast is in the early planning stage (4C Offshore, 2022).

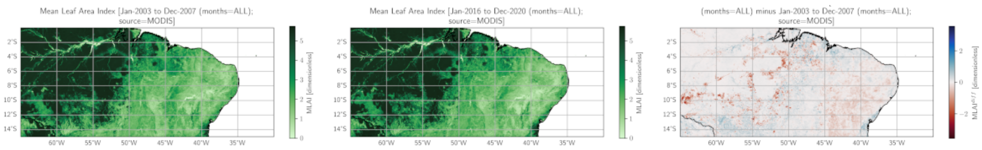

Figure A.13: MLAI computed over each period in the similar comparison (left and middle), as well as the difference in these values between the two periods (right).

A.5.3.3 | Study periods

For NB, the selected periods for the similar comparison was from Jan-2002 to Dec-2006 and from Jan-2014 to Dec-2018 (for the same reasons highlighted in Section A.5.2.3 for CA.

A.5.3.4 | Land use and land cover change

Figure A.14 displays trends in LULCC at around the time of period 1 in the similar comparison.

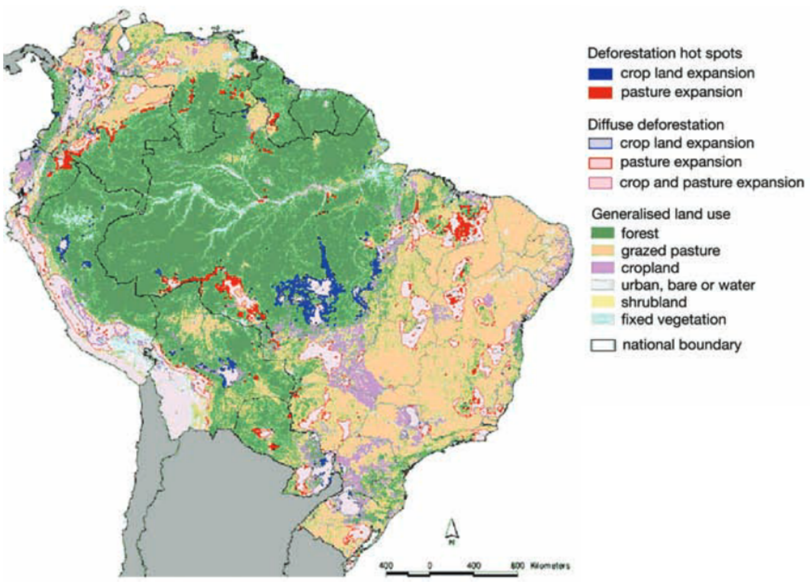

Figure A.14: Land usage and land cover change in Northern South America (IPCC, 2007).

B

Theory and derivations

B.1 | Commutativity of statistical operations

B.1.1 | Mean of monthly averaged by hour of day values is approximately equal to mean of hourly values

Let $x_d^m(i)$ be the value of a variable at hour i on the dth day of the mth month in the dataset we are computing over, n_{months} the number of months we are computing over, and n_{days}^m the number of days for the mth month in the dataset. Then:

$$\begin{aligned}
&\text{Mean of monthly averaged by hour of day values for hour i} \\
&= \frac{1}{n_{months}} \sum_{m=1}^{n_{months}} \frac{1}{n_{days}^m} \sum_{d=1}^{n_{days}^m} x_d^m(i) \\
&= \sum_{m=1}^{n_{months}} (n_{months} n_{days}^m)^{-1} \sum_{d=1}^{n_{days}^m} x_d^m(i)
\end{aligned} \tag{B.1}$$

$$\begin{aligned}
&\text{Mean of hourly values at hour i} \\
&= \left(\sum_{j=1}^{n_{months}} n_{days}^j \right)^{-1} \sum_{m=1}^{n_{months}} \sum_{d=1}^{n_{days}^m} x_d^m(i) \\
&= \sum_{m=1}^{n_{months}} \left(\sum_{j=1}^{n_{months}} n_{days}^j \right)^{-1} \sum_{d=1}^{n_{days}^m} x_d^m(i)
\end{aligned} \tag{B.2}$$

So the mean of monthly averaged by hour of day values is equal to the mean of hourly values if $n_{months} n_{days}^m = \sum_{j=1}^{n_{months}} n_{days}^j$. This occurs if n_{days}^m is a constant. This condition is not satisfied in general since the number of days in different months varies from 28 to 31. However, this is a small difference, especially when summation is conducted over long periods. Thus we conclude that the mean of monthly averaged by hour of day values is *approximately* equal to the mean of hourly values, and we are justified in computing the mean diurnal profile using monthly averaged by hour of day data (which requires significantly less computer storage and memory).

B.1.2 | MDP mean is approximately equal to mean of all hourly data values

Let $x_d^m(i)$ be the value of a variable at hour i on the dth day of the mth month in the dataset we are computing over, n_{months} the number of months we are computing over, and n_{days}^m the number of days for the mth month in the dataset. Then:

$$\begin{aligned}
\text{MDP mean} &= \frac{1}{n_{months}} \sum_{m=1}^{n_{months}} \frac{1}{n_{days}^m} \sum_{d=1}^{n_{days}^m} \frac{1}{24} \sum_{i=1}^{24} x_d^m(i) && \text{(B.3)} \\
&= \frac{1}{24} \sum_{m=1}^{n_{months}} (n_{months} n_{days}^m)^{-1} \sum_{d=1}^{n_{days}^m} x_d^m(i) \\
\text{Mean of all hourly data values} &= \left(24 \sum_{j=1}^{n_{months}} n_{days}^j \right)^{-1} \sum_{m=1}^{n_{months}} \sum_{d=1}^{n_{days}^m} \sum_{i=1}^{24} x_d^m(i) && \text{(B.4)} \\
&= \frac{1}{24} \sum_{m=1}^{n_{months}} \left(\sum_{j=1}^{n_{months}} n_{days}^j \right)^{-1} \sum_{d=1}^{n_{days}^m} \sum_{i=1}^{24} x_d^m(i)
\end{aligned}$$

So we conclude that the MDP mean of a variable is *approximately* equal to the mean of all hourly data values, and interpret it as such in our results.

B.1.3 | Mean of hourly changes is equal to hourly change in mean values

Let x_j^i be the value of a variable at hour i for the jth instance in the dataset we are computing over, n the number of instances we are computing over, and $mean_j$ the mean computed over all instances of a variable, whether compiled over a month, an entire dataset, or other. Then:

$$\begin{aligned}
mean_j(x_j^i - x_j^{i-1}) &= \frac{1}{n} \sum_{j=1}^{n} (x_j^i - x_j^{i-1}) && \text{(B.5)} \\
&= \frac{1}{n} \sum_{j=1}^{n} x_j^i - \frac{1}{n} \sum_{j=1}^{n} x_j^{i-1} \\
&= mean_j(x_j^i) - mean_j(x_j^{i-1})
\end{aligned}$$

So we can interpret the MDP, hourly means and monthly means for the hourly change as the hourly change in MDP, hourly means and monthly means respectively.

B.1.4 | Maximum and minimum of means does not necessarily equal to mean of maxima and minima

Let x_d^i be the value of a variable at hour i for the dth day in the dataset we are computing over, n_{days} the number of days we are computing over, and $mean_d$ the mean computed over all day instances of a variable, whether compiled over a month, an entire dataset, or other. Then:

$$max\left(\left\{mean_d(x_d^i) : i \in \mathbb{Z} \cap [1,24]\right\}\right) \leq mean_d\left(max(\{x_d^i : d \in \mathbb{Z} \cap [1,24])\}\right) \tag{B.6}$$

$$min\left(\left\{mean_d(x_d^i) : i \in \mathbb{Z} \cap [1,24]\right\}\right) \geq mean_d\left(min(\{x_d^i : d \in \mathbb{Z} \cap [1,24])\}\right) \tag{B.7}$$

MDP maxima and minima correspond to the LHS of these equations and need to be interpreted as such. They do not necessarily describe the maxima and minima of days considered individually.

B.1.5 | Magnitude of mean vector does not necessarily equal to mean of vector magnitudes

Let $\vec{v}_j^i$ be a vector quantity at hour i for the jth instance in the dataset we are computing over, and n the number of instances we are computing over. Using the triangle inequality, we have:

$$\begin{aligned} \text{Magnitude of mean vector at hour i} &= \left|\frac{1}{n}\sum_{j=1}^{n}\vec{v}_j^i\right| \\ &\leq \frac{1}{n}\sum_{j=1}^{n}|\vec{v}_j^i| \\ &= \text{Mean of vector magnitudes at hour i} \end{aligned} \tag{B.8}$$

Thus the magnitude of mean vector is less than or equal to the mean of vector magnitudes, and this is why an exception was made for wind speed summary statistics in our analysis (these were computed using instantaneous hourly values from zonal and meridional components rather than monthly averaged by hour of day values). This result also implies that the magnitude of wind velocity summary statistics will not necessarily coincide with wind speed summary statistics.

B.1.6 | Gross capacity factor from mean power curve is equal to mean of gross capacity factors from each power curve

Let $WS100_j^i$ be the 100 m wind speed at hour i for the jth instance in the dataset we are computing over, n the number of instances we are computing over, and P_k the power curve of the kth turbine. The gross capacity factor is given by the average power generated divided by the nameplate power rating $P_{nameplate}$, so:

$$\begin{aligned} &\text{Gross capacity factor from mean power curve} \\ &= \frac{\frac{1}{24n}\sum_{i=1}^{24}\sum_{j=1}^{n}\left[\frac{1}{3}\sum_{k=1}^{3}P_k(WS100_j^i)\right]}{P_{nameplate}} \\ &= \frac{1}{3}\sum_{k=1}^{3}\left[\frac{\frac{1}{24n}\sum_{i=1}^{24}\sum_{j=1}^{n}P_k(WS100_j^i)}{P_{nameplate}}\right] \\ &= \text{Mean of gross capacity factors from each power curve} \end{aligned} \tag{B.9}$$

B.2 | Derivation for net atmospheric condensation

B.2.1 | Water vapour continuity

B.2.1.1 | Factors affecting water vapour in a grid cell

Here we derive the formula used for NAC (Eq 3.1). The TCWV in a grid cell will change under the following scenarios:

1. The balance between evaporation and condensation in the atmosphere.
2. The balance between evaporation and condensation on the Earth's surface.
3. The balance between convergence and divergence of water vapour (i.e. movement of water vapour into the grid cell from neighbouring grid cells or vice versa).
4. The balance between sublimation (change of state from solid to gas) and deposition (change of state from gas to solid).
5. The balance between water vapour products and water vapour reactants for chemical reactions occurring within the grid cell.

We will assume that the effects of sublimation/deposition and chemical reactions are negligible in comparison to evaporation/condensation and water vapour movement.

B.2.1.2 | Continuity equation for gridded data

Positive NSE constitutes a positive rate of TCWV increase (i.e. there is an increased concentration of water vapour in that grid cell since liquid water is evaporating into water vapour), while positive NAC and positive VIDMF[1] constitutes a negative rate of TCWV increase (i.e. TCWV is decreasing because water vapour is condensing out into liquid droplets or is diverging/leaving the grid cell). So we have:

$$\begin{aligned} \frac{d}{dt}(TCWV\ [kgm^{-2}]) &= -NAC\ [kgm^{-2}s^{-1}] + NSE\ [kgm^{-2}s^{-1}] \\ &\quad -VIDMF\ [kgm^{-2}s^{-1}] \end{aligned} \tag{B.10}$$

$$\begin{aligned} NAC\ [kgm^{-2}s^{-1}] &= NSE\ [kgm^{-2}s^{-1}] - VIDMF\ [kgm^{-2}s^{-1}] \\ &\quad -\frac{d}{dt}(TCWV\ [kgm^{-2}]) \end{aligned} \tag{B.11}$$

B.2.2 | Approximating NAC using hourly data values

B.2.2.1 | Continuity equation in discrete form

Using an approximation for NSE and $\frac{d}{dt}(TCWV)$, the equation used to obtain the jth instance of NAC at hour i from raw ERA5 data is then:

$$\begin{aligned} NAC_j^i\ [kgm^{-2}s^{-1}] &= -\frac{1000\ kgm^{-2}}{1\ m \text{ of water}}\frac{(NSE_j^i + NSE_j^{i-1})\ [m \text{ of water}]}{2\times 3600\ s} \\ &\quad -VIDMF_j^i\ [kgm^{-2}s^{-1}] - \frac{(TCWV_j^{i+1} - TCWV_j^{i-1})\ [kgm^{-2}]}{2\times 3600\ s} \end{aligned} \tag{B.12}$$

B.2.2.2 | Approximation for NSE

The raw ERA5 data for NSE is specified in units of m of water equivalent, with net evaporation being negative, and is an *accumulation* parameter that ends at the specified hour (i.e. NSE_j^i corresponds to the total *amount* of net surface evaporation over the hour window beginning at hour i-1 and ending at hour i). To approximate the instantaneous *rate* of net surface evaporation at hour i, we thus average over accumulated net surface evaporation in the hour windows leading up to and immediately after hour i (this corresponds to NSE_j^i and NSE_j^{i+1} respectively). As this is an average over two periods each of 1 hour length, we divide by $2 \times 3600\ s$ to obtain the *rate*. We also introduce a negative sign in front of the NSE term because we are defining positive NSE to mean net evaporation in contrast to the raw ERA5 data definitions. Finally, liquid water has

[1]Moisture refers to water vapour only per ERA5 definition for this variable.

a density of approximately 1000 kgm^{-3} so 1 m of water is equivalent to an areal density of 1000 kgm^{-2}.

B.2.2.3 | Approximation for rate of change in TCWV

The raw ERA5 data for TCWV is an *instantaneous* parameter for the specified hour (i.e. $TCWV_j^i$ models the actual column water vapour at the instant of hour i). To then approximate the instantaneous *rate of change* for TCWV at hour i, we use the average rate of change between the instances at hour i-1 and hour i+1 (the values at these hours correspond to $TCWV_j^{i-1}$ and $TCWV_j^{i+1}$ respectively). As the period of time between hour i-1 and hour i+1 is 2 hours, we again divide by $2 \times 3600\ s$ in obtaining the rate.

B.2.3 | Approximation carries over to mean values

By linearity of the mean function, we obtain from Eq B.12:

$$\begin{aligned} mean_j(NAC_j^i)\ [kgm^{-2}s^{-1}] = \\ -\frac{1000\ kgm^{-2}}{1\ m \text{ of water}} \frac{\{mean_j(NSE_j^i) + mean_j(NSE_j^{i-1})\}\ [m \text{ of water}]}{2 \times 3600\ s} \\ -mean_j(VIDMF_j^i)\ [kgm^{-2}s^{-1}] \\ -\frac{\{mean_j(TCWV_j^{i+1}) - mean_j(TCWV_j^{i-1})\}\ [kgm^{-2}]}{2 \times 3600\ s} \end{aligned} \tag{B.13}$$

where $mean_j$ is the mean computed over all instances of a variable, whether compiled over a month, an entire dataset, or other. Thus Eqn B.13 can be used to construct the summary statistics for NAC regardless of whether hourly data or monthly averaged by hour of day data is being used.

B.2.4 | NAC as a hybrid parameter

Note that NAC is neither an instantaneous or accumulation parameter. It is a hybrid value derived from the average of two accumulations (NSE), an instantaneous value (VIDMF) and a mean rate of change using two instantaneous values (TCWV) as endpoints. These methods mean that maxima and minima for NSE may be underestimated and overestimated respectively, while the most positive and most negative rate of change in TCWV may be underestimated and overestimated respectively. To the extent that hours for the maxima and minima for NSE coincide with the most positive and negative rate of change in TCWV respectively (which is possible, given that net evaporation contributes to TCWV increase), these biases in NAC may cancel each other out (since NSE has a positive coefficient on the RHS of Eq B.11 while TCWV a negative), but this will not always be the case.

B.3 | Heuristical argument for anistropy of condensation-induced airflow

B.3.1 | Three layer model of troposphere

- Under hydrostatic equilibrium air pressure decreases with altitude. We can roughly divide up the troposphere into 3 layers: the high pressure region at the surface, a medium pressure region where the clouds will form (conceptually described later), and a low pressure region above this.

- Localised parcels of air within a region will have different temperatures and relative humidities, and hence different LCLs. As there are many such air parcels, we can conceptually identify the "region where clouds will form" with a band of heights which the LCLs (bar outliers) span across (in a similar vein to how the discrete energy levels of atoms in close proximity bunch up together to form energy bands) (Green, 1998).

B.3.2 | Net forces on particles at interfaces

- Upon condensation there is a drop in pressure such that the middle of the 3 layers is now the one with the lowest pressure. Particles at the first interface (counting from the surface up) will then have a pressure gradient force upwards with magnitude which exceeds that of the gravitational force (they were previously equal when in hydrostatic equilibrium). Meanwhile, the pressure gradient force at the second interface reverses direction and is now compounding upon the downwards effect of gravity.

- The ensuing circulation is such that air from the surface is directed upwards and accelerates through the first interface, then decelerates and spreads outwards as it penetrates through the second interface. As the fluid enters motion, this subsequently changes the Eulerian pressure field such that the surface layer now has a low pressure relative to the top layer (because air decelerates and accumulates here), while the middle layer where atmospheric condensation occurs continues to have the lowest pressure. At this point there becomes less of a contrast between the forces at each interface (and so the effects of condensation are less anisotropic) but the forces nevertheless remain favourable to the circulation pattern of surface air accelerating upward through the first interface then decelerating and spreading outwards while penetrating through the second interface.

B.3.3 | Electrical circuit with battery analogy

- The final configuration is conceptually similar to the way electrical circuits work if we identify the top layer with the outgoing leg of conventional current from a battery, the middle layer with the battery itself, and the surface layer with the return leg of conventional current. In the circuit / atmosphere there will be low electric potential (potential energy per unit charge) / air pressure (potential energy per unit volume) in the surface layer, a negative electric potential difference / pressure difference across the middle layer (going from the first interface to the second interface)[2] which is sustained by chemical / latent energy, and high electric potential / air pressure in the top layer.

- And in the same way that batteries connect together two material of different electrochemical potential (potential energy per unit mole) so that one end more readily emits electrons and the other accepts (giving rise to anisotropic electron flow), atmospheric condensation under gravity produces two (abstract) interfaces subject to different net forces per unit area (equivalent to pressure and potential energy per unit volume) so that one end more readily expels air (downwards) and the other accepts (upwards).

B.3.4 | Electrical circuit with solar cell analogy

B.3.4.1 | Pressure chamber with selective resistivities at interfaces

- Another way to view this is that particles in the middle layer will have a tendency to spread outwards due to internal pressure within this layer, but this motion is either supported or inhibited by the pressure balances (net of gravitational and pressure-gradient forces per unit area) at each interface. This is conceptually similar to how the buildup of electron and hole pressures in a solar cell upon incident radiation are supported or inhibited by the selective membranes at each contact (which have different electron and hole conductivities) (Wurfel and Wurfel, 2016).

[2] By Kirchoff's voltage law, potential difference across the battery must be negative if potential difference over the remainder of the circuit is positive.

B.3.4.2 | Symmetry between electromagnetic and pressure fields

- Note that these circuit analogies might not be merely superficial similarities. Theoretical work by Fedosin (2015) suggests that there is a fundamental symmetry embodied within the equations for electromagnetic and pressure fields. The pressure field equations are (Fedosin, 2015)

$$\nabla_\nu f^{\mu\nu} = \frac{-4\pi\sigma}{c^2} J^\mu = -4\pi\sigma\epsilon_0\mu_0 J^\mu \tag{B.14}$$

$$\nabla_\sigma f_{\mu\nu} + \nabla_\mu f_{\nu\sigma} + \nabla_\nu f_{\sigma\mu} = 0 \tag{B.15}$$

while the electromagnetic field equations are[3]

$$\nabla_\nu F^{\mu\nu} = -\mu_0 j^\mu \tag{B.16}$$

$$\nabla_\sigma F_{\mu\nu} + \nabla_\mu F_{\nu\sigma} + \nabla_\nu F_{\sigma\mu} = 0 \tag{B.17}$$

(in covariant form using Einstein notation). $f_{\mu\nu}$ is the pressure field tensor, $F_{\mu\nu}$ is the electromagnetic tensor, ϵ_0 is the permittivity of free space, μ_0 is the permeability of free space, ϵ_0 is the permittivity of free space, c is the speed of light, σ is the pressure field constant, $J^\mu = \rho_0 u^\mu$ is the mass four-current, and $j^\mu = \rho_{0q} u^\mu$ is the charge four-current, where ρ_0 is the mass density of matter in the comoving reference frame, ρ_{0q} is the charge density in the comoving reference frame, and u^μ is the four-velocity.

B.3.4.3 | Discretising volume of atmospheric circulation

- Given the symmetry between charge and mass density in these equations, we can further extend the electrical circuit analogy and make the similarities even more apparent by examining the circuit in terms of electric potential multiplied by charge density: this quantity represents potential energy per unit volume of the charges and is analogous to pressure (potential energy per unit volume of the masses). Furthermore, we will use a solar cell rather than battery in the circuit (with positive terminal at the second interface and negative terminal at the first interface). In addition to this, we will conceptualise the atmospheric circulation as discrete localised volumes with fluxes of gas quanta (localised addition of mass density; analogous to localised addition of conventional charge density for hole fluxes) and vacuum quanta (localised removal of mass density; analogous to localised removal of conventional charge density / negative charge for

[3] Note that these equations are usually expressed with positive coefficient on the RHS. The negative coefficient arises here due to use of the column rather than row index for the nabla operator and the fact that the electromagnetic tensor is antisymmetric.

electron fluxes). Because we will be describing conventional charge which is positive, a downwards / upwards flux of electrons will correspond to an upwards / downwards flux of conventional charge density *removal*. The analogue to a downwards / upwards flux of electrons will thus be an upwards / downwards flux of vacuum quanta, while an upwards / downwards flux of holes corresponds to a downwards / upwards flux of gas quanta.

- Within the middle semiconductor / cloud layer of the electrical circuit / atmospheric circulation, there is ongoing electron-hole / vacuum-gas generation and recombination, and these quantas migrate to the two interfaces under the building internal pressure of the layer (as the volume of the middle layer is fixed by definition, a corollary to this is increasing potential energy stored within this layer). The first interface has a relatively high electron conductivity / vacuum quanta permeability while the second interface has a relatively high hole conductivity / gas quanta permeability. The result is an anisotropic flow whereby there is a net upwards flux of conventional charge / mass at both interfaces (i.e. conventional current / wind is flowing upwards at these interfaces). A corollary to this is a downward flux of electrons / vacuum quanta at both interfaces, and no remarkable comments about hole/gas fluxes because these are theoretical constructs which are valid only within the middle semiconductor / cloud layer (not valid within the wider circuit / circulation).

B.3.4.4 | Flow driven by potential energy buildup in pressure chamber

- Within the circuit / circulation, there will be a relatively high potential energy per unit volume above the second interface, and a relatively low potential energy per unit volume below the first interface. For the flow to be sustained, there needs to be external light / latent energy input for the generation of electron-hole / vacuum-gas pairs as it is the pressure buildup from these pairs within the middle layer which drives the flow. That is, energy for the flow *outside of the middle layer* derives from the potential energy *within the middle layer*, and this potential energy must in turn derive from conversion of energy sources external to this layer. In both cases, these energy sources are instantaneously realised within the middle layer since photons (light energy) will either be absorbed in whole or rejected in whole by electrons, while moisture (latent energy) will instantaneously undergo condensation and leave a vacuum quanta by construction of the model (the middle layer was defined as the region where condensation will occur).

- Note that there is an asymmetry in this treatment because a corollary to external latent energy input is a mass flux (in the form of water vapour), which does not exist in the case of external light energy input. Water vapour which is within the circulation may condense out and to the extent that it drops out of the circulation and onto the surface, there is a loss of mass as the droplets become external to the system. This in turn will mean a reduced air density. Conversely, for external sources of moisture input (eg. if precipitated droplets re-enter the system due to evaporation, or there is moisture advection into the system from afar), mass enters the system and so air density is increased (we are assuming a fixed volume defining the circulation). We have assumed in our treatment that these effects are minor and do not change our conclusions regarding anisotropic air flow. Of course, this treatment in itself is not enough to suggest that real-life atmospheric circulations represent a good approximation to the conditions assumed (both tacit and explicit; with respect to the conclusions regarding anisotropic air flow), and even then questions remain regarding whether such effects will be significant.

B.3.5 | Height of condensation

- Also, unlike electric potential in the circuit which was independent of height, our treatment of atmospheric circulation tacitly incorporated the effect of height: we were examining pressure divided by density using the net of gravitational and pressure-gradient forces, and the former force does depend on height. So also crucial (for anisotropy of condensation-induced airflow) is that atmospheric condensation is occurring at the appropriate height: not so low that the anisotropy is biased downwards, and not so high that the resulting circulation stalls (a heuristical argument using the previous 3 layer model follows below).

- If condensation happened at the surface rather than middle layer, then upon initial disturbance from hydrostatic equilibrium, the surface layer will become the one with lowest pressure, while the middle and top layers will have a medium and low pressure respectively (as remains from the initial equilibrium due to the relatively short time scale for condensation). Both the pressure gradient and gravitational forces for particles at the first interface will be directed downwards so that air flows downwards. Meanwhile, at the second interface, the downwards gravitational force will have greater magnitude than the upwards pressure-gradient force (this is because the middle region will simultaneously be decreasing in pressure as air at the first interface flows downwards, in the process weakening the pressure-gradient force at the first interface from what was initially a hydrostatic equilibrium). The ensuing fluid circulation will cause the surface layer to have medium pressure (as the effects of condensation and airflow into this layer from above partially counteract each other), but the forces on particles at each interface will still be downwards and so the downward anisotropic bias persists.

- If condensation happened at the top layer instead, then upon initial disturbance of the hydrostatic equilibrium, the top layer will have especially low pressure, while the middle and surface layers will initially still have the medium and high pressures respectively from the initial equilibrium. This is initially conducive for upwards air flow through both the first and second interfaces. But as the fluid is set in motion, the top layer increases in pressure (as air from both the surface and middle layers is sent here) and partially offsets the effect of condensation, resulting in a medium amount of pressure. The middle layer likely retains a medium pressure as air is simultaneously being fed into (from below) and drained (from above) this layer. The surface layer also ends up with a medium pressure as air is initially directed upwards. The result is a weak pressure gradient force but the omnipresent gravitational force at each interface (which goes against the initially induced upwards air motion). Thus the circulation is likely to stall.

C

Codebook and reproducibility

All code created in the course of this project is available at `https://github.com/anthonylst6/thesis`. Programs created for automating analysis of an arbitrary ERA5 variable (in terms of mean diurnal profile statistics, hourly means and monthly means) were envisioned for general usage and as such, most of the functions within each script have been documented using Python docstrings, and permission to use these programs are granted subject to MIT License conditions.

C.1 | High-level description of functions

- The functions created in the course of this thesis allow comparison for the Mean Leaf Area Index (MLAI) and Mean Fraction of Photosynthetically Absorbed Radiation (MFAPAR) between two arbitrary periods (so long as they are within the range of available data from 1981-2021). And the comparison can further be done in terms of a subset of months from each period. So it is possible, for example, to compare the MLAI over the months of January, March and December between 1990-2000 with the MLAI over the months of July and November between 2005-2007. These variables derive from the GLASS dataset.

- These functions also allow comparison for various ERA5 variables between two arbitrary periods in terms of each variable's diurnal profile (can choose subset of months), mean (can choose subset of both months and hours), hourly means for each hour of the day (can choose subset of months), and monthly means for each month of the day (can choose subset of hours).

- For wind speed, there is also a separate function to compute the mean, standard deviation, Weibull distribution parameters resulting from an empirical fit, and other.

- The main data processing functions are contained in the `calc_funcs.py` script in the `scripts` folder.

- The `plot_funcs.py` script in the `scripts` folder is a plotting layer on top of `calc_funcs.py` and contains all the functions for creating comparison plots.

- Most analysis can be done purely using the `plot_funcs.py` script since this was built to automatically invoke any processing functions from `calc_funcs.py` if the processed data file does not already exist.

- The entire code is built around carefully selected names for each file, so it is not recommended to rename any of these files as this may break the code.

- There is a vast array of functions within these scripts but we will describe here only the high-level comparison plot functions. For detail into the other functions, look into the docstrings embedded within each script. At the time of writing, `calc_funcs.py` is fully documented while only the high-level comparison plot functions in `plot_funcs.py` have been documented.

- The high-level comparison plot functions in `plot_funcs.py` are:

  - `plot_comp_mdp_clim_stats_given_var_or_dvar`
  - `plot_comp_means_given_layer_and_type`
  - `plot_comp_hourly_means_given_var_or_dvar`
  - `plot_comp_monthly_means_given_var_or_dvar`
  - `plot_comp_wsd_clim`

- Each of these functions creates an output plot with 3 columns and 8 rows. The left column corresponds to the statistical summaries for the first period of study. The middle column is the same but for the second period. The right column is the difference between periods in the values for each statistical summary (calculated as second period minus first period). For reference, the first two rows will always display MLAI and MFAPAR. The colourbars are automatically standardised to allow fair comparison between periods, months and hours.

- Where spatiotemporal correlations in the left or middle columns hold between an ERA5 statistic and MLAI, this is suggestive that the vegetation cover *may* be responsible for the observed variations in the ERA5 statistic.

- Where spatiotemporal correlations hold between the right column of an ERA5 statistic and the left or middle columns for MLAI, this leaves open the question of what is causing the observed variations in the ERA5 statistic, but suggests that vegetation cover *may* be responsible for modulating these variations.
- Where spatiotemporal correlations hold between the right columns of an ERA5 statistic and MLAI, this is suggestive that the variations in vegetation cover *may* be responsible for the variations in the ERA5 statistic.

C.2 | Example usage

C.2.1 | plot_comp_mdp_clim_stats_given_var_or_dvar

Suppose we were interested in analysing the seasonal differences in the diurnal statistics of mean sea level pressure ("mslp") in a region of South America ("sa"), with default region extents manually defined in the `calc_funcs.py` script. Specifically, we are interested in differences between the wet season from January to June ([1,2,3,4,5,6]) and the dry season from July to December ([7,8,9,10,11,12]), over the period from "Jan-2001" to "Dec-2020". Then we would use the following code to obtain Figure C.1:

```
import plot_funcs_v1h as pf
pf.plot_comp_mdp_clim_stats_given_var_or_dvar(
  region="sa", period1_start="Jan-2001", period1_end="Dec-2020",
  period2_start="Jan-2001", period2_end="Dec-2020",
  period1_months=[1,2,3,4,5,6], period2_months=[7,8,9,10,11,12],
  glass_source_pref="modis", var_or_dvar="mslp",
  perc=False, mask_perc_quantile=pf.mask_perc_quantile_default,
  mask_period1=None, mask_period2=None, extents=None, cfv_data=None,
  output=True
)
```

Listing C.1: Example for plot_comp_mdp_clim_stats_given_var_or_dvar

C.2.2 | plot_comp_means_given_layer_and_type

Suppose we were interested in analysing differences in the means between two separate periods for the hourly change in variables ("dvars") at the surface ("sfc"), in a region of Central America ("ca"), with default region extents manually defined in the `calc_funcs.py` script. Specifically, we are interested in differences in means computed over daytime hours from 0800 to 1500 ([8,9,10,11,12,13,14,15]) and the wet season

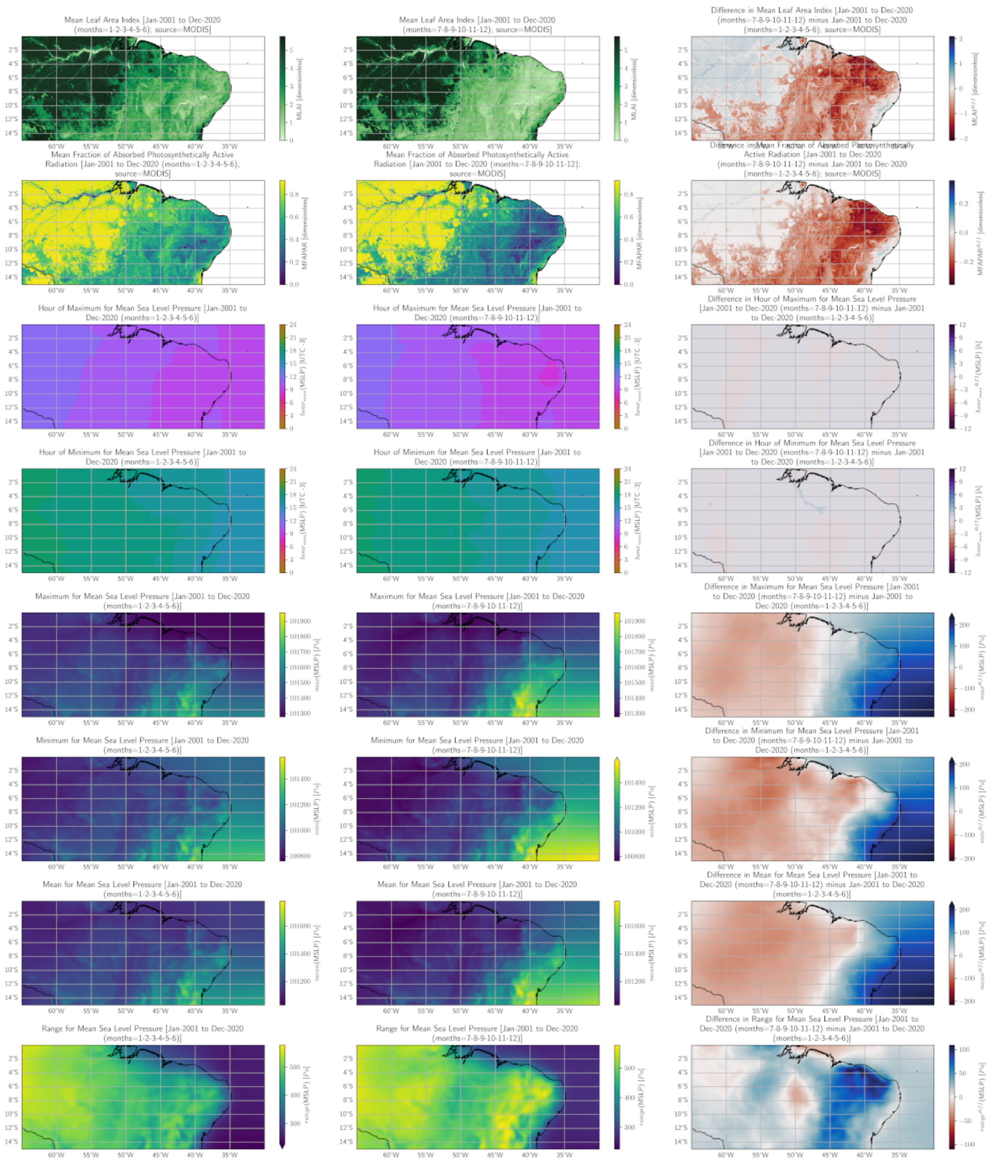

Figure C.1: Example for plot_comp_hourly_means_given_var_or_dvar from May to October ([5,6,7,8,9,10]), between the periods from "Jan-2003" to "Dec-2007" and "Jan-2016" to "Dec-2020". Then we would use the following code to obtain Figure C.2:

```
import plot_funcs_v1h as pf
pf.plot_comp_means_given_layer_and_type(
  region="ca", period1_start="Jan-2003", period1_end="Dec-2007",
  period2_start="Jan-2016", period2_end="Dec-2020",
  period1_months=[5,6,7,8,9,10], period2_months=[5,6,7,8,9,10],
  period1_hours=[8,9,10,11,12,13,14,15],
  period2_hours=[8,9,10,11,12,13,14,15],
  glass_source_pref="modis",
  var_or_dvar_layer="sfc", var_or_dvar_type="dvars",
  perc=False, mask_perc_quantile=pf.mask_perc_quantile_default,
  mask_period1=None, mask_period2=None, extents=None, cfv_data=None,
  output=True
)
```

Listing C.2: Example for plot_comp_means_given_layer_and_type

C.2.3 | plot_comp_hourly_means_given_var_or_dvar

Suppose we were interested in analysing the seasonal differences in the hourly means of vertical integral of energy conversion ("viec") in a region of Western Australia ("wa"), with default region extents manually defined in the `calc_funcs.py` script (and the State Boundary Fence of Western Australia is drawn in). Specifically, we are interested in differences between the wet season from July to August ("jja") and the dry season from December to February ("djf"), over the period from "Jan-2001" to "Dec-2020". Then we would use the following code to obtain Figure C.3:

```
import plot_funcs_v1h as pf
pf.plot_comp_hourly_means_given_var_or_dvar(
  region="wa", period1_start="Jan-2001", period1_end="Dec-2020",
  period2_start="Jan-2001", period2_end="Dec-2020",
  period1_months="jja", period2_months="djf", glass_source_pref="modis",
  var_or_dvar="viec", hours_to_plot="18-23",
  perc=False, mask_perc_quantile=pf.mask_perc_quantile_default,
  mask_period1=None, mask_period2=None, extents=None, cfv_data=None,
  output=True
)
```

Listing C.3: Example for plot_comp_hourly_means_given_var_or_dvar

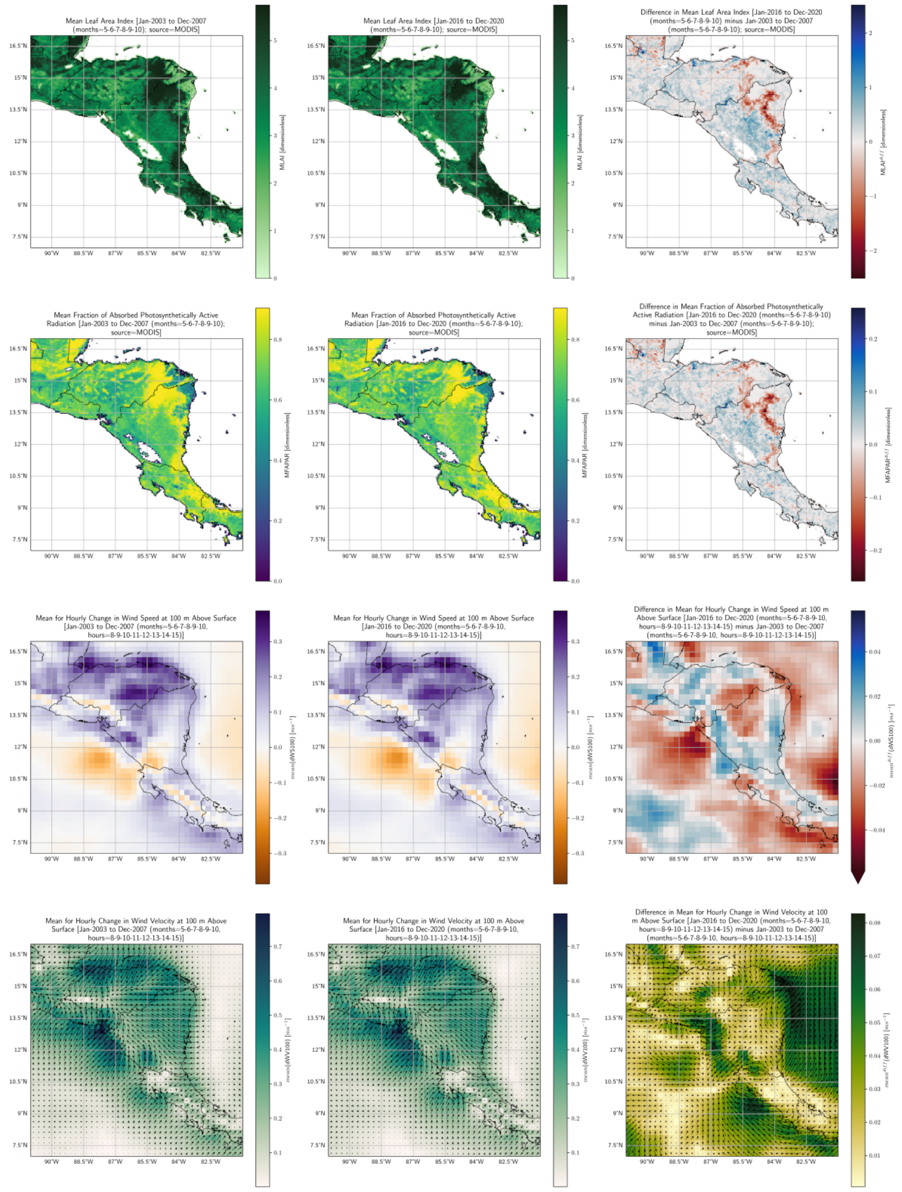

(a) First 4 rows of example plot

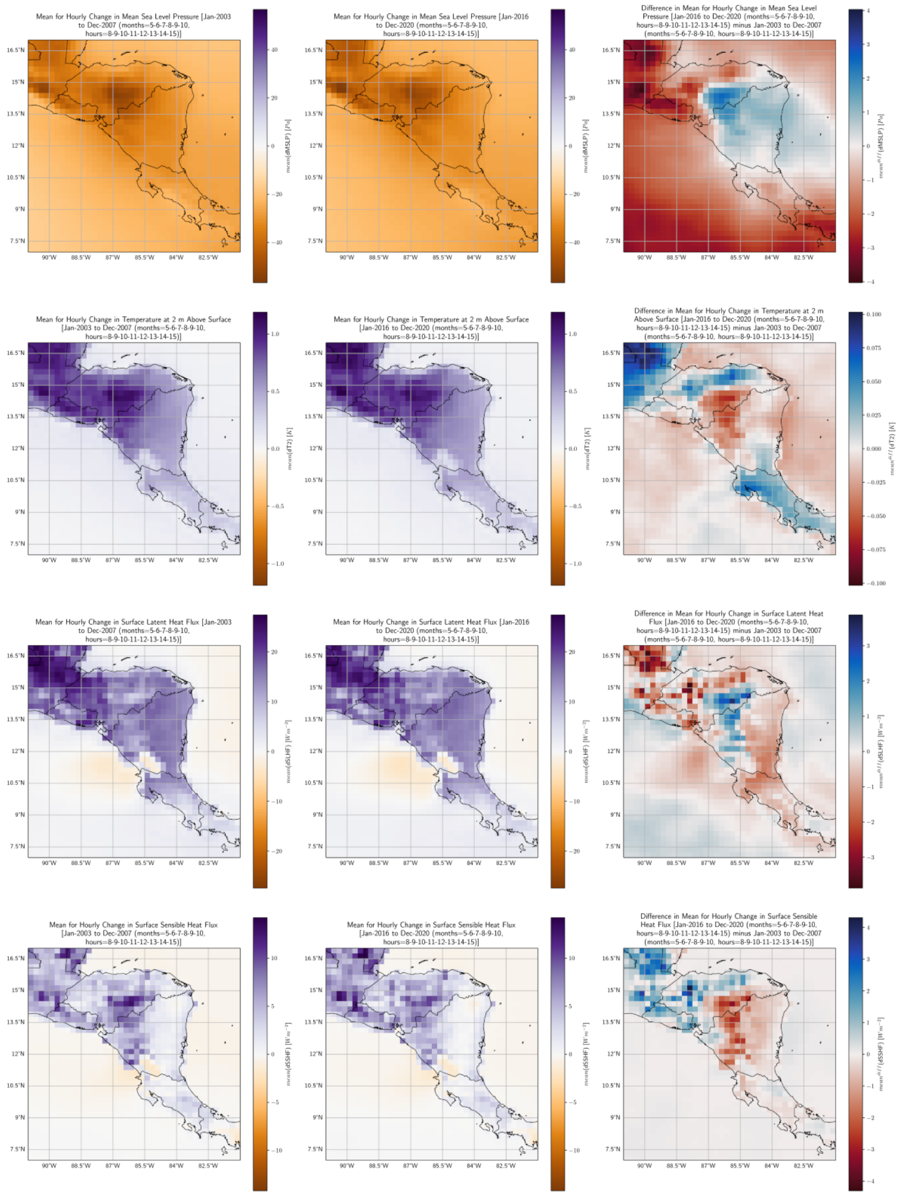

(b) Last 4 rows of example plot

Figure C.2: Example for plot_comp_means_given_layer_and_type

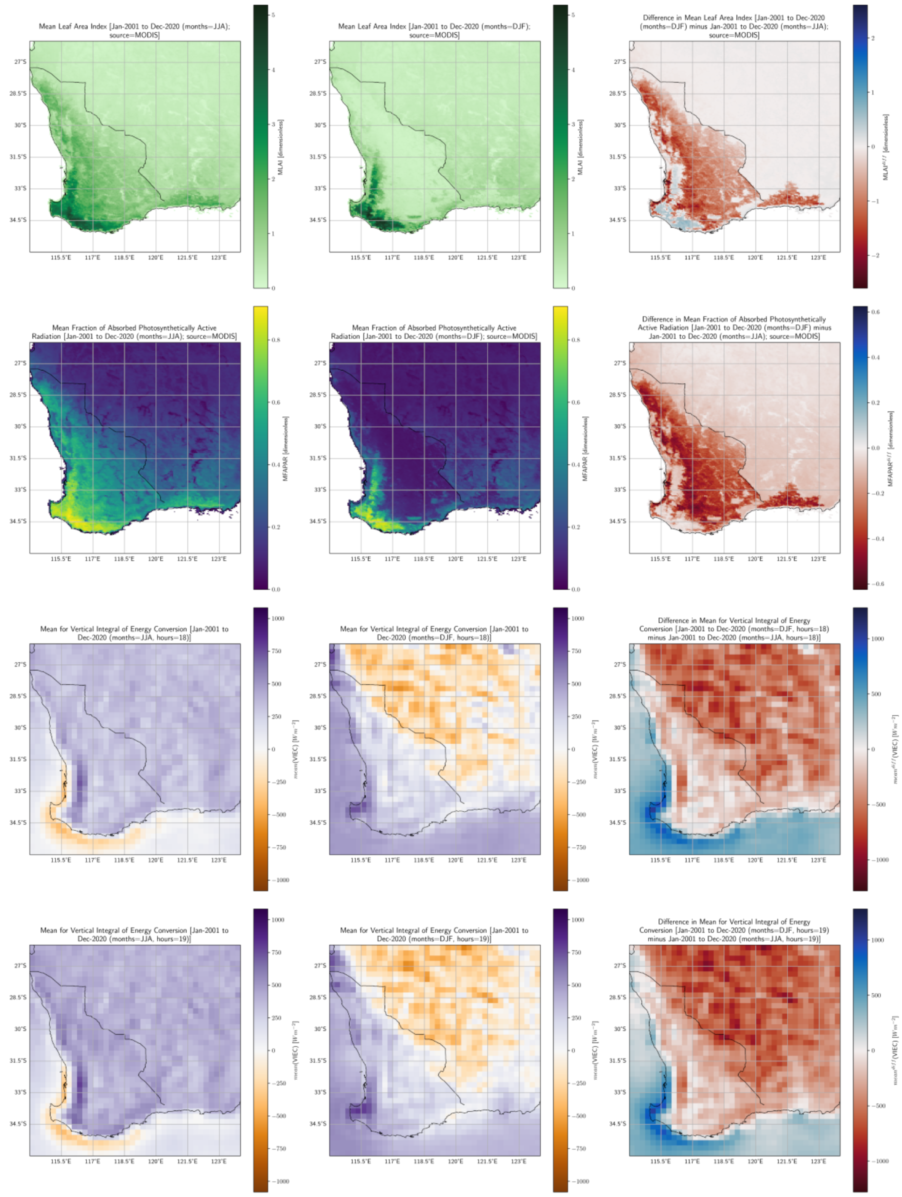

(a) First 4 rows of example plot

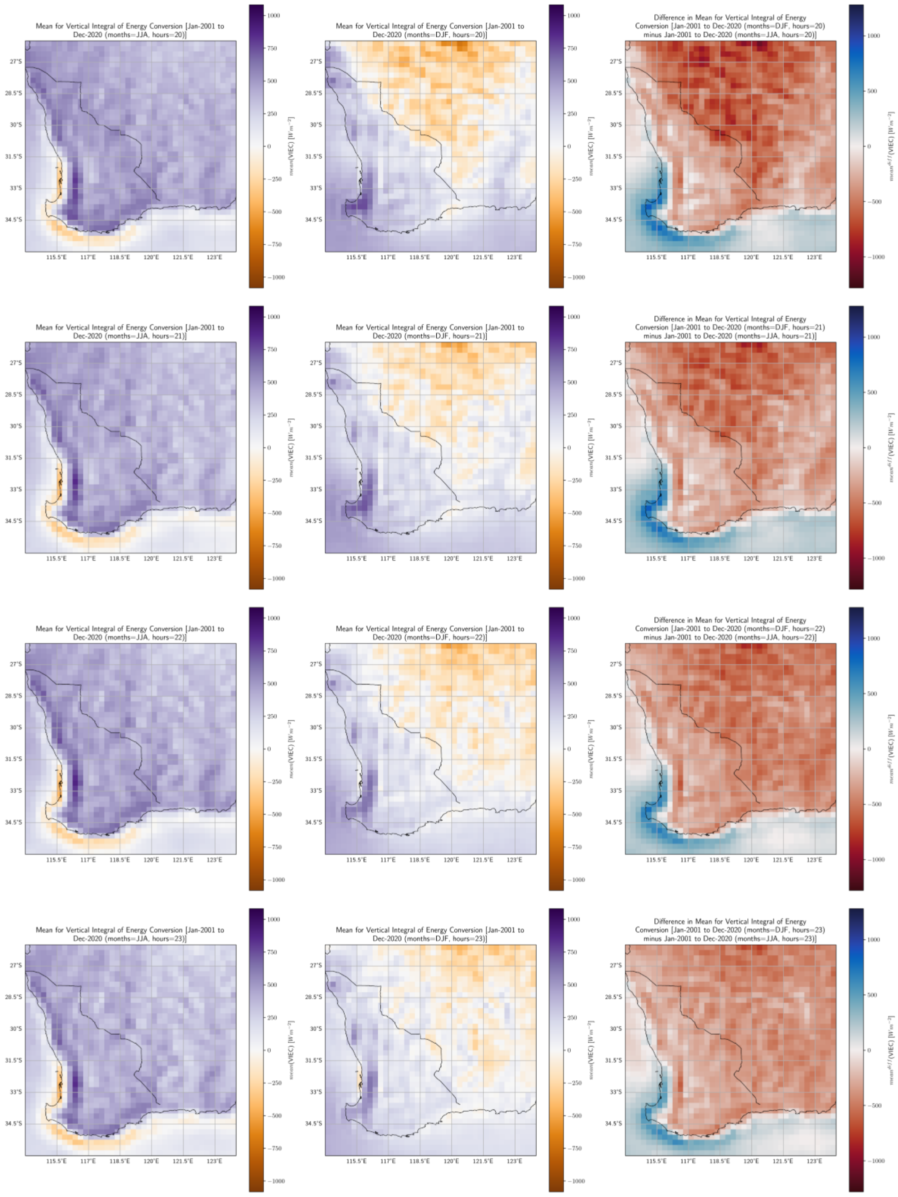

(b) Last 4 rows of example plot

Figure C.3: Example for plot_comp_hourly_means_given_var_or_dvar

C.3 | Analysing other regions and variables

Note: the steps in this section have not been tested as of the time of writing.

C.3.1 | For custom regions

- The default regions and extents in [W, E, S, N] format (for `cartopy` plotting library) used in the thesis project were:
  - "wa": [114, 124, -36, -26]
  - "ca": [-91, -81, 7, 17]
  - "sa": [-65, -30, -15, 0]
- To add a custom region:
  1. Edit the `area` variable in `data_download.ipynb` or `data_download.py` to include the name of the new region and its extents in [N, W, S, E] format (for ECMWF Climate Data Store (CDS) API)
  2. Edit the first argument in the `retrieve_era5_slv_month_hour` and `retrieve_era5_slv_hour` functions so that it reflects the name of the new region
  3. Run the edited `data_download.ipynb` or `data_download.py` to download the relevant ERA5 data from ECMWF
  4. Edit the `regions` variable in the `calc_funcs.py` script to include the new region's name, extents in [W, E, S, N] format, and local timezone relative to UTC

C.3.2 | For arbitrary ERA5 variables

- The ERA5 variables obtained from ECMWF for use in the thesis project by default were (using naming conventions from `https://confluence.ecmwf.int/display/CKB/ERA5%3A+data+documentation`):
  - `'100m_u_component_of_wind'`
  - `'100m_v_component_of_wind'`
  - `'10m_u_component_of_wind'`
  - `'10m_v_component_of_wind'`

  - '2m_temperature'
  - 'mean_sea_level_pressure'
  - 'surface_latent_heat_flux'
  - 'surface_sensible_heat_flux'
  - 'evaporation'
  - 'total_column_cloud_liquid_water'
  - 'total_column_water_vapour'
  - 'vertical_integral_of_divergence_of_moisture_flux'
  - 'vertical_integral_of_energy_conversion'
  - 'vertical_integral_of_kinetic_energy'
  - 'convective_inhibition'
  - 'forecast_albedo'
  - 'total_cloud_cover'

- To add an arbitrary ERA5 variable:
  1. Edit the `vars_era5` variable in `data_download.ipynb` or `data_download.py` to include the name of the new variable using the ERA5 variable names from `https://confluence.ecmwf.int/display/CKB/ERA5%3A+data+documentation`
  2. Place the variable within one of the existing "sfc", "atm" or "cld" categories
  3. (Alternatively) Create a new category with the variable and add additional code cells with the new category name as an argument into the `retrieve_era5_slv_month_hour` and `retrieve_era5_slv_hour functions`
  4. Run the edited `data_download.ipynb` or `data_download.py` to download the relevant ERA5 data from ECMWF CDS
  5. Edit the `vars_and_dvars_era5`, `vars_dep_and_rename` and `attrs_da` variables in the `calc_funcs.py` script to reflect this new variable
  6. Edit the try-except blocks in the `plot_means_given_layer_and_type`, `plot_diff_means_given_layer_and_type` and `plot_comp_means_given_layer_and_type` functions in the `plot_funcs.py` script so that a total of 6 ERA5 variables will be displayed at all times (this is an unfortunate design constraint from displaying 8 rows for the comparison plots with the first 2 rows occupied by MLAI and MFAPAR)

C.3.3 | For novel ERA5-derived variables

- The default ERA5-derived variables used in the thesis project were:
  - Instantaneous approximation (with negative sign reversed and units converted) for Surface Latent Heat Flux (SLHF)
  - Instantaneous approximation (with negative sign reversed and units converted) for Surface Sensible Heat Flux (SSHF)
  - Instantaneous approximation (with negative sign reversed and units converted) for Net Surface Evaporation (NSE)
  - Approximation for Net Atmospheric Condensation (NAC)
- To incorporate a novel ERA5-derived variable:
  1. Insert an if statement into the `calc_era5_mdp_clim_given_var_or_dvar` function in the `calc_funcs.py` script (this is the function which is furthest upstream and from which other computations apart from wind speed distribution derive from) using the same style and logic as that for NAC in the script
  2. Edit the `vars_and_dvars_era5`, `vars_dep_and_rename` and `attrs_da` variables in the `calc_funcs.py` script to reflect this new variable
  3. Edit the try-except blocks in the `plot_means_given_layer_and_type`, `plot_diff_means_given_layer_and_type` and `plot_comp_means_given_layer_and_type` functions in the `plot_funcs.py` script so that a total of 6 ERA5 variables will be displayed at all times (this is an unfortunate design constraint from displaying 8 rows for the comparison plots with the first 2 rows occupied by MLAI and MFAPAR)

C.4 | Steps to reproduce thesis results from scratch

Note: The original project scope included analysis for WA, CA and NB but this was cut short to only WA due to time constraints.

1. (If haven't already) Install miniconda for Python 3.9 or later using instructions from `https://docs.conda.io/en/latest/miniconda.html`
2. Download thesis repository by entering `git clone git@github.com:anthonylst6/thesis.git` into a bash shell

(Terminal for Linux or Mac, Git Bash recommended for Windows) or clicking Code -> Download ZIP on Github then unzip the folder

3. Open bash shell in home directory of repository then run `conda env create -f env_thesis.yml`

4. (If haven't already) Set up ECMWF CDS API using instructions from `https://confluence.ecmwf.int/display/CKB/How+to+download+ERA5#HowtodownloadERA5-4-DownloadERA5familydatathroughtheCDSAPI`

5. Download raw data by entering `conda activate thesis` into bash shell then running the `data_download.ipynb` notebook in the `scripts` directory (open the notebook by running `jupyter lab &` in the bash shell)

6. (Alternatively) Enter `conda run -n thesis python data_download.py` into bash shell from the `scripts` directory

7. (For proper rendering of figures) Make sure that a LaTeXdistribution is installed

8. Reproduce results by running the `results.ipynb` notebook in the `scripts` directory for different focus regions by commenting and uncommenting relevant code (again use `jupyter lab &` from bash shell to open notebooks)

9. (Alternatively) Enter `conda run -n thesis python results_wa.py`, `conda run -n thesis python results_ca.py` and `conda run -n thesis python results_sa.py` into bash shell from the `scripts` directory

10. (If personal computer is limited in RAM) Edit the `results_wa.pbs`, `results_ca.pbs` and `results_sa.pbs` job scripts in the `scripts` directory to be compatible with target HPC facility (the provided scripts were designed for the UNSW Katana computational cluster), then submit these as a batch job

C.5 | System and time requirements (for reproducing thesis results only)

- For Western Australia (WA) raw data and results, up to 25 GB of storage, several days for raw data download (due to queueing in ECMWF CDS), and for data processing up to 60 GB of RAM over 12 hours if using 8 CPUs

- For Central America (CA) raw data and results, up to 25 GB of storage, several days for raw data download (due to queueing in ECMWF CDS), and for data processing up to 60 GB of RAM over 12 hours if using 8 CPUs
- For Northern Brazil (NB) raw data and results, up to 80 GB of storage, several days for raw data download (due to queueing in ECMWF CDS), and for data processing up to 140 GB of RAM over 12 hours if using 8 CPUs
- The data processing can also be run with less RAM and fewer CPU cores but this will be slower and will require manual restarting of code everytime RAM limit is reached (the code was designed to pick up from where it left off). But in this case there should at least be 8 GB of RAM for WA and CA results, and at least 24 GB of RAM for NB results.

References

Influence of biogenic emissions from boreal forests on aerosol–cloud interactions. *Nature Geoscience*, 15(1):42–47, January 2022. ISSN 1752-0894, 1752-0908. doi: 10.1038/s41561-021-00876-0.

4C Offshore. Global Offshore Renewable Map. `https://web.archive.org/web/20221116035406/https://map.4coffshore.com/offshorewind/`, 2022. Last Accessed: November 16th, 2022.

Azorin-Molina, C., Vicente-Serrano, S. M., McVicar, T. R., Jerez, S., Sanchez-Lorenzo, A., López-Moreno, J.-I., Revuelto, J., Trigo, R. M., Lopez-Bustins, J. A., and Espírito-Santo, F. Homogenization and Assessment of Observed Near-Surface Wind Speed Trends over Spain and Portugal, 1961–2011. *Journal of Climate*, 27(10):3692–3712, May 2014. ISSN 0894-8755, 1520-0442. doi: 10.1175/JCLI-D-13-00652.1.

Azorin-Molina, C., Asin, J., McVicar, T. R., Minola, L., Lopez-Moreno, J. I., Vicente-Serrano, S. M., and Chen, D. Evaluating anemometer drift: A statistical approach to correct biases in wind speed measurement. *Atmospheric Research*, 203: 175–188, 2018a. doi: 10.1016/j.atmosres.2017.12.010.

Azorin-Molina, C., Rehman, S., Guijarro, J. A., McVicar, T. R., Minola, L., Chen, D., and Vicente-Serrano, S. M. Recent trends in wind speed across Saudi Arabia, 1978-2013: a break in the stilling. *International Journal of Climatology*, 38: e966–e984, April 2018b. ISSN 08998418. doi: 10.1002/joc.5423.

Benz, S. Insane Full Cloud Cover XC! `https://web.archive.org/web/20220415064844/https://www.youtube.com/watch?v=n_mfE7xXSVI`, March 2021a. Last Accessed: November 14th, 2022.

Benz, S. How to Read Big Clouds. `https://web.archive.org/web/20220415064021/https://www.youtube.com/watch?v=suiYnO5IqRs`, August 2021b. Last Accessed: November 14th, 2022.

Berthot, A., Pattiaratchi, C., Feng, M., Li, Y., and Meyers, G. Understanding the natural variability of currents along the Western Australian coastline. Technical report, SRFME Collaboration: CSIRO, WA Government, UWA, January 1997.

Bunyard, P., Hodnett, M., Poveda, G., Burgos Salcedo, J. D., and Peña, C. Experimental evidence of condensation-driven airflow. preprint, Hydrometeorology/Instruments and observation techniques, October 2015. URL `https://hess.copernicus.org/preprints/12/10921/2015/`.

Bunyard, P. P., Hodnett, M., Peña, C., and Burgos Salcedo, J. Condensation and partial pressure change as a major cause of airflow: Experimental evidence. *DYNA*, 84(202):92–101, July 2017. ISSN 2346-2183, 0012-7353. doi: 10.15446/dyna.v84n202.61253.

Bunyard, P. P., Hodnett, M., Peña, C., and Burgos-Salcedo, J. D. Further experimental evidence that condensation is a major cause of airflow. *DYNA*, 86(209):56–63, April 2019. ISSN 2346-2183, 0012-7353. doi: 10.15446/dyna.v86n209.73288.

C3S. Leaf area index and fraction absorbed of photosynthetically active radiation 10-daily gridded data from 1981 to present. doi: 10.24381/cds.7e59b01a, 2022. Last Accessed: November 16th, 2022.

Caballero, R., Pierrehumbert, R. T., and Mitchell, J. L. Axisymmetric, nearly inviscid circulations in non-condensing radiative-convective atmospheres. *Quarterly Journal of the Royal Meteorological Society*, 134(634):1269–1285, July 2008.

ISSN 00359009, 1477870X. doi: 10.1002/qj.271.

Chen, X., Li, C., and Xu, J. Failure investigation on a coastal wind farm damaged by super typhoon: A forensic engineering study. *Journal of Wind Engineering and Industrial Aerodynamics*, 147:132–142, December 2015. ISSN 01676105. doi: 10.1016/j.jweia.2015.10.007.

Chen, X., Li, C., and Tang, J. Structural integrity of wind turbines impacted by tropical cyclones: A case study from China. *Journal of Physics: Conference Series*, 753, September 2016. ISSN 1742-6588, 1742-6596. doi: 10.1088/1742-6596/753/4/042003.

Colin, M., Sherwood, S., Geoffroy, O., Bony, S., and Fuchs, D. Identifying the Sources of Convective Memory in Cloud-Resolving Simulations. *Journal of the Atmospheric Sciences*, 76(3):947–962, March 2019. ISSN 0022-4928, 1520-0469. doi: 10.1175/JAS-D-18-0036.1.

Cutrim, E., Martin, D. W., and Rabin, R. Enhancement of Cumulus Clouds over Deforested Lands in Amazonia. *Bulletin of the American Meteorological Society*, 76(10), 1995.

Dask Development Team. *Dask: Library for dynamic task scheduling*, 2016. URL `https://dask.org`.

Doddy Clarke, E., Griffin, S., McDermott, F., Monteiro Correia, J., and Sweeney, C. Which Reanalysis Dataset Should We Use for Renewable Energy Analysis in Ireland? *Atmosphere*, 12(5):624, May 2021. ISSN 2073-4433. doi: 10.3390/atmos12050624.

Droste, A. M., Steeneveld, G. J., and Holtslag, A. A. M. Introducing the urban wind island effect. *Environmental Research Letters*, 13(9), September 2018. ISSN 1748-9326. doi: 10.1088/1748-9326/aad8ef.

ECMWF. *IFS Documentation CY41R2*. IFS Documentation. ECMWF, 2016. URL `https://www.ecmwf.int/node/16646`.

ECMWF. ERA5: data documentation, known issues. `https://web.archive.org/web/20221116041420/https://confluence.ecmwf.int/display/CKB/ERA5%3A+data+documentation`, 2022. Last Accessed: November 16th, 2022.

Esau, I. and Lyons, T. Effect of sharp vegetation boundary on the convective atmospheric boundary layer. *Agricultural and Forest Meteorology*, 114(1-2):3–13, December 2002. ISSN 01681923. doi: 10.1016/S0168-1923(02)00154-5.

EUMETSTAT. A Year of Weather 2018. `https://web.archive.org/web/20221117113355/https://www.youtube.com/watch?v=wVRbeGc_6zM`, February 2018. Last Accessed: November 17th, 2022.

European Environment Agency. Europe's onshore and offshore wind energy potential: An assessment of environmental and economic constraints. Technical report, Office for Official Publications of the European Communities, Luxembourg, 2009. URL `https://data.europa.eu/doi/10.2800/11373`.

Fan, W., Liu, Y., Chappell, A., Dong, L., Xu, R., Ekström, M., Fu, T.-M., and Zeng, Z. Evaluation of Global Reanalysis Land Surface Wind Speed Trends to Support Wind Energy Development Using In Situ Observations. *Journal of Applied Meteorology and Climatology*, 60(1):33–50, January 2021. ISSN 1558-8424, 1558-8432. doi: 10.1175/JAMC-D-20-0037.1.

Fang, H., Baret, F., Plummer, S., and Schaepman-Strub, G. An Overview of Global Leaf Area Index (LAI): Methods, Products, Validation, and Applications. *Reviews of Geophysics*, 57(3):739–799, September 2019. ISSN 8755-1209, 1944-9208. doi: 10.1029/2018RG000608.

Fedosin, S. G. Four-dimensional equation of motion for viscous compressible and charged fluid with regard to the acceleration field, pressure field and dissipation field. *International Journal of Thermodynamics*, 18(1):13, March 2015. ISSN 2146-1511, 1301-9724. doi: 10.5541/ijot.5000034003.

Gadd, W. Part 2: Thermals and Clouds. `https://web.archive.org/web/20220415063620/https://www.skynomad.com/articles/thermal_clouds.htm`. Last Accessed: November 14th, 2022.

GE Energy. Riders On The Storm: GE Is Building A Wind Turbine That Can Weather Violent Typhoons, Hurricanes |

GE News. https://web.archive.org/web/20221116035328/https://www.ge.com/news/reports/riders-storm-ge-building-wind-turbine-can-weather-violent-typhoons-hurricanes, 2018. Last Accessed: November 16th, 2022.

Geiger, R. *The Climate Near The Ground*. Harvard University Press, Cambridge, Massachusetts, 1950.

Gero, A., Pitman, A., Narisma, G., Jacobson, C., and Pielke Sr., R. The impact of land cover change on storms in the Sydney Basin, Australia. *Global and Planetary Change*, 54(1-2):57–78, November 2006. ISSN 09218181. doi: 10.1016/j.gloplacha.2006.05.003.

Google Maps. Central America. https://www.google.com/maps/@13.9272885,-88.0715799,2172225m/data=!3m1!1e3, 2022a. Last Accessed: November 1st, 2022.

Google Maps. Northern Brazil. https://www.google.com/maps/@-8.9314753,-48.3178392,4421764m/data=!3m1!1e3, 2022b. Last Accessed: November 1st, 2022.

Google Maps. Western Australia. https://www.google.com/maps/@-30.9647554,119.2306323,1919065m/data=!3m1!1e3, 2022c. Last Accessed: November 1st, 2022.

Gordon, L., Dunlop, M., and Foran, B. Land cover change and water vapour flows: learning from Australia. *Philosophical Transactions of the Royal Society of London. Series B: Biological Sciences*, 358(1440):1973–1984, December 2003. ISSN 0962-8436, 1471-2970. doi: 10.1098/rstb.2003.1381.

Gorshkov, V. G., Gorshkov, V. V., and Makarieva, A. M. *Biotic Regulation of the Environment: Key Issue of Global Change*. Praxis Publishing Ltd, 2000.

Green, M. A. *Solar Cells: Operating Principles, Technology and System Applications*. The University of New South Wales, 1998.

Gualtieri, G. Reliability of ERA5 Reanalysis Data for Wind Resource Assessment: A Comparison against Tall Towers. *Energies*, 14(14):4169, July 2021. ISSN 1996-1073. doi: 10.3390/en14144169.

Guo, H., Xu, M., and Hu, Q. Changes in near-surface wind speed in China: 1969-2005. *International Journal of Climatology*, 31(3):349–358, March 2011. ISSN 08998418. doi: 10.1002/joc.2091.

He, C., Murray, F., and Lyons, T. Monoterpene and isoprene emissions from 15 Eucalyptus species in Australia. *Atmospheric Environment*, 34(4):645–655, January 2000. ISSN 13522310. doi: 10.1016/S1352-2310(99)00219-8.

He, Y., Monahan, A. H., and McFarlane, N. A. Diurnal variations of land surface wind speed probability distributions under clear-sky and low-cloud conditions. *Geophysical Research Letters*, 40(12):3308–3314, June 2013. ISSN 00948276. doi: 10.1002/grl.50575.

Held, I. M. and Hou, A. Y. Nonlinear Axially Symmetric Circulations in a Nearly Inviscid Atmosphere. *Journal of the Atmospheric Sciences*, 37(3):515–533, March 1980. ISSN 0022-4928, 1520-0469. doi: 10.1175/1520-0469(1980)037<0515:NASCIA>2.0.CO;2.

Hersbach, H., Bell, B., Berrisford, P., Biavati, G., Horanyi, A., Munoz Sabater, J., Nicola, J., Peubey, C., Radu, R., Rozum, I., Schepers, D., Simmons, A., Soci, C., Dee, D., and Thepaut, J.-N. ERA5 monthly averaged data on single levels from 1959 to present. doi: 10.24381/cds.f17050d7, 2019. Copernicus Climate Change Service (C3S) Climate Data Store (CDS). Last Accessed: September 26th, 2022.

Hong, X., Leach, M. J., and Raman, S. Role of vegetation in generation of mesoscale circulation. *Atmospheric Environment*, 29(16):2163–2176, August 1995. ISSN 13522310. doi: 10.1016/1352-2310(94)00241-C.

Hoyer, S. and Hamman, J. xarray: N-D labeled arrays and datasets in Python. *Journal of Open Research Software*, 5(1), 2017. doi: 10.5334/jors.148.

Hunter, J. D. Matplotlib: A 2d graphics environment. *Computing in Science & Engineering*, 9(3):90–95, 2007. doi: 10.1109/MCSE.2007.55.

Inness, A., Ades, M., Agustí-Panareda, A., Barré, J., Benedictow, A., Blechschmidt, A., Dominguez, J., Engelen, R., Eskes, H., Flemming, J., Huijnen, V., Jones, L., Kipling, Z., Massart, S., Parrington, M., Peuch, V.-H., M, R., Remy, S., Schulz, M., and Suttie, M. CAMS global reanalysis (EAC4) monthly averaged fields. `https://ads.atmosphere.copernicus.eu/cdsapp#!/dataset/cams-global-reanalysis-eac4-monthly?tab=overview`, 2019. Copernicus Atmosphere Monitoring Service (CAMS) Atmosphere Data Store (ADS). Last Accessed: November 18th, 2022.

IPCC. Climate change 2007: the physical science basis: contribution of Working Group II to the Fourth Assessment Report of the Intergovernmental Panel on Climate Change. Technical report, Cambridge University Press, Cambridge ; New York, 2007.

Jaramillo, A., Mesa, O. J., and Raymond, D. J. Is Condensation-Induced Atmospheric Dynamics a New Theory of the Origin of the Winds? *Journal of the Atmospheric Sciences*, 75(10):3305–3312, October 2018. ISSN 0022-4928, 1520-0469. doi: 10.1175/JAS-D-17-0293.1.

Jaramillo, A., Mesa, O. J., and Raymond, D. J. Reply to "Comments on 'Is Condensation-Induced Atmospheric Dynamics a New Theory of the Origin of the Winds?'". *Journal of the Atmospheric Sciences*, 2019(1):86–90, July 2019. ISSN 0022-4928, 1520-0469. doi: 10.1175/JAS-D-19-0025.1.

Jaswal, A. K. and Koppar, A. L. Climatology and trends in near-surface wind speed over India during 1961-2008. *MAUSAM*, 64(3), 2013. doi: 10.54302/mausam.v64i3.725.

Jiang, B. and Liang, S. Improved vegetation greenness increases summer atmospheric water vapor over Northern China. *Journal of Geophysical Research: Atmospheres*, 118(15):8129–8139, August 2013. ISSN 2169897X. doi: 10.1002/jgrd.50602.

Jiang, C., Liu, J., Zhang, H., Zhang, Z., and Wang, D. China's progress towards sustainable land degradation control: Insights from the northwest arid regions. *Ecological Engineering*, 127:75–87, February 2019. ISSN 09258574. doi: 10.1016/j.ecoleng.2018.11.014.

Johnson, S. L. and Wright, A. H. MINE VOID WATER RESOURCE ISSUES IN WESTERN AUSTRALIA. Technical Report HG 9, Water and Rivers Commission, Western Australia, 2003.

Junkermann, W., Hacker, J., Lyons, T., and Nair, U. Land use change suppresses precipitation. *Atmos. Chem. Phys.*, page 9, 2009.

Justus, C. G., Hargraves, W. R., Mikhail, A., and Graber, D. Methods for Estimating Wind Speed Distributions. *Journal of Applied Meteorology*, 17, 1977.

Khanna, J., Medvigy, D., Fueglistaler, S., and Walko, R. Regional dry-season climate changes due to three decades of Amazonian deforestation. *Nature Climate Change*, 7(3):200–204, March 2017. ISSN 1758-678X, 1758-6798. doi: 10.1038/nclimate3226.

Kitada, T., Okamura, K., and Tanaka, S. Effects of Topography and Urbanization on Local Winds and Thermal Environment in the Nohbi Plain, Coastal Region of Central Japan: A Numerical Analysis by Mesoscale Meteorological Model with a k-epsilon Turbulence Model. *Journal of Applied Meteorology*, 37:21, 1998. doi: 10.1175/1520-0450(1998)037<1026:EOTAUO>2.0.CO;2.

Knox, R., Bisht, G., Wang, J., and Bras, R. Precipitation Variability over the Forest-to-Nonforest Transition in Southwestern Amazonia. *Journal of Climate*, 24(9):2368–2377, May 2011. ISSN 0894-8755, 1520-0442. doi: 10.1175/2010JCLI3815.1.

Kröniger, K., De Roo, F., Brugger, P., Huq, S., Banerjee, T., Zinsser, J., Rotenberg, E., Yakir, D., Rohatyn, S., and Mauder, M. Effect of Secondary Circulations on the Surface–Atmosphere Exchange of Energy at an Isolated Semi-arid Forest. *Boundary-Layer Meteorology*, 169(2):209–232, November 2018. ISSN 0006-8314, 1573-1472. doi: 10.1007/s10546-018-0370-6.

Lapworth, A. Factors determining the decrease in surface wind speed following the evening transition. *Quarterly Journal of the Royal Meteorological Society*, 129(591):1945–1968, April 2003. ISSN 1477870X, 00359009. doi: 10.1256/qj.02.163.

Lapworth, A. The Morning Transition of the Nocturnal Boundary Layer. *Boundary-Layer Meteorology*, 119(3):501–526, June 2006. ISSN 0006-8314, 1573-1472. doi: 10.1007/s10546-005-9046-0.

Lee, B.-H., Ahn, D.-J., Kim, H.-G., and Ha, Y.-C. An estimation of the extreme wind speed using the Korea wind map. *Renewable Energy*, 42:4–10, June 2012. ISSN 09601481. doi: 10.1016/j.renene.2011.09.033.

Li, Y., Wang, Y., Chu, H., and Tang, J. The climate influence of anthropogenic land-use changes on near-surface wind energy potential in China. *Chinese Science Bulletin*, 53(18):2859–2866, September 2008. ISSN 2095-9273, 2095-9281. doi: 10.1007/s11434-008-0360-z.

Li, Y., Piao, S., Chen, A., Ciais, P., and Li, L. Z. X. Local and teleconnected temperature effects of afforestation and vegetation greening in China. *National Science Review*, 7(5):897–912, May 2020. ISSN 2095-5138, 2053-714X. doi: 10.1093/nsr/nwz132.

Liang, S., Cheng, J., Jia, K., Jiang, B., Liu, Q., Xiao, Z., Yao, Y., Yuan, W., Zhang, X., Zhao, X., and Zhou, J. The Global Land Surface Satellite (GLASS) Product Suite. *Bulletin of the American Meteorological Society*, 102(2):E323–E337, February 2021. ISSN 0003-0007, 1520-0477. doi: 10.1175/BAMS-D-18-0341.1.

Lyons, T. J. Clouds prefer native vegetation. *Meteorology and Atmospheric Physics*, 80(1-4):131–140, June 2002. ISSN 0177-7971, 1436-5065. doi: 10.1007/s007030200020.

Lyons, T. J., Xinmei, H., Schwerdtfeger, P., Hacker, J. M., Foster, I. J., and Smith, R. C. G. Land–Atmosphere Interaction in a Semiarid Region: The Bunny Fence Experiment. *Bulletin of the American Meteorological Society*, 74(7):1327–1334, July 1993. ISSN 0003-0007, 1520-0477.

Lyons, T. J., Smith, R. C. G., and Xinmei, H. THE IMPACT OF CLEARING FOR AGRICULTURE ON THE SURFACE ENERGY BUDGET. *International Journal of Climatology*, 16(5):551–558, May 1996. ISSN 0899-8418, 1097-0088. doi: 10.1002/(SICI)1097-0088(199605)16:5<551::AID-JOC25>3.0.CO;2-9.

Lyons, T. J., Fuqin, L., Hacker, J. M., Cheng, W.-L., and Xinmei, H. Regional turbulent statistics over contrasting natural surfaces. *Meteorology and Atmospheric Physics*, 78(3-4):183–194, December 2001. ISSN 0177-7971, 1436-5065. doi: 10.1007/s703-001-8172-0.

Mahmood, R., Leeper, R., and Quintanar, A. I. Sensitivity of planetary boundary layer atmosphere to historical and future changes of land use/land cover, vegetation fraction, and soil moisture in Western Kentucky, USA. *Global and Planetary Change*, 78(1-2):36–53, July 2011. ISSN 09218181. doi: 10.1016/j.gloplacha.2011.05.007.

Mahmood, R., Pielke Sr., R. A., Hubbard, K. G., Niyogi, D., Dirmeyer, P. A., McAlpine, C., Carleton, A. M., Hale, R., Gameda, S., Beltrán-Przekurat, A., Baker, B., McNider, R., Legates, D. R., Shepherd, M., Du, J., Blanken, P. D., Frauenfeld, O. W., Nair, U., and Fall, S. Land cover changes and their biogeophysical effects on climate. *International Journal of Climatology*, 34(4):929–953, March 2014. ISSN 08998418. doi: 10.1002/joc.3736.

Makarieva, A. M. and Gorshkov, V. G. Reply to A. G. C. A. Meesters et al.'s comment on "Biotic pump of atmospheric moisture as driver of the hydrological cycle on land". *Hydrology and Earth System Sciences*, 13(7):1307–1311, July 2009a. ISSN 1607-7938. doi: 10.5194/hess-13-1307-2009.

Makarieva, A. M., Gorshkov, V. G., Nobre, A. D., Nefiodov, A. V., Sheil, D., Nobre, P., and Li, B.-L. Comments on "Is Condensation-Induced Atmospheric Dynamics a New Theory of the Origin of the Winds?". *Journal of the Atmospheric Sciences*, 2019(1):81–85, July 2019. ISSN 0022-4928, 1520-0469. doi: 10.1175/JAS-D-18-0358.1.

Makarieva, A. M. and Gorshkov, V. G. Condensation-induced dynamic gas fluxes in a mixture of condensable and non-condensable gases. *Physics Letters A*, 373(32):2801–2804, August 2009b. ISSN 03759601. doi: 10.1016/j.physleta.2009.05.057.

Makarieva, A. M. and Gorshkov, V. G. The Biotic Pump: Condensation, atmospheric dynamics and climate. *International Journal of Water*, 5(4):365, 2010. ISSN 1465-6620, 1741-5322. doi: 10.1504/IJW.2010.038729.

Makarieva, A. M., Gorshkov, V. G., and Li, B.-L. Precipitation on land versus distance from the ocean: Evidence for a forest pump of atmospheric moisture. *Ecological Complexity*, 6(3):302–307, September 2009. ISSN 1476945X. doi:

10.1016/j.ecocom.2008.11.004.

Makarieva, A. M., Gorshkov, V. G., and Li, B.-L. Revisiting forest impact on atmospheric water vapor transport and precipitation. *Theoretical and Applied Climatology*, 111(1-2):79–96, January 2013a. ISSN 0177-798X, 1434-4483. doi: 10.1007/s00704-012-0643-9.

Makarieva, A. M., Gorshkov, V. G., Sheil, D., Nobre, A. D., and Li, B.-L. Where do winds come from? A new theory on how water vapor condensation influences atmospheric pressure and dynamics. *Atmospheric Chemistry and Physics*, 13 (2):1039–1056, January 2013b. ISSN 1680-7324. doi: 10.5194/acp-13-1039-2013.

Makarieva, A. M., Gorshkov, V. G., and Nefiodov, A. Condensational power of air circulation in the presence of a horizontal temperature gradient. *Physics Letters A*, 378(3):294–298, January 2014. ISSN 03759601. doi: 10.1016/j.physleta.2013.11.019.

Makarieva, A. M., Gorshkov, V. G., Nefiodov, A. V., Sheil, D., Nobre, A. D., Bunyard, P., Nobre, P., and Li, B. The equations of motion for moist atmospheric air. *Journal of Geophysical Research: Atmospheres*, 122(14):7300–7307, July 2017. ISSN 2169-897X, 2169-8996. doi: 10.1002/2017JD026773.

Martius, O., Wehrli, K., and Rohrer, M. Local and remote atmospheric responses to soil moisture anomalies in Australia. *Journal of Climate*, pages 1–48, August 2021. ISSN 0894-8755, 1520-0442. doi: 10.1175/JCLI-D-21-0130.1.

Marx, A., McFarlane, D., and Alzahrani, A. UAV data for multi-temporal Landsat analysis of historic reforestation: a case study in Costa Rica. *International Journal of Remote Sensing*, 38(8-10):2331–2348, May 2017. ISSN 0143-1161, 1366-5901. doi: 10.1080/01431161.2017.1280637.

Matthew, O. J. and Ohunakin, O. S. Simulating the effects of climate change and afforestation on wind power potential in Nigeria. *Sustainable Energy Technologies and Assessments*, 22:41–54, August 2017. ISSN 22131388. doi: 10.1016/j.seta.2017.05.009.

May, R. M., Arms, S. C., Marsh, P., Bruning, E., Leeman, J. R., Goebbert, K., Thielen, J. E., Bruick, Z. S., and Camron, M. D. Metpy: A Python package for meteorological data. `https://github.com/Unidata/MetPy`.

McVicar, T. R., Van Niel, T. G., Li, L. T., Roderick, M. L., Rayner, D. P., Ricciardulli, L., and Donohue, R. J. Wind speed climatology and trends for Australia, 1975–2006: Capturing the stilling phenomenon and comparison with near-surface reanalysis output. *Geophysical Research Letters*, 35(20):L20403, October 2008. ISSN 0094-8276. doi: 10.1029/2008GL035627.

Meesters, A., Dolman, A., and Bruijnzeel, L. Comment on "biotic pump of atmospheric moisture as driver of the hydrological cycle on land" by A. M. Makarieva and V. G. Gorshkov, Hydrol. Earth Syst. Sci., 11, 1013-1033, 2007. *Hydrology and Earth System Sciences*, 13(7):1299–1305, 2009. ISSN 1027-5606. doi: 10.5194/hess-13-1299-2009.

Met Office. *Cartopy: a cartographic python library with a matplotlib interface*. Exeter, Devon, 2010 - 2015. URL `http://scitools.org.uk/cartopy`.

Minola, L., Azorin-Molina, C., and Chen, D. Homogenization and Assessment of Observed Near-Surface Wind Speed Trends across Sweden, 1956–2013. *Journal of Climate*, 29(20):7397–7415, October 2016. ISSN 0894-8755, 1520-0442. doi: 10.1175/JCLI-D-15-0636.1.

Minola, L., Reese, H., Lai, H., Azorin-Molina, C., Guijarro, J. A., Son, S., and Chen, D. Wind stilling-reversal across Sweden: The impact of land-use and large-scale atmospheric circulation changes. *International Journal of Climatology*, 42(2):1049–1071, February 2022. ISSN 0899-8418, 1097-0088. doi: 10.1002/joc.7289.

Nair, U. S., Wu, Y., Kala, J., Lyons, T. J., Pielke Sr., R. A., and Hacker, J. M. The role of land use change on the development and evolution of the west coast trough, convective clouds, and precipitation in southwest Australia. *Journal of Geophysical Research*, 116(D7), April 2011. ISSN 0148-0227. doi: 10.1029/2010JD014950.

Narisma, G. T. and Pitman, A. J. The Impact of 200 Years of Land Cover Change on the Australian Near-Surface Climate. *Journal of Hydrometeorology*, 4(2):424–436, April 2003. ISSN 1525-755X, 1525-7541. doi: 10.1175/1525-7541(2003)4<424:TIOYOL>2.0.CO;2.

NOAA-PSL and NOAA-CPC. Climate Indices: Monthly Atmospheric and Ocean Time Series. https://web.archive.org/web/20221116040507/https://psl.noaa.gov/data/climateindices/list/, 2022. Last Accessed: November 16th, 2022.

Norris, J. R., Ralph, F. M., Demirdjian, R., Cannon, F., Blomquist, B., Fairall, C. W., Spackman, J. R., Tanelli, S., and Waliser, D. E. The Observed Water Vapor Budget in an Atmospheric River over the Northeast Pacific. *Journal of Hydrometeorology*, 21(11):2655–2673, November 2020. ISSN 1525-755X, 1525-7541. doi: 10.1175/JHM-D-20-0048.1.

Pagen, D. *Understanding the Sky*. First edition, 1992.

Pagen, D. *The Art of Paragliding*. Sport Aviation Publications, Spring Mills, PA., 2001. ISBN 978-0-936310-14-5. OCLC: 225368330.

Palutikof, J. P., Brabson, B. B., Lister, D. H., and Adcock, S. T. A review of methods to calculate extreme wind speeds. *Meteorological Applications*, 6(2):119–132, June 1999. ISSN 13504827. doi: 10.1017/S1350482799001103.

Petäjä, T., Moisseev, D., Sinclair, V., O'Connor, E., Manninen, A., Levula, J., Väänänen, R., Heikkinen, L., Äijälä, M., Aalto, J., and Thornton, J. Biogenic Aerosols—Effects on Clouds and Climate (BAECC) Final Campaign Summary. Technical Report DOE/SC-ARM–15-051, 1242990, March 2016. URL http://www.osti.gov/servlets/purl/1242990/.

Peña, A., Gryning, S.-E., and Hahmann, A. Observations of the atmospheric boundary layer height under marine upstream flow conditions at a coastal site. *Journal of Geophysical Research: Atmospheres*, 118(4):1924–1940, February 2013. ISSN 2169897X. doi: 10.1002/jgrd.50175.

Pitman, A. J., Narisma, G. T., Pielke Sr., R., and Holbrook, N. J. Impact of land cover change on the climate of southwest Western Australia. *Journal of Geophysical Research*, 109(D18):D18109, 2004. ISSN 0148-0227. doi: 10.1029/2003JD004347.

Rajeswari, J. R., Srinivas, C. V., and Venkatraman, B. Impact of urbanization on boundary-layer parameters and mesoscale circulations over tropical coastal city, Chennai. *Meteorology and Atmospheric Physics*, 134(1):3, February 2022. ISSN 0177-7971, 1436-5065. doi: 10.1007/s00703-021-00843-9.

Ramon, J., Llorenç, L., Verónica, T., Soret, A., and Doblas-Reyes, F. J. What global reanalysis best represents near-surface winds? *Quarterly Journal of the Royal Meteorological Society*, 145:3236–3251, 2019. doi: 10.1002/qj.3616.

Ray, D. K., Nair, U. S., Welch, R. M., Han, Q., Zeng, J., Su, W., Kikuchi, T., and Lyons, T. J. Effects of land use in Southwest Australia: 1. Observations of cumulus cloudiness and energy fluxes. *Journal of Geophysical Research*, 108(D14):4414, 2003. ISSN 0148-0227. doi: 10.1029/2002JD002654.

Rejmanek, H. 10 Years of What I Know About the Weather. https://web.archive.org/web/20210225053908/https://xcmag.com/magazine-articles/honza-rejmanek-10-years-of-what-i-know-about-the-weather/, 2018. Last Accessed: November 14th, 2022.

Rosenkranz, M., Pugh, T. A. M., Schnitzler, J.-P., and Arneth, A. Effect of land-use change and management on biogenic volatile organic compound emissions - selecting climate-smart cultivars: Climate-smart BVOC emissions. *Plant, Cell & Environment*, 38(9):1896–1912, September 2015. ISSN 01407791. doi: 10.1111/pce.12453.

Schneider, T. The General Circulation of the Atmosphere. *Annual Review of Earth and Planetary Science*, 34:655–688, 2006. doi: 10.1146/annurev.earth.34.031405.125144.

Shen, C., Zha, J., Wu, J., and Zhao, D. Centennial-scale variability of terrestrial near-surface wind speed over China from reanalysis. *Journal of Climate*, pages 1–52, April 2021. ISSN 0894-8755, 1520-0442. doi: 10.1175/JCLI-D-20-0436.1.

Taylor, C. M., Klein, C., Parker, D. J., Gerard, F., Semeena, V. S., Barton, E. J., and Harris, B. L. "Late-stage" deforestation enhances storm trends in coastal West Africa. *Proceedings of the National Academy of Sciences*, 119(2):e2109285119, January 2022. ISSN 0027-8424, 1091-6490. doi: 10.1073/pnas.2109285119.

The Wind Power. Brazil - Map. https://web.archive.org/web/20221116035232/https://www.thewindpower.net/country_maps_en_26_brazil.php, 2022a. Last Accessed: November 16th, 2022.

The Wind Power. Costa Rica - Map. https://web.archive.org/web/20221116035129/https://www.thewindpower.net/country_maps_en_29_costa-rica.php, 2022b. Last Accessed: November 16th, 2022.

The Wind Power. GE Energy 2.5-100. https://web.archive.org/web/20221116035517/https://www.thewindpower.net/turbine_en_382_ge-energy_2.5-100.php, 2022c. Last Accessed: November 16th, 2022.

The Wind Power. Goldwind GW100/2500. https://web.archive.org/web/20221116035742/https://www.thewindpower.net/turbine_en_669_goldwind_gw100-2500.php, 2022d. Last Accessed: November 16th, 2022.

The Wind Power. Honduras - Map. https://web.archive.org/web/20221116034814/https://www.thewindpower.net/country_maps_en_83_honduras.php, 2022e. Last Accessed: November 16th, 2022.

The Wind Power. Nicaragua - Map. https://web.archive.org/web/20221116035034/https://www.thewindpower.net/country_maps_en_84_nicaragua.php, 2022f. Last Accessed: November 16th, 2022.

The Wind Power. Vestas V100/2600. https://web.archive.org/web/20221116040006/https://www.thewindpower.net/turbine_en_778_vestas_v100-2600.php, 2022g. Last Accessed: November 16th, 2022.

The Wind Power. Australia - Map. https://web.archive.org/web/20221116034619/https://www.thewindpower.net/country_maps_en_16_australia.php, 2022h. Last Accessed: November 16th, 2022.

Tompkins, A. M. Organization of Tropical Convection in Low Vertical Wind Shears: The Role of Water Vapor. *Journal of the Atmospheric Sciences*, 58(6):529–545, March 2001a. ISSN 0022-4928, 1520-0469.

Tompkins, A. M. On the Relationship between Tropical Convection and Sea Surface Temperature. *Journal of Climate*, 14 (5):633–637, March 2001b. ISSN 0894-8755, 1520-0442. doi: 10.1175/1520-0442(2001)014<0633:OTRBTC>2.0.CO;2.

Torralba, V., Doblas-Reyes, F. J., and Gonzalez-Reviriego, N. Uncertainty in recent near-surface wind speed trends: a global reanalysis intercomparison. *Environmental Research Letters*, 12(11):114019, November 2017. ISSN 1748-9326. doi: 10.1088/1748-9326/aa8a58.

Vermote, E. NOAA CDR Program. (2019): NOAA Climate Data Record (CDR) of AVHRR Leaf Area Index (LAI) and Fraction of Absorbed Photosynthetically Active Radiation (FAPAR), Version 5. doi: 10.7289/V5TT4P69, 2022a. Last Accessed: November 17th, 2022.

Vermote, E. NOAA CDR Program. (2019): NOAA Climate Data Record (CDR) of AVHRR Normalized Difference Vegetation Index (NDVI), Version 5. doi: 10.7289/V5ZG6QH9, 2022b. Last Accessed: November 17th, 2022.

WA Department of Primary Industries and Regional Development. Wheat yield potential and land management constraints in the south-west of Western Australia. https://web.archive.org/web/20221116041215/https://www.agric.wa.gov.au/managing-soils/wheat-yield-potential-and-land-management-constraints-south-west-western-australia, 2021a. Last Accessed: November 16th, 2022.

WA Department of Primary Industries and Regional Development. Climate drivers of the South West Land Division. https://web.archive.org/web/20221116040647/https://www.agric.wa.gov.au/climate-weather/climate-drivers-south-west-land-division, 2021b. Last Accessed: November 8th, 2022.

WA Department of Water and Environmental Regulation. Effects of mining - bauxite hydrology. https://web.archive.org/web/20221116041724/https://www.water.wa.gov.au/water-topics/water-quality/managing-water-quality/effects-of-mining-bauxite-hydrology. Last Accessed: November 16th, 2022.

Wang, J., Chagnon, F. J. F., Williams, E. R., Betts, A. K., Renno, N. O., Machado, L. A. T., Bisht, G., Knox, R., and Bras, R. L. Impact of deforestation in the Amazon basin on cloud climatology. *Proceedings of the National Academy of Sciences*, 106 (10):3670–3674, March 2009. ISSN 0027-8424, 1091-6490. doi: 10.1073/pnas.0810156106.

Wang, J., Feng, J., Yan, Z., and Zha, J. Urbanization Impact on Regional Wind Stilling: A Modeling Study in the Beijing-Tianjin-Hebei Region of China. *Journal of Geophysical Research: Atmospheres*, 125(20), October 2020. ISSN 2169-897X, 2169-8996. doi: 10.1029/2020JD033132.

Wurfel, P. and Wurfel, U. *Physics of Solar Cells: From Basic Principles to Advanced Concepts*. Wiley-VCH, third edition, 2016.

Xinmei, H., Lyons, T. J., and Smith, R. C. G. Meteorological impact of replacing native perennial vegetation with annual agricultural species. *Hydrological Processes*, 9(5-6):645–654, June 1995. ISSN 08856087, 10991085. doi: 10.1002/hyp.3360090512.

Xu, R., Li, Y., Teuling, A. J., Zhao, L., Spracklen, D. V., Garcia-Carreras, L., Meier, R., Chen, L., Zheng, Y., Lin, H., and Fu, B. Contrasting impacts of forests on cloud cover based on satellite observations. *Nature Communications*, 13(1):670, 2022. ISSN 2041-1723. doi: 10.1038/s41467-022-28161-7.

Yan, H., Huang, J., He, Y., Liu, Y., Wang, T., and Li, J. Atmospheric Water Vapor Budget and Its Long-Term Trend Over the Tibetan Plateau. *Journal of Geophysical Research: Atmospheres*, 125(23), December 2020. ISSN 2169-897X, 2169-8996. doi: 10.1029/2020JD033297.

Yan, Y. and Zheng-Hui, X. A Simulation Study on Climatic Effects of Land Cover Change in China. *Advances in Climate Change Research*, 4(2):117–126, June 2013. ISSN 16749278. doi: 10.3724/SP.J.1248.2013.117.

Yu, R., Li, J., and Chen, H. Diurnal variation of surface wind over central eastern China. *Climate Dynamics*, 33(7-8): 1089–1097, December 2009. ISSN 0930-7575, 1432-0894. doi: 10.1007/s00382-008-0478-3.

Zeng, Z., Ziegler, A. D., Searchinger, T., Yang, L., Chen, A., Ju, K., Piao, S., Li, L. Z. X., Ciais, P., Chen, D., Liu, J., Azorin-Molina, C., Chappell, A., Medvigy, D., and Wood, E. F. A reversal in global terrestrial stilling and its implications for wind energy production. *Nature Climate Change*, 9(12):979–985, December 2019. ISSN 1758-678X, 1758-6798. doi: 10.1038/s41558-019-0622-6.

Zha, J., Wu, J., and Zhao, D. Changes of probabilities in different wind grades induced by land use and cover change in Eastern China Plain during 1980–2011. *Atmospheric Science Letters*, 17(4):264–269, April 2016. ISSN 1530-261X, 1530-261X. doi: 10.1002/asl.653.

Zha, J., Wu, J., and Zhao, D. Effects of land use and cover change on the near-surface wind speed over China in the last 30 years. *Progress in Physical Geography: Earth and Environment*, 41(1):46–67, February 2017a. ISSN 0309-1333, 1477-0296. doi: 10.1177/0309133316663097.

Zha, J., Wu, J., Zhao, D., and Yang, Q. Changes of the probabilities in different ranges of near-surface wind speed in China during the period for 1970–2011. *Journal of Wind Engineering and Industrial Aerodynamics*, 169:156–167, October 2017b. ISSN 01676105. doi: 10.1016/j.jweia.2017.07.019.

Zha, J., Zhao, D., Wu, J., and Shen, C. Terrestrial Near-Surface Wind Speed Variations in China: Research Progress and Prospects. *Journal of Meteorological Research*, 35(3):537–556, June 2021. ISSN 2095-6037, 2198-0934. doi: 10.1007/s13351-021-0143-x.

Zhang, G., Azorin-Molina, C., Chen, D., McVicar, T. R., Guijarro, J. A., Kong, F., Minola, L., Deng, K., and Shi, P. Uneven Warming Likely Contributed to Declining Near-Surface Wind Speeds in Northern China Between 1961 and 2016. *Journal of Geophysical Research: Atmospheres*, 126(11), June 2021. ISSN 2169-897X, 2169-8996. doi: 10.1029/2020JD033637.

Zhang, G., Azorin-Molina, C., Wang, X., Chen, D., McVicar, T. R., Guijarro, J. A., Chappell, A., Deng, K., Minola, L., Kong, F., Wang, S., and Shi, P. Rapid urbanization induced daily maximum wind speed decline in metropolitan areas: A case study in the Yangtze River Delta (China). *Urban Climate*, 43:101147, May 2022. ISSN 22120955. doi: 10.1016/j.uclim.2022.101147.

Zhang, R., Zhang, S., Luo, J., Han, Y., and Zhang, J. Analysis of near-surface wind speed change in China during 1958–2015. *Theoretical and Applied Climatology*, 137(3-4):2785–2801, August 2019. ISSN 0177-798X, 1434-4483. doi: 10.1007/s00704-019-02769-0.

Zhang, Y., Peña-Arancibia, J. L., McVicar, T. R., Chiew, F. H. S., Vaze, J., Liu, C., Lu, X., Zheng, H., Wang, Y., Liu, Y. Y., Miralles, D. G., and Pan, M. Multi-decadal trends in global terrestrial evapotranspiration and its components.

Scientific Reports, 6(1):19124, May 2016. ISSN 2045-2322. doi: 10.1038/srep19124.

Zhang, Y., Sun, K., Gao, Z., Pan, Z., Shook, M. A., and Li, D. Diurnal Climatology of Planetary Boundary Layer Height Over the Contiguous United States Derived From AMDAR and Reanalysis Data. *Journal of Geophysical Research: Atmospheres*, 125(20), October 2020. ISSN 2169-897X, 2169-8996. doi: 10.1029/2020JD032803.

Zhao, M., Pitman, A. J., and Chase, T. The impact of land cover change on the atmospheric circulation. *Climate Dynamics*, 17(5-6):467–477, March 2001. ISSN 0930-7575. doi: 10.1007/PL00013740.

Zhao, M. and Pitman, A. J. The regional scale impact of land cover change simulated with a climate model. *International Journal of Climatology*, 22(3):271–290, February 2002. ISSN 0899-8418, 1097-0088. doi: 10.1002/joc.727.

Zhi, H., Wang, P., Dan, L., Yu, Y., Xu, Y., and Zheng, W. Climate-vegetation interannual variability in a coupled atmosphere-ocean-land model. *Advances in Atmospheric Sciences*, 26(3):599–612, May 2009. ISSN 0256-1530, 1861-9533. doi: 10.1007/s00376-009-0599-6.

Zhuojia, Y. and Xinyuan, J. Mesoscale vegetation-breeze circulations and their impact on boundary layer structures at night. *Advances in Atmospheric Sciences*, 12(1):29–46, March 1995. ISSN 0256-1530, 1861-9533. doi: 10.1007/BF02661285.